# CONSIDERATIONS FOR DISCRETE ELEMENT MODELING OF ROCK CUTTING

by

Jorge Alejandro Mendoza Rizo

B.S. in Civil Engineering, Universidad Nacional de Colombia, 2008

M.S. in Civil Engineering, University of Pittsburgh, 2010

Submitted to the Graduate Faculty of

Swanson School of Engineering in partial fulfillment

of the requirements for the degree of

Doctor of Philosophy in Civil Engineering

University of Pittsburgh

2013

UNIVERSITY OF PITTSBURGH

SWANSON SCHOOL OF ENGINEERING

This dissertation was presented

by

Jorge Alejandro Mendoza Rizo

It was defended on

July 19th, 2013

and approved by

Jeen-Shang Lin, Sc. D., Associate Professor, Department of Civil and Environmental Engineering

Luis E. Vallejo, Ph. D., Professor, Department of Civil and Environmental Engineering

John C. Brigham, Ph. D., Assistant Professor, Department of Civil and Environmental Engineering

Albert C. To, Ph. D., Assistant Professor, Department of Mechanical Engineering and Materials Science

Isaac K. Gamwo, Ph. D., P.E., Research Chemical Engineer, National Energy Technology Laboratory

Dissertation Director: Jeen-Shang Lin, Sc. D., Associate Professor

**CONSIDERATIONS FOR DISCRETE ELEMENT MODELING OF ROCK CUTTING**

Jorge Alejandro Mendoza Rizo, Ph. D.

University of Pittsburgh, 2013

This study attempts to build a framework within the Discrete Element Method (DEM) to produce a reliable predictive tool in rock cutting applications, such that the cutting forces and fragmentation process are reasonably estimated. The study is limited to shallow depth cutting, often the mode of cutting involved in drilling operations.

Rock cutting requires the consideration of tool-rock interaction and the damage or fracture of rocks. With respect to modeling, rock cutting becomes a sequence of difficult problems: A contact problem first arises as a cutter advances and interacts with a target rock. This is followed by the problem of determining the location and nature of the rock failure. In the event of rock failure, a modeler must then consider modeling the initiation of the fragmentation process. The adopted approach utilizes the intrinsic capability of DEM to adequately consider contacts and model fractures. The commercial DEM codes PFC2D and PFC3D from Itasca were used.

This modeling effort focuses on the rock cutting that occurs during rock scratching tests. Two primary reasons provide the impetus of this investigation: first, a rock scratching test possesses all essential characteristics of a general rock cutting problem; second, available test data, particularly data obtained by Richard [1], provide a basis for validation. Modeling the scratch test also served another purpose for understanding the mechanics of drilling into rock because the cutting action is very similar to that of a single polycrystalline diamond compact (PDC) bit.

The validation of the present modeling effort utilizes an observation made by Richard and Dagrain [2] during shallow cuts that the specific energy obtained in a scratch test is approximately equal to the uniaxial strength of the rock. Rocks were represented as bonded particles [3]. This study first explores the sensitivity of the essential parameters that affect rock behavior and parameter selection necessary to realistically represent a rock. Extensive two-dimensional analyses were first completed and followed by three-dimensional analyses, all of which were conducted under an ambient pressure environment.

This study also addressed an important question regarding rock porosity. The current practice often implicitly considers porosity. Essentially, a porosity that is computationally simple and advantageous but ultimately unrealistic is used and other DEM parameters are consequently adjusted until the desired modulus and strength are produced. This sample is then considered mechanically equivalent. The ability to substitute rock materials of low porosities with higher values is extremely beneficial for computational efficiency. Samples with small porosity values were generated by solving the Apollonius' problem to fill voids with particles, and therefore, the influence of initial sample microstructure could be studied.

The Unconfined Compressive Strength (UCS) for most rocks is generally about ten times greater than that of the tensile strength [4]. This ratio, considered to be realistic rock behavior, has been historically difficult to obtain in similar models. In order to achieve this strength ratio, microdefects were also introduced into the sample. This study was able to implicitly model porosity by introducing optimal microdefects percentages in order to create equivalent rock samples with varying porosity values. Moreover, a connection between two-dimensional and three-dimensional samples was also established by finding an appropriate porosity to match the two models.

This study presented a validated and simplified framework for modeling rock cutting, and should be useful for general applications for a wide variety of fields. Preliminary work on cutting under high pressure was also initiated and yielded results that would be useful for subsequent studies.

## TABLE OF CONTENTS

## LIST OF TABLES

## LIST OF FIGURES

# 1.0 OBJECTIVES, SCOPE OF WORK AND DISSERTATION STRUCTURE

Understanding the mechanics of rock cutting and developing a credible modeling framework has important implications across a diverse field of applications ranging from drilling for oil production, mining for coals and minerals, tunneling and underground cavern construction, among others. From a modeling perspective, rock cutting analysis poses a daunting challenge. This study consists of two main objectives: (1) to develop a framework for modeling rock cutting as posed by the laboratory rock scratch test using the discrete element method, and (2) to investigate the validity of the implicit modeling of rock porosity incorporated into discrete element modeling.

This study focused on the modeling of rock cutting under ambient pressure environments, with only limited efforts devoted to an exploratory investigation of the high pressure effects. During rock cutting, two modes of rock failure were observed. For a shallow cut, a rock experiences a ductile or plastic mode of failure; however, for a deep cut, a rock experiences a brittle or fracture mode of failure. This study is limited to the study of ductile failure as this is generally the mode of failure imposed by controlled rock cutting. Rocks included in the model possessed a wide range of strength values, and their uniaxial compressive strength values varied from 15 to 200$MPa$.

This work is comprised of five additional chapters, which can be summarized as follows:

**CHAPTER 2:** The **LITERATURE AND METHODOLOGY REVIEW** section presents the state-of-the-art development of the topics under study. This

allows for the formulation of specific inquires that have yet to be addressed and for the identification of important contributions in the field of geomechanics. The methodology comprises the procedures followed through the study in order to calibrate the DEM model.

**CHAPTER 3:** The Rock Scratching Test is modeled using the PFC2D, and to a lesser extent, the PFC3D. It is the goal of this chapter to obtain the cutting specific energy for rocks with strengths that span from very low to very high values and are similar to those obtained in laboratory results. Several factors and their effects on this model were investigated, among them, the influence of crushing and the particle size sensitivity. Ultimately, the DEM model was calibrated using particle size effects and was found to match well with results obtained from laboratory testing.

**CHAPTER 4:** The established DEM model was used to investigate the effects of implicitly modeling porosity. A first attempt to implicitly model porosity consisted of considering only varying microproperties in order to account for the inherent material differences of rock samples with different porosities. Ultimately, while some macroproperties did align between the samples with different porosity, it was required that simulated microdefects be included. This final adjustment, including developing optimal levels of microdefects for rock samples of different porosities, allowed for implicit porosity modeling. Finally, results from the RST are used to ensure the adequate implicit modeling of porosity.

**CHAPTER 5:** Several contributions and potential projects which exceeded the scope of this study are presented in this chapter for possible future work.

Specifically considered and suggested are investigating the effects of the initial stress state on the behavior of the DEM model, further clarifying the confinement pressure boundary, re-evaluating the microproperties utilizing statistical analysis, and introducing pressure to the rock cutting process.

**CHAPTER 6:** Overall conclusions to this work as well as contributions in both industrial and future research applications are presented in this chapter.

# 2.0 LITERATURE AND METHODOLOGY REVIEW

The review of literature for this dissertation focuses on two main topics: 1) the behavior of rocks under pressure and 2) the numerical modeling of rock mechanics under a pressurized environment using the Discrete Element Method (DEM). First, a brief review of the DEM formulation implemented in the Particle Flow Code (PFC) and the contact model used for modeling rock are presented. Then, a basic description of the scratching test characteristics is provided for the specific case of a sharp cutter and a shallow cut.

## 2.1 DISTINCT ELEMENT METHOD IN PARTICLE FLOW CODE

### 2.1.1 Distinct Element Method

The Distinct Element Method is a specific application of a broad numerical method named the Discrete Element Method. The Distinct Element Method is first laid out by Cundall [5] for rock mechanics analysis and is subsequently applied to soil mechanics problems by Cundall and Strack [6]. In the Discrete Element Method, each discrete element or particle, has three degrees of freedom, namely, two translational and one rotational, in a two-dimensional setting. At each time step, a rigid body dynamics equation is solved for each particle. The interaction between

particles is modeled through the penalty method in which very stiff springs are used to both prevent excessive particle overlap and enable the computation of forces between particles.

The solution method used for solving a particle system is based on the explicit finite-difference method. The explicit method scheme requires a fine time-step for stability and accuracy considerations while avoiding the need to solve simultaneous equations.

The time-stepping algorithm assumes that both the velocity and acceleration are constant inside each time step. The maximum time-step that can be used is dictated by the fundamental period of the system. Because of the high stiffness used, the time step is very small often on the order of $10^{-9}$ seconds.

At each time step, the equation of motion is solved for each particle. Both external loads and interaction with neighboring particles contribute to the force terms. The interaction forces or contact forces are updated using the force-displacement law from the relative motion at each point of contact.

### 2.1.2 Contact Model

In the 2D DEM, displacement constraints are imposed by both employing rigid walls and modeling circular particles, referred to as balls. Accordingly, two types of contact are encountered, ball-ball and ball-wall. Therefore, a contact model can dictate the behavior of these two interactions by defining the following characteristics:: 1) stiffness, which relates the relative displacements to the contact force; 2) slip, which provides a relationship between normal and shear forces; 3) damping, which achieves steady state by dissipating kinetic energy; and 4) bonding, which allows particles to be bonded together. There are two types of bond: (1) contact

bonds, which can transfer force only; and (2) parallel bonds, which can transfer both forces and moments.

The linear stiffness model is the simplest model in which the stiffness maintains a constant value until failure occurs. This method can be used to model both normal contact and shear contact between particles as shown in Figure 2.1, which depicts a linear normal contact, the left side and a linear shear contact on the right side. This normal contact is removed when a particle loses contact or the spring is subjected to net tensile force. A shear spring fails, as represented by a slider (refer to $\mu$ in Figure 2.1), when its strength, often defined by the Mohr-Coulomb law, is exceeded.

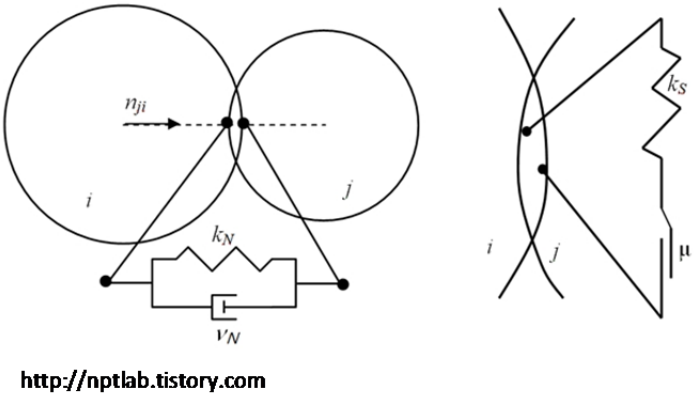


**Figure 2.1** Linear model implementing stiffness, slip, and damping at contact

To model a rock sample in DEM, in this study, the rock is modeled by the Bond-Particle Model (BPM) of Potyondy and Cundall [3], in which particles are cemented together with bonds. First, an assembly of circular particles is created following a specified grain size distribution. This assembly is then packed under a preset level of compressive stress and bonded together at the points of contact between particles. The particular type of bond used is called the parallel

bond which can be visualized as a finite-sized piece of cementitious material with its diameter proportional to the minimum diameter of the two particles that a bond cements (as depicted in Figure 2.2) or as a prism in a special case of 2D analyses.

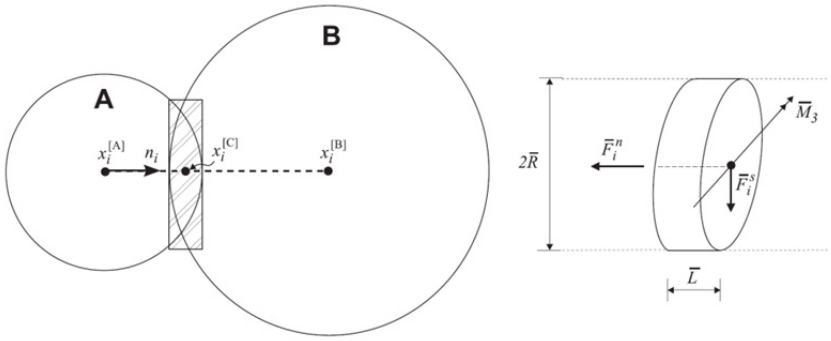


**Figure 2.2** Parallel bond visualization as a cylinder of cementitious material [7]

The parallel bond acts in parallel with the linear model, and the sliding characteristic of the linear model are applied when the bond does not exist. The cementitious material can be imagined, rheologically speaking, as a set of uniformly distributed springs over the finite region of the bond. The spring forces and moments can be related to maximum stresses acting within the bond periphery, and a bond can be broken when a Mohr-Coulomb failure envelope, depicted in Figure 2.3, is exceeded by the bond stresses. A model created with the parallel bonds is called herein the bonded-particle model (BPM).

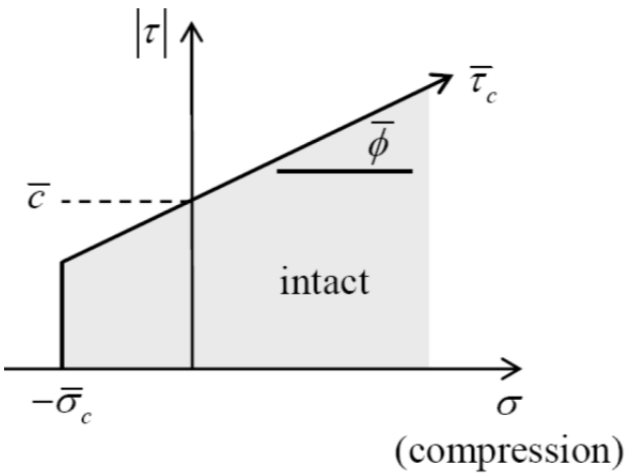


**Figure 2.3** Parallel bond failure envelope [7]

The last contact modeled developed by Potyondy [8] is called the flat-jointed bonded-particle model, where the limitation found in the bonded-particle model is addressed, that is, if the model is calibrated by matching the uniaxial strength ($\sigma_c$) by means of the BPM, the resulting tensile strength ($\sigma_t$) values will be too large and the $\sigma_c/\sigma_t$ ratio is lower than expected. This is resolved by the introduction of a grain structure created by polygons, where granular interlocking is a main structural component that not only provides rotational restraint but also considers the effects that this rotation will create, such as the transfer of moments to the neighboring grains as described by the author in Figure 2.4. The grains can be bonded between each other on their interfaces as the parallel bond model; however, the rotational effect of the grains will still be active if the bonds fail which does not occur on the BPM. Potyondy assures that the flat-jointed bonded-particle model supersedes the former bonded-particle model due to the capabilities of reproducing more micro and macromechanical responses parallel to rock damage.

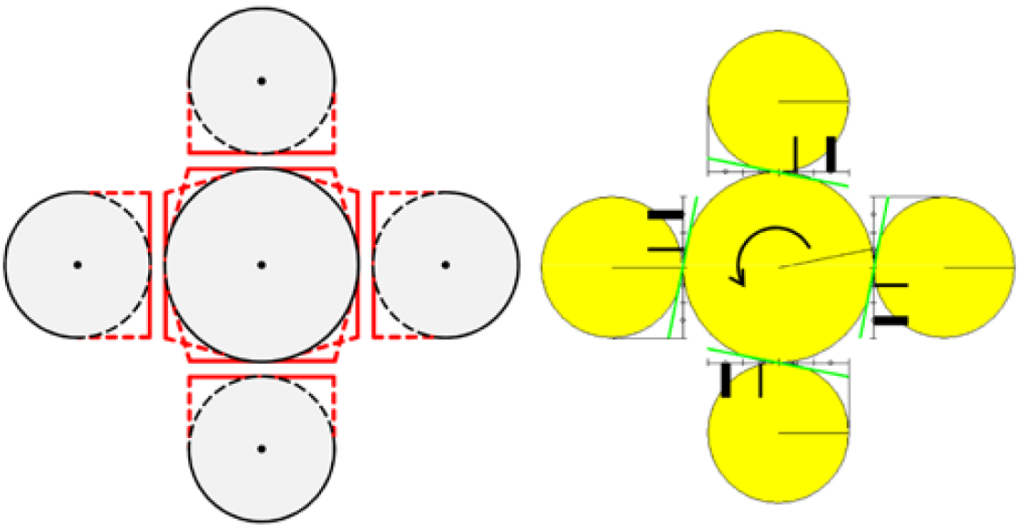

**Figure 2.4** Interface geometry of interlocked grains (left) and moment transference due to the rotation restraint of the middle particle (right) [8] [1]

### 2.1.3 Calibration of a Discrete Element Model for Rocks Under Pressure

Several approaches have been used for calibrating rocks using the DEM. The bonded-particle model (BPM) was extensively investigated by Potyondy and Cundall [3] for the calibration of rock-like materials using the parallel bond contact model. The calibration procedure is well described in the Itasca Manual [9]. However, it is emphasized that the BPM

[1] "Effective interface geometry of interlocked grain modeled with four unbonded flat-joint contacts (left) and segment forces and interface gap after rotating the central particle while keeping the surrounding particles fixed (right). Compressive forces develop at the far end of each interface that resist the moment applied to the central particle" Potyondy [8] Potyondy DO. A Flat-Jointed Bonded-Particle Material for Hard Rock. In: The 46th US Rock Mechanics / Geomechanics Symposium - ARMA, Chicago, IL, 2012. 10.

contains limitations for reproducing the desired failure envelope in a pressurized environment (Figure 2.5).

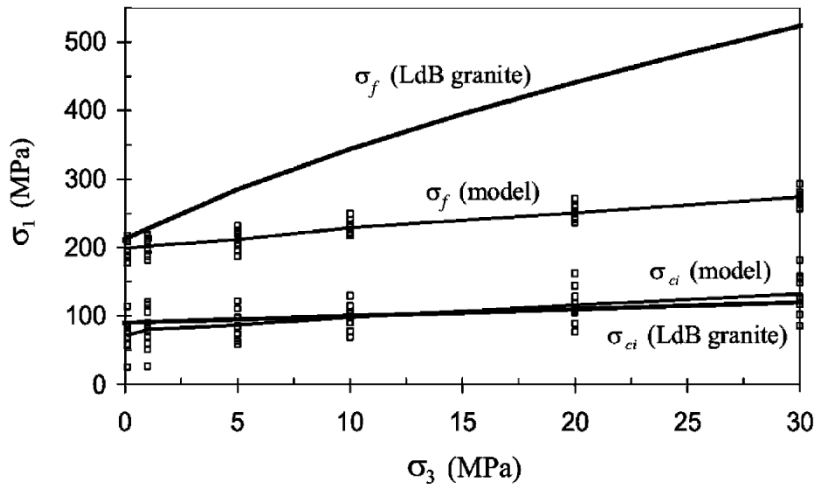


**Figure 2.5** PFC2D results in Lac du Bonnet granite [3]

However, the pressure dependent behavior of rocks with high pressure dependence is not captured accurately by stress-strain curves. In Figure 2.6 (a) three stress-strain curves under 0.1, 10 and 70 MPa confinement pressure are depicted. It is apparent that the stiffness of the rock does not change as a function of the confinement, which is not representative of sedimentary rocks such as sandstones, e.g., Figure 2.6 (b).

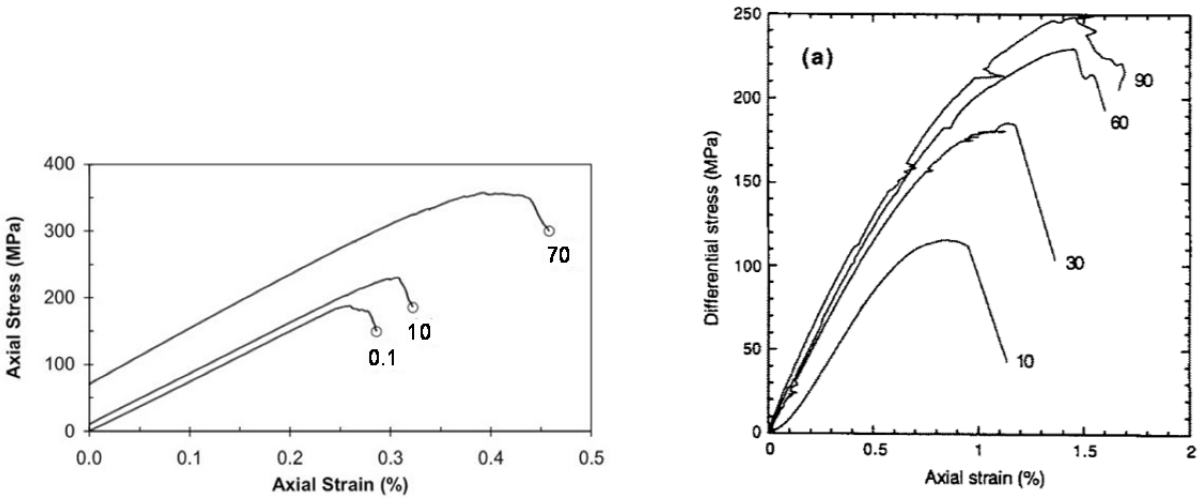


**Figure 2.6** **S**tress-strain curves of (a) PFC2D simulation of Lac du Bonnet granite [3] and (b) Bentheim sandstone

The failure envelope can be improved by the introduction of unbreakable clusters to produce complex grain interlocking as seen in Figure 2.7. The resulting failure envelope shape is dependent on the amount of particles per cluster and it can be seen that a higher density of particles in the cluster produces a higher angle of internal friction. It is worth mentioning that the work of Potyondy and Cundall [3] was conducted while the parallel-bond model was in an early stage of its development, and the normal and shear strength were dictated by constants, i.e., it was not pressure dependent.

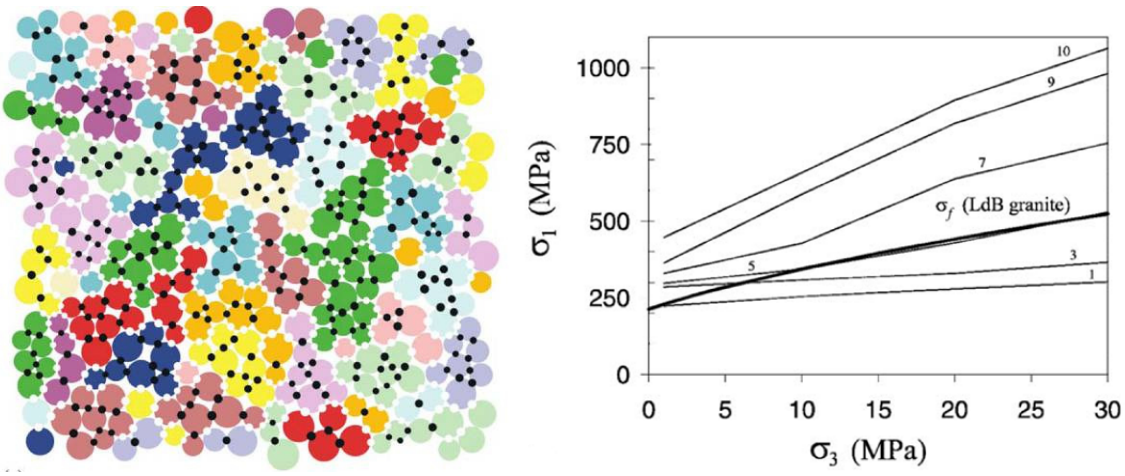


**Figure 2.7** (a) Geometry of clusters in PFC2D, where the black dots represent unbreakable bonds and white dots the boundary breakable bonds; and (b) failure envelope in function of the mean number of particles in a cluster [3]

The BPM model was improved by Cho et al. [10] by employing a clump model, where clumps are seen as unbreakable clusters that behave cohesively as a rigid body. This implementation improved the ratio between the unconfined compressive and tensile strength that was observed as relatively high in Brazilian tests by Potyondy and Cundall, and in direct tension tests by Diedrichs [11]. Furthermore, a very accurate failure envelope for the Lac Du Bonnet granite is obtained by Cho et al. [10] using the clump model as depicted in Figure 2.8.

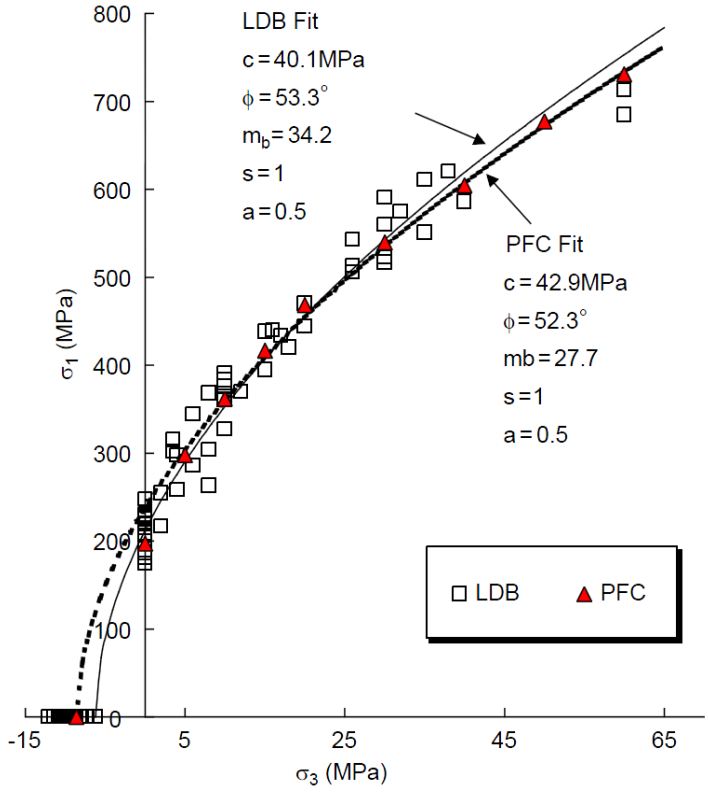


**Figure 2.8** Failure envelope prediction with PFC results using the clumped particle model [10]

Although the failure envelope was improved by implementing clumps and clusters, a more recent work on granular bonded material [12] using PFC was able to capture pressure dependent behavior through the employment of ductile and fragile behaviors for shear and normal strength in the contact bond. Wang and Tonon [13, 14] argue that tensile and shear failure jointly control the strength of the material. In their work, the tensile failure occurs after the tensile strength has been exceeded, and the tensile forces then approach zero. In parallel, the shear strength follows a Mohr-Coulomb failure criterion, that when surpassed leads to failure. Following failure, the residual friction drives the shear strength. Additionally, Wang and Tonon implemented a membrane boundary, depicted in Figure 2.9, for applying confinement pressure. This boundary is comprised by the outer particles of the sample. This “boundary condition” adds

a more realistic failure pattern that cannot be achieved when the external pressure is being exerted by rigid walls. By incorporating these changes, Wang and Tonon were able to improve previous results obtained by Potyondy and Cundall, as shown in Figure 2.9.

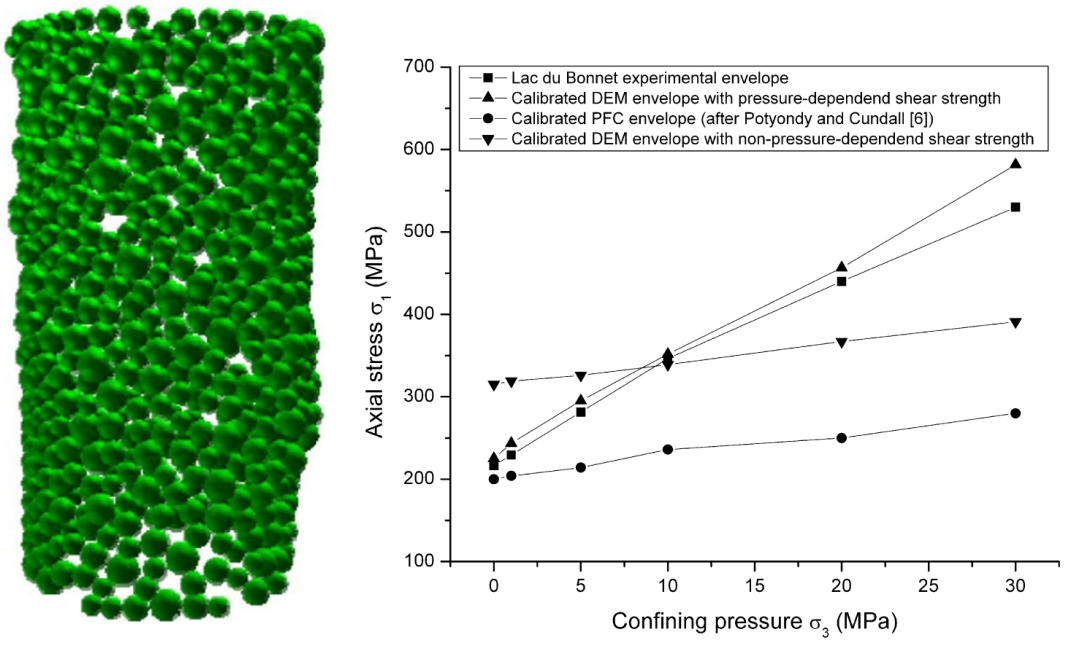


**Figure 2.9** Lac du Bonnet granite simulation: (a) Membrane boundary depicting bulging and (b) failure envelope [13]

The literature presented, though focused on the calibration of rocks under pressure, lacks consideration of simulated confinement pressures exceeding 70 MPa. This limitation offers an opportunity to address the problem of simulating rocks and their behavior under high pressure. Work by Ledgerwood [15] investigated this limitation. The calibration of a Carthage marble using PFC is conducted using a similar membrane boundary but created under a more robust algorithm that comprises extreme modification of the surface where pressure is applied. This boundary condition showed a strain localization failure mechanism (shear band) under low pressures and shear-enhanced compaction in the high pressure condition; however, the latter is

not well represented as depicted in Figure 2.10. The author's description of the figure follows: the light gray color represents particles in which all bonds have failed; particles with intact bonds are shown in dark gray; and the particles with black dots on the edges represent the surface where the horizontal pressure is being applied. Based on the results shown in Figure 2.10, the simulated rock specimen under high pressure would be pulverized after failure. This disagrees with laboratory results that show the behavior of rock under high pressure undergoes a transition from brittle to ductile, passing through different phases such as crushing, compaction, and cataclastic flow, among others.

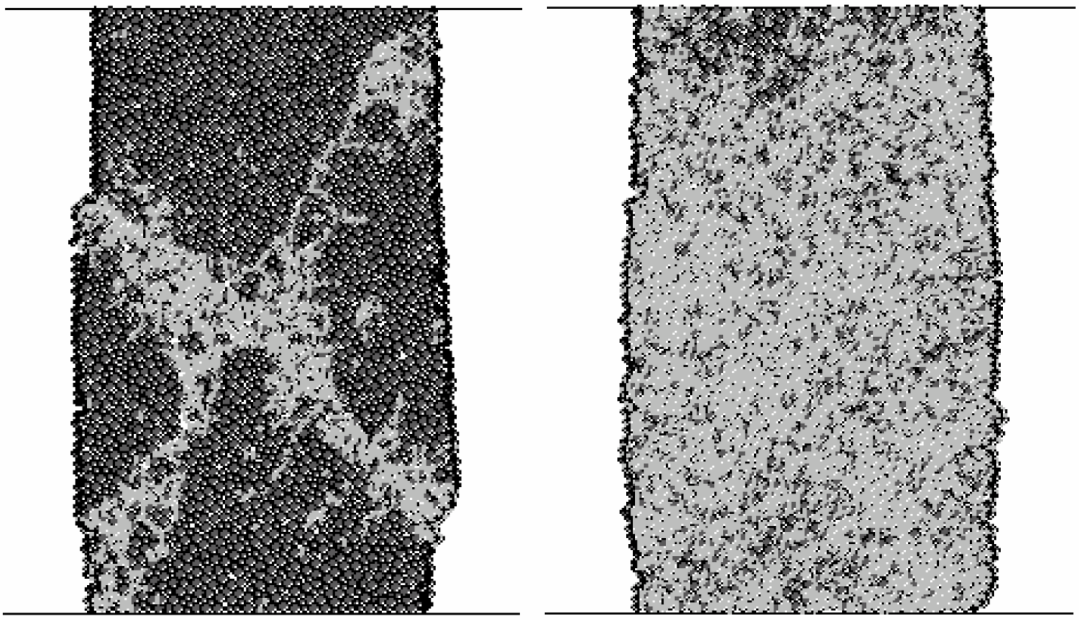

**(a)** **(b)**

**Figure 2.10** (a) Strain-localization mechanism and (b) shear-enhanced compaction band according to Ledgerwood [15]

The stress-strain curves obtained in Ledgerwood's simulation led to important conclusions of the rock behavior under different pressurized environments. It is clear that when

the rock experiences low pressure, the failure tends to be brittle as shown in the 7 MPa confinement case in Figure 2.11. The stress-strain relationship should evolve as a function of the confinement where the post-yielding transitions from softening to hardening. This agreed well for samples with confinement pressures less than 70 MPa but when the confinement pressure increased, the hardening, clearly shown in the laboratory results, fails to be captured. An important motivation for this research lies in investigating the relationship between high pressure rock samples and hardening and most efforts are focused on the reproduction of the evolution of stress-strain behavior of rock samples under different states of stress.

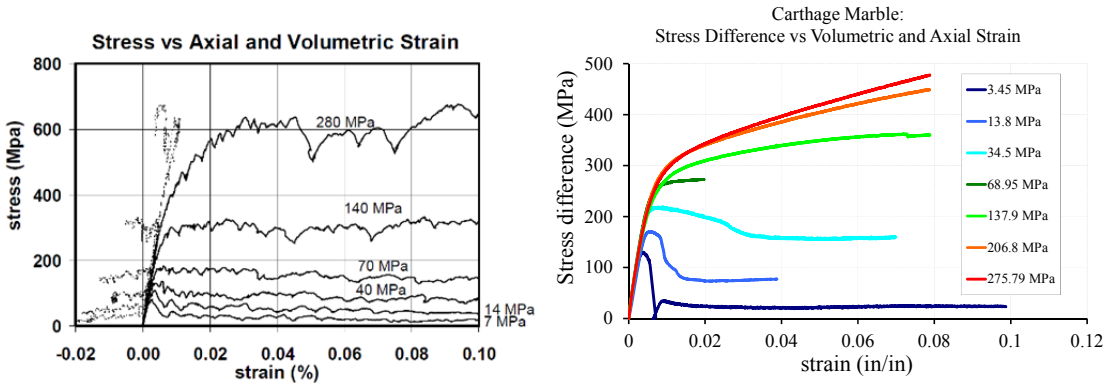


**(a)** **(b)**

**Figure 2.11** (a) Simulation and (b) laboratory stress-strain curves of Carthage marble [15]

## 2.2 SYNOPSIS OF THE ROCK SCRATCHING TEST

The Rock Scratching Test (RST) will be the basis for validating the modeling effort of this study. In this test, the cutter moves in a linear fashion into a rock sample. The rationale is that there is no sense in attempting to model sophisticated drilling bit action, unless this much simpler

problem can be reproduced in a satisfactory manner. The following section explains briefly the RST scheme, and how it has been modeled to date.

### 2.2.1 The Rock Scratching Test as a technique

In the oil industry or any other industry which requires that a natural resource be extracted, drilling is one of the most critical and expensive stages of an extracting project. Even though the importance of drilling to resource extraction is widely accepted, the phenomenon of well drilling lacks a strong theoretical approach with respect to the interaction between the rock and drag bit. The Rock Scratching Test (RST) is a laboratory test performed over either a slab or a cylinder obtained from a rock core. The rock specimen is scratched in a single direction throughout the sample, using a cutting tool which mimics one of the tips of a drill bit or drag bit, used for well drilling [16]. The purposes of the RST are: 1) to register the horizontal force acting on the cutting tool, and 2) to observe the failure behavior of the rock. Hence, the Uniaxial Compressive Strength (UCS) can be well estimated based on the cutting mechanism observed in the experiment, and the forces acting on the cutting face [17, 18].

Based on experimental observation, Richard [17] concluded that two cutting modes in the rock cutting process take place in the RST. They are: 1) a “ductile” failure mode occurring at shallow depths (generally less than 1mm) associated with crushing of particles at the tool tip and shearing of the rock in front the cutter and 2) a brittle mode occurring at greater depths (generally more than 1 mm), characterized by macroscopic cracks that initiate from the tip of the cutter creating uneven paths of failure ahead of the cutter. The two types of failure modes are depicted in Figure 2.12.

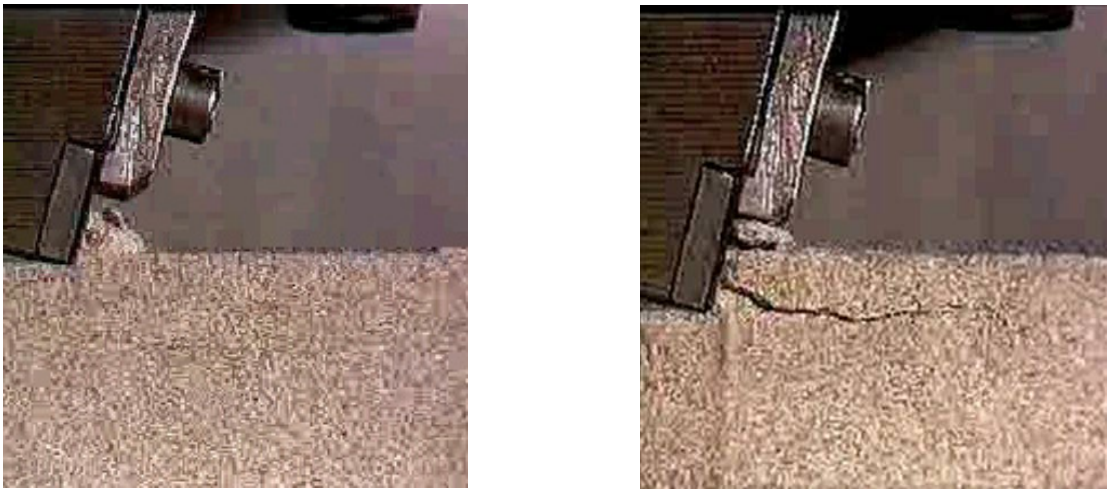

**(a)** **(b)**

**Figure 2.12** The Rock Scratching Test: (a) a ductile failure mode and (b) a brittle failure mode

It was found during the shallow cutting process that the uniaxial strength is related to the specific energy of cutting. The specific energy of cutting is defined by Richard as the energy required to cut a unit volume of rock.

$$\varepsilon = \frac{F_S}{wd}$$

**Equation 2.1**

Equation 2.1 presents the relation between the specific energy, $\varepsilon$, and the mean horizontal force on a shallow cutting, $F_S$,here $w$ and $d$ respectively stands for the width of the cross-sectional scratched section and the depth of cutting.

The Rock Strength Device (RSD) is used to perform the RST. The size of the rock sample (cores) that can be used in the RSD range from 30 *mm* to 120 *mm* in diameter, and 20 *mm* to 1000 *mm* in length according to Schei et al. [19]. In addition, the length of the groove

scratched has to be at least 10 times the depth of the cutting. Thus, a sample subjected to shallow cutting can offer good results after 10 *mm* of a cutting process. A more detailed description of the apparatus and the configuration of the test was presented by Richard and Dagrain et al. [2, 17]. Furthermore, Dagrain et al. presented more updated characteristics used in the RSD, depicted in the table below. Overall, the beauty of the RST is that the results obtained, regardless of the rock-like material used, show that the scattered data are concentrated in a one-to-one relationship of specific cutting energy and unconfined compressive strength.

**Table 2.1** Rock Scratching Device characteristics [2]

| $\theta$ (°) | *w (mm)* | *v (mm/s)* | *d (mm)* | *L (mm)* | $F_s$,$F_n$(N) |
|---|---|---|---|---|---|
| 15 | 10 | 4-10 | 0.1-1 | 200-1000 | 0-4000 |

The data points shown in Figure 2.13 were obtained in three different laboratories located in the USA, France and Belgium (Showing the effectiveness of the method) and using different types of rocks, rock-like materials and construction materials. In total, 252 materials were tested. There is another source of information, where more materials are added to the curve, published by the company Epslog Engineering in a brochure for their Wombat apparatus (http://www.epslog.com/files/brochure_11-06.pdf). While this brochure is not an academic reference, it gives a state-of-the-art view of the RST test.

**Table 2.2** Rocks subjected to the RST [2]

| Material | Samples tested |
|---|---|
| Sandstone | 92 |
| Limestone | 86 |
| Shale | 19 |
| Dolomite | 6 |
| Chalk | 4 |
| Granite or Granodiorite | 3 |
| Coal | 2 |
| Anhydrite | 2 |
| Construction materials | 17 |
| Refractory | 3 |

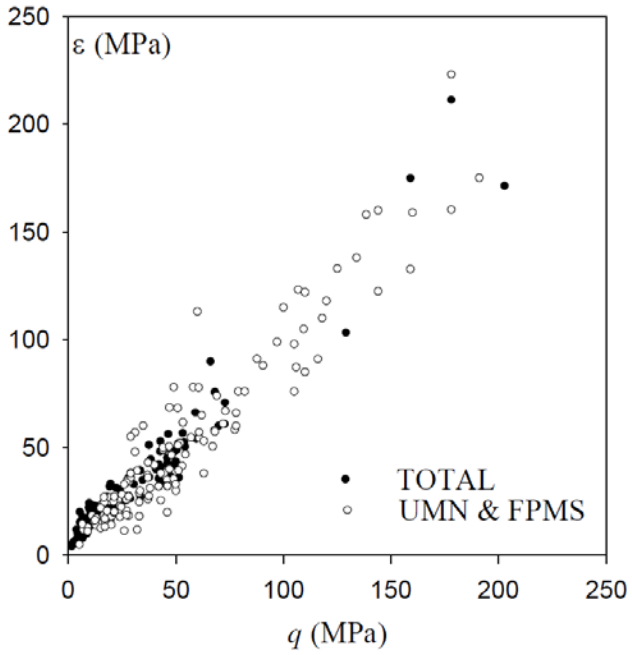


**Figure 2.13** Correlation between the cutting specific energy and the unconfined compressive strength [2].

### 2.2.2 Rock Cutting Test Under Pressure

Unfortunately, there is no data available of an RST in slab cutting. Kaitkay and Lei [20] performed a groove circular rock cutting test under hydrostatic pressure. The effects of the hydrostatic pressure assisted the cutting process with the chip formation and presented a nonlinear trend of cutting force against pressure as shown in the figure below.

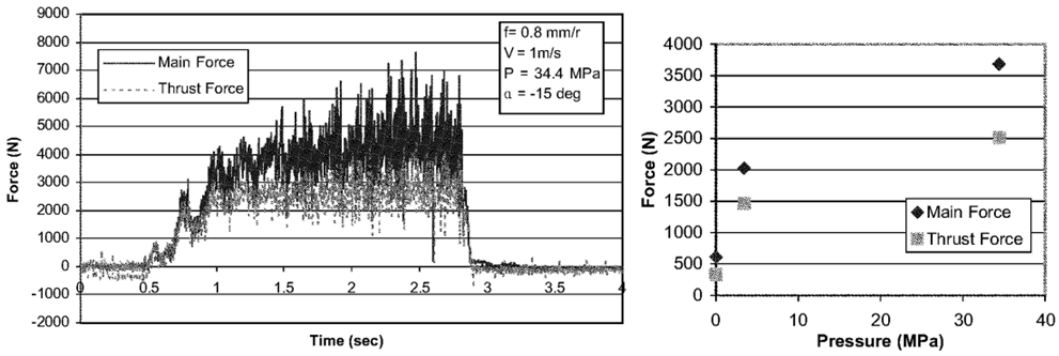


**Figure 2.14** Rock Cutting Test under hydrostatic pressure: Left side, force history; and right side, force vs. pressure

Although this is not a two-dimensional case, we can use the cutting force history and the mean cutting forces as a frame of reference for our simulations.

### 2.2.3 Discrete Element Modeling of RST

In general, the DEM modeling of rock cutting has been performed taking into account the following conditions: 1) The rock is modeled as a BPM, 2) the walls containing the specimen are boundary conditions at zero velocity, and 3) the cutting tool is a segmented wall, representing a boundary condition at a constant velocity. The nature of the rock being a BPM and the cutting tool a rigid body, allows for identification of the damage in the bulk material and the recording of the forces acting in the cutting process, respectively.

The different failure modes in rock cutting was modeled by Huang et al. [21, 22]. They found that the depth of cutting determines whether the failure regime is ductile or brittle when a characteristic particle size is given. The authors also found a fair relationship between specific energy of cutting and the unconfined compressive strength of the sample.

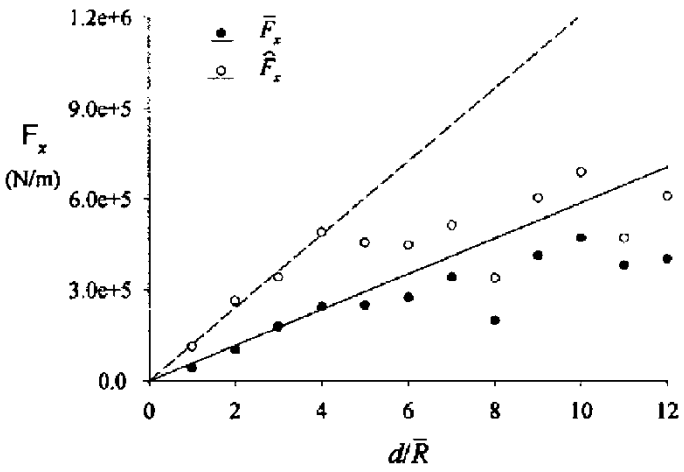


**Figure 2.15** Linear trend of force vs. depth in the RST simulation [21]

DEM has also been used by Rojek [23] in rock cutting simulation with the purpose of validating the cutting force results with the existing analytical approaches of Nishimatsu [24] and Evans [25]; however, this study does not specifically refer to the scratching test or the shallow cut. Moreover, the study shows an interesting failure pattern that characterizes a deep cutting depth as shown in Figure 2.16.

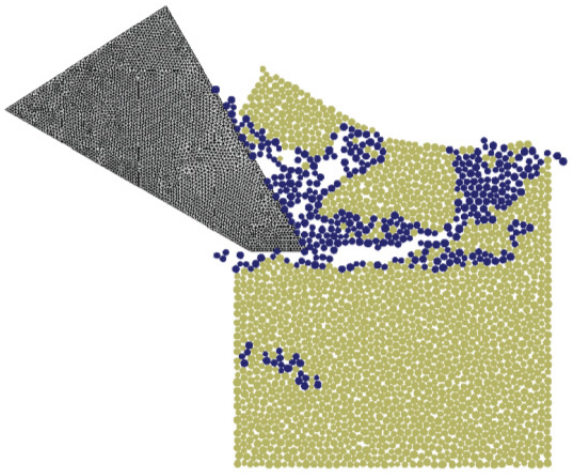

**Figure 2.16** Brittle failure in rock cutting **[23]**

Huang and Detournay [26] investigated that the switch from ductile to brittle failure mechanisms can be explained by the introduction of a length scale parameter in the rock description which is a function of the material toughness and the uniaxial strength. The investigators claim that the mean radius loses its quality of discretization parameter and becomes dependent on the toughness and the uniaxial strength. Thus, when the length scale is introduced, the failure behavior is controlled by the strength of the mechanical properties of the material.

**Figure 2.17** Ductile and brittle failure due to cutting depth and particle size ratio [26]

A latter study by Rojek, [27] evaluates the 2D and 3D simulation of rock cutting with a single roadheader pick and compares these results with records obtained experimentally. Rojek concludes that the numerical results are quite agreeable with those obtained in the physical lab. Moreover, it is pointed out that the lack of full geometrical representation in the 2D case yields to results that can be fulfilled by 3D analyses. This is supported by the means and standard

deviations of the forces obtained during the experiment which are compared side by side with the ones from the simulation as shown in Figure 2.18.

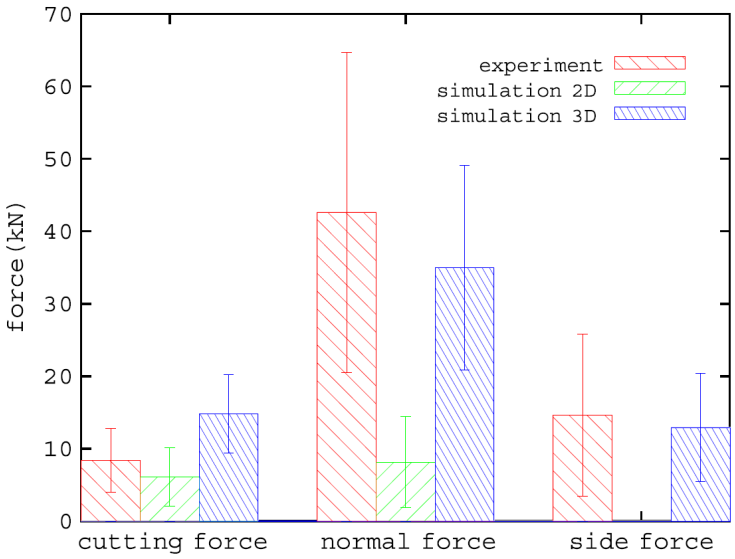


**Figure 2.18** Comparison of the mean force histories of the rock cutting process[27]

The simulation of rock cutting using a point attack pick under a PFC3D simulation environment was explored by Su and Akcin [28]. This study, along with experimental results, found that theoretical models of rock cutting (Evan's, Lui's and Goktan's models), are comparable with simulation results. The figure below depicts the relationship between laboratory and simulation cutting forces results, and the cutting process in the simulation.

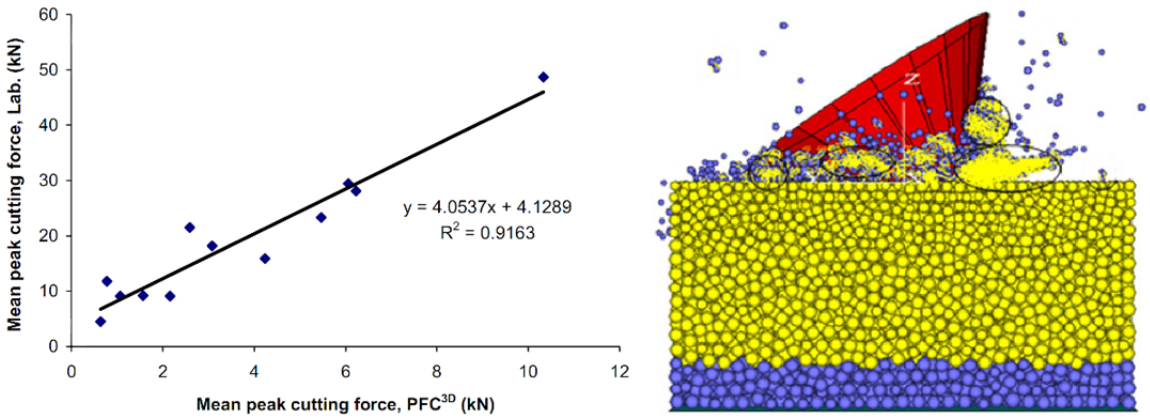


**Figure 2.19** Comparison of the mean force histories of the rock cutting process [28]

### 2.2.4 Discrete Element Modeling of RST under Pressure

Lei et al. [29, 30] has explored the use of DEM in modeling rock scratching tests by performing studies on the influence of hydrostatic pressure on orthogonal machining and sensitivity analyses of the micro-properties of the numerical model. The authors suggest that the increment of particle size towards the bottom of the sample decreases the computational expenses without affecting the macro-properties of the material. The particle arrangement used in their simulation is shown in the figure below.

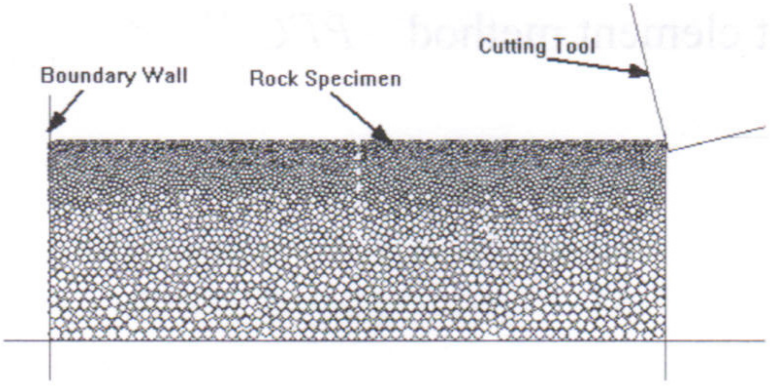


**Figure 2.20** Specimen setup and boundaries for rock cutting [29]

The findings in these studies are that: 1) the hydrostatic effect restrains crack growth and creates larger horizontal forces during the cutting process (Refer to Figure 2.21), 2) the failure in the absence of confining pressure implies short-chip formation, crack propagation and smaller cutting forces (Refer to Figure 2.21), 3) the damping coefficient has a large effect in the cutting forces, therefore a more realistic value is necessary for having results closer to reality, and 4) the shape of the particles for avoiding the spinning that the circular elements allows also affect the results, suggesting further research in the implementation of clusters in the specimen.

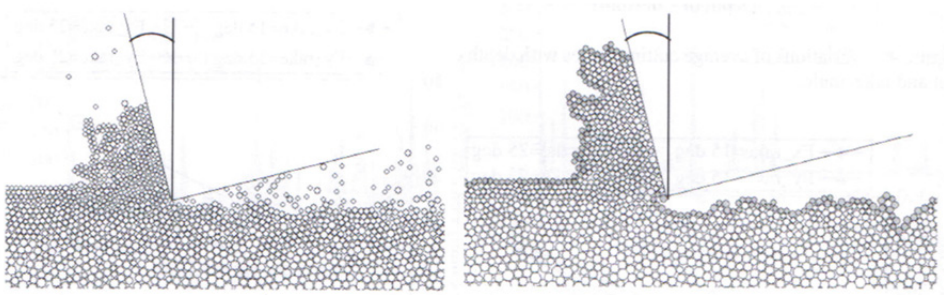

**Figure 2.21** Rock cutting process with and without confinement, left and right, respectively [29, 30]

The relation between failure mode in drilling and bottom hole pressure was investigated by Block and Jin [31] using DEM. Here, the energy dissipation was addressed not just as the breaking of the bonds, but also the irreversible reorganization of the grain structure. This issue was accounted for by calculating the average stress tensor and the strain rate on a grain within a given neighborhood. A cap-like failure envelope was considered in the post-processing of the results to determine whether the state of stresses on analyzed regions were behaving elastically, or failing either in a brittle or ductile mode. Moreover, it was found that the cutting morphology is affected by the *in situ* pressure conditions and the weight of the PDC bit. The case of

atmospheric conditions is shown in Figure 2.22(a) while the case of down-hole conditions is shown in Figure 2.22(b).

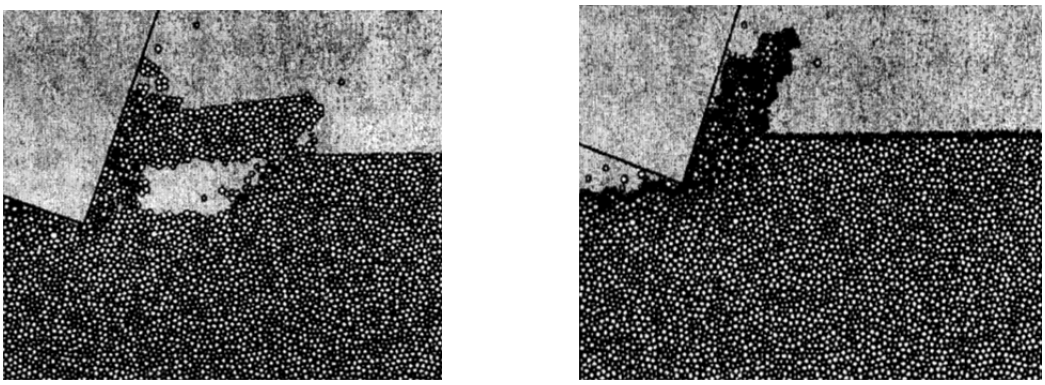

**(a)** **(b)**

**Figure 2.22** Visualization of cutting morphology using DEM at (a) atmospheric conditions and (b) down-hole conditions (30 MPa)

Also, qualitative characteristics were observed in the rock cutting simulation under pressure using PFC2D and reported in [15]. The reported characteristics include the efficiency of the cutter backrake angle and cutting depth, the flow of crushed material below the cutter, as depicted in the Figure 2.23, and some other confidential characteristics.

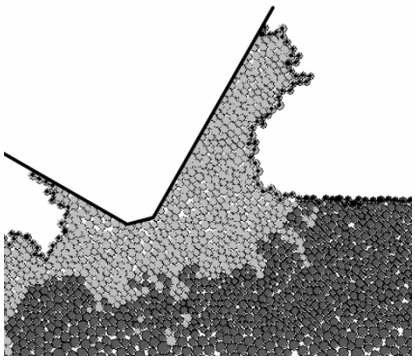

**Figure 2.23** Cutting process using PFC2D under 20 MPa of pressure

To summarize, there has yet no comprehensive modeling effort that has duplicated the relationship between the specific energy and the uniaxial strength as observed in the laboratory rock scratch tests. There is neither a detailed study on the validity of implicit modeling of porosity using the discrete element method.

## 2.3 METHODOLOGY

### 2.3.1 Sensitivity Analysis

The general test procedure and the material property selection for the DEM numerical model are described in this section. The calibration of the material using the Unconfined Compressive Strength test results and the aim of choosing a variety of rock-like materials in the numerical model are explained.

The DEM numerical model requires a set of microparameters characteristic of the bonded-particle model. These microparameters refer to the properties of the model entities, namely, particles and walls. The focus of this study lies in the direct analysis of the microproperties with the particles and their corresponding contact model.

A large number Unconfined Compressive Strength tests using the DEM were conducted to evaluate the sensitivity of the microproperties and to analyze their influence on the macroproperties. This analysis is useful in order to ensure that the selected microparameters yielded reasonable rock samples and are able to predict sets of microproperties based on target macroproperties. The results of this analysis are summarized herein, where each data point represents the average of three different samples. The results of this sensitivity study provided

guidance for the selection of microparameters to manipulate and their influence on the macroproperties. For example, in order to increase the uniaxial strength of the rock, the sensitivity study provided insight into which parameters should be changed and by what degree in order to obtain the desired results.

The sensitivity study produced the following conclusions:

- When the particle stiffness ratio, $k_n/k_s$ exceeds one, the Young's modulus is largely unaffected. However, when the ratio of the particle stiffness is larger than the ratio of the parallel bond stiffness, represented by $b$ in Figure 2.24, the Young's modulus of the material increases with respect to the Young's modulus of the particles.
- The Poisson's ratio is very sensitive when the $k_n/k_s$, is less than 2. Moreover, increasing the bond stiffness ratio can increase the Poisson's ratio. This can be observed in Figure 2.25.
- The uniaxial strength was found to be dependent on both the particle and bond stiffness as shown in Figure 2.26. When the bond particle stiffness ratio is significantly larger than the particle stiffness ratio, the uniaxial strength displays erratic behavior when the $k_n/k_s$ ratio is less than one. However, when the particle stiffness ratio is equal or larger than the bond stiffness ratio, and the normal stiffness of the particle is larger than its shear counterpart, the uniaxial strength shows more stability.

- The bond strength ratio, namely, shear to normal bond strength, represented by the variable *b* in Figure 2.27, proved to influence the Young's Modulus of the material when this ratio is less than or equal to one.
- Finally, the uniaxial strength of the material has a tendency of being very sensitive to subtle changes of the normal bond strength when its value is less than 100*MPa*, regardless of the strength ratio. Figure 2.28 shows that materials with high uniaxial strength are inherently more stable than those characterized by low uniaxial strength.

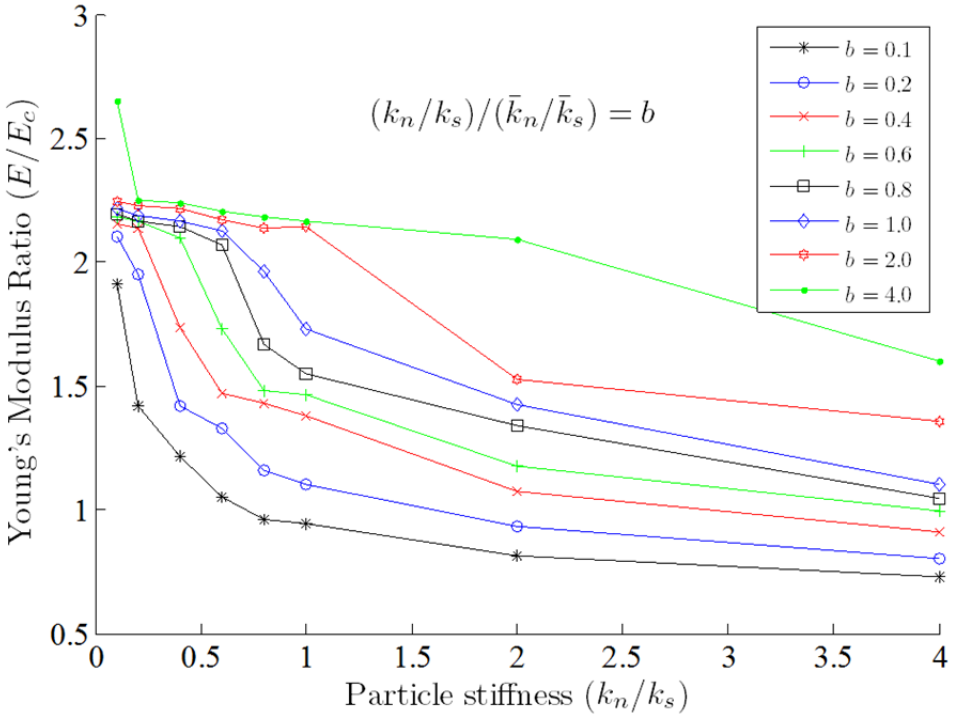


**Figure 2.24** Sensitivity of bond and particle stiffness ratio on material stiffness

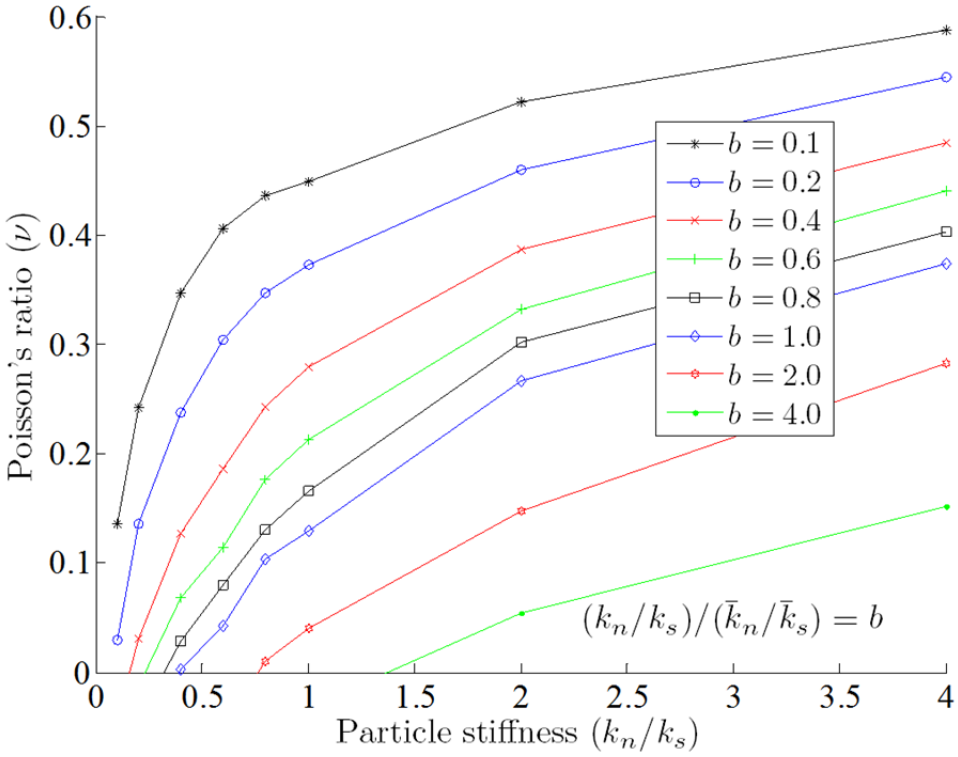


**Figure 2.25** Sensitivity of bond and particle stiffness ratio on Poisson's ratio

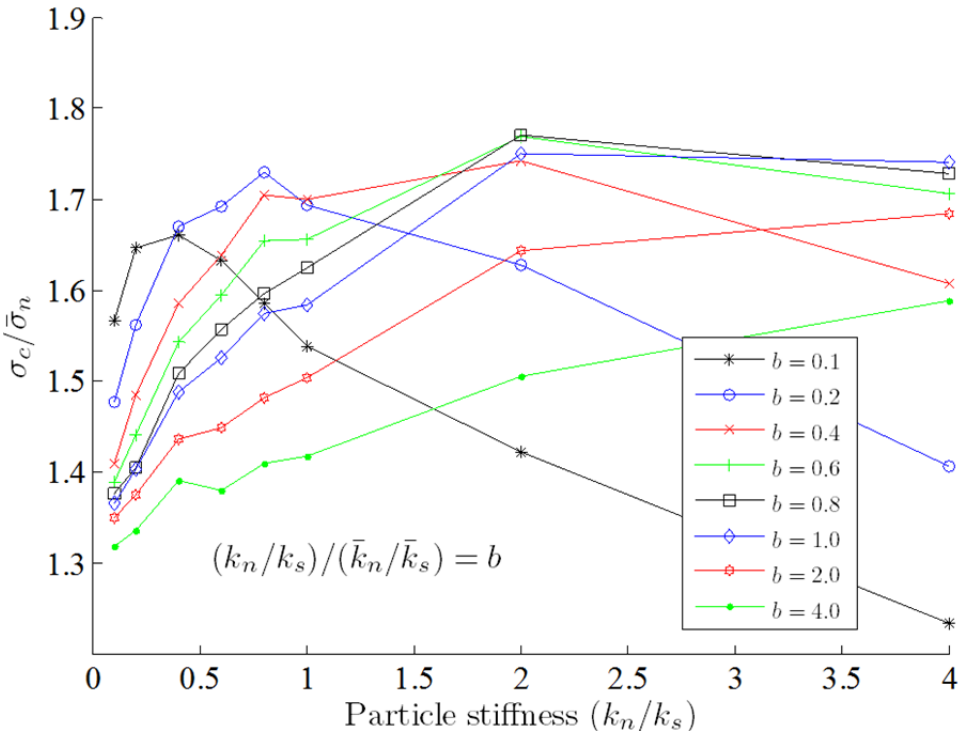


**Figure 2.26** Sensitivity of bond and particle stiffness ratio on material strength

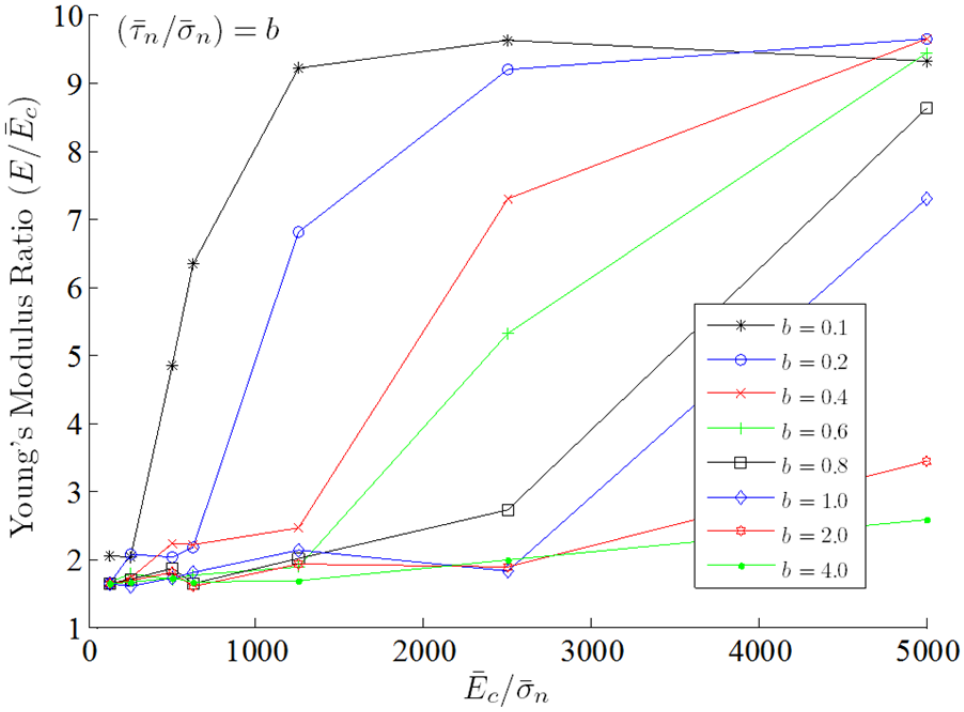


**Figure 2.27** Sensitivity of bond strength ratio on particle and material stiffness

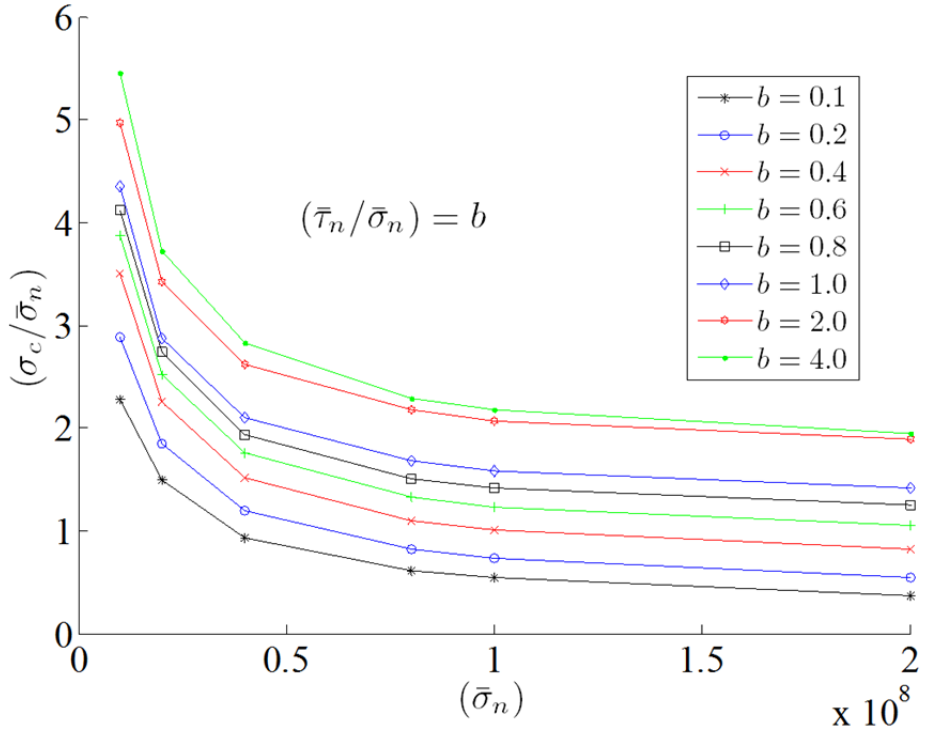


**Figure 2.28** Sensitivity of bond strength ratio on material strength

### 2.3.2 Generating Samples with Different Porosities

Modeling rocks as an assemblage of particles bonded together using discrete elements has allowed for a new approach to the study of mechanical rock behavior [3]. It has significantly impacted the failure analysis, particularly in the area of fragmentation and fracture. The discrete element model adopts a host of micro mechanical parameters to define a rock, which includes the stiffness, surface friction and cohesion of the particles, and modulus and strength of the bonds. These micro mechanical parameters are often selected to match the macroproperties of a given rock. On account of data availability, the model is generally calibrated by adjusting the strength and the Young's modulus from the uniaxial compression test. Occasionally, the tensile strength from Brazilian test is also incorporated. Even though the void ratio of a given rock is known to significantly affect the mechanical properties of the rock (e.g., Vernik [32]), it has not been explicitly considered in discrete element modeling. In fact, only a narrow range of porosities have been used: around 16% for two-dimensional analyses, and 35% for three-dimensional analyses. This study strives to address whether the current approach of not explicitly incorporating the actual porosity in modeling rocks affects the validity of the results using discrete element modeling.

Specifically, it has been hypothesized that if the macro properties of a rock are captured in a discrete element model, the porosity does not need to be explicitly incorporated. This will be referred to hereafter as an implicit modeling of porosity. Rock cutting has been used as a target problem because it presents a complicated process commonly found in rock construction.

The paper is organized as follows: First, the procedure of generation a rock sample via a bonded particle model is reviewed. This is followed by a brief discussion of how a dense assembly of particles with a small porosity can be created and the procedure is also presented.

Rock cutting is then completed on two samples, one with an actual porosity of 8% and the other with 16% but with parameters such that both have the same uniaxial strength and Young's modulus. This study is limited to two-dimensional problems, and the computer code PFC$^{2D}$ from Itasca (2008) was used in the analysis.

#### *2.3.2.1* ***The procedure of Potyondy and Cundall***

The procedure developed by Potyondy and Cundall (2004) has become a standard for generating bonded particle rock samples. It consists of four main steps as illustrated in Figure 2.29. First, a rectangular domain is enclosed by four frictionless but stiff walls within which particles following a given size distribution are placed. The particles are first given a size that is a fraction of its final size to facilitate their placement, and a small porosity of 8% was initially employed to yield the number of particles used. Second, after their placement, particle diameters are scaled up to create a porosity of 8%. This resulted in significant overlapping of particles. Third, particles are given density and stiffness values but not friction, and the particle overlapping induced contact forces drive the system into an equilibrium state. Fourth, an isotropic stress is applied on the boundary to establish an isotropic stress state within the sample. Floating particles, i.e., particles without sufficient contacts with neighboring particles, are eliminated and bonds are then introduced between contacting particles. This particle insertion procedure is sometimes referred to as a dynamic method due to its consideration of the dynamics of particle motion. There are two types of bonds, the contact bond and the parallel bond. The former has no volume; the latter is modeled as cylindrical beams that have length, area and modulus. This study adopts the parallel bond.

#### *2.3.2.2* ***Creating a rock sample of low porosity***

The preceding procedure generally leads to a sample with porosity of approximately 16%. Particles may be simply deleted from a sample to create a higher porosity sample, but decreasing the porosity is a more challenging task. One possibility is to adopt the Lubachevsky–Stillinger algorithm [33], which is essentially a nonequilibrium molecular dynamics simulation in which the particle size increases with time [34]. But within the framework of discrete elements, Bagi [35] proposed a constructive method in which the particles are placed from a purely geometrical consideration, without simulating the dynamics of particle motion. Schöpfer et al. [36] however, used the dynamic procedure first then inserted particles into existing voids such that in a two-dimensional case an inserted particle would be in perfect contact with three particles. This has been successfully implemented in generated a low porosity of 23% for three-dimensional samples.

Herein, two approaches that were investigated are suggested: First a sample is obtained using the Potyondy and Cundall's procedure. Then, small seed particles are randomly inserted into voids and allowed to grow toward the target porosity. The insertion procedure is repeated until the target porosity is reached. This procedure is illustrated in Figure 2.29 and Figure 2.30.

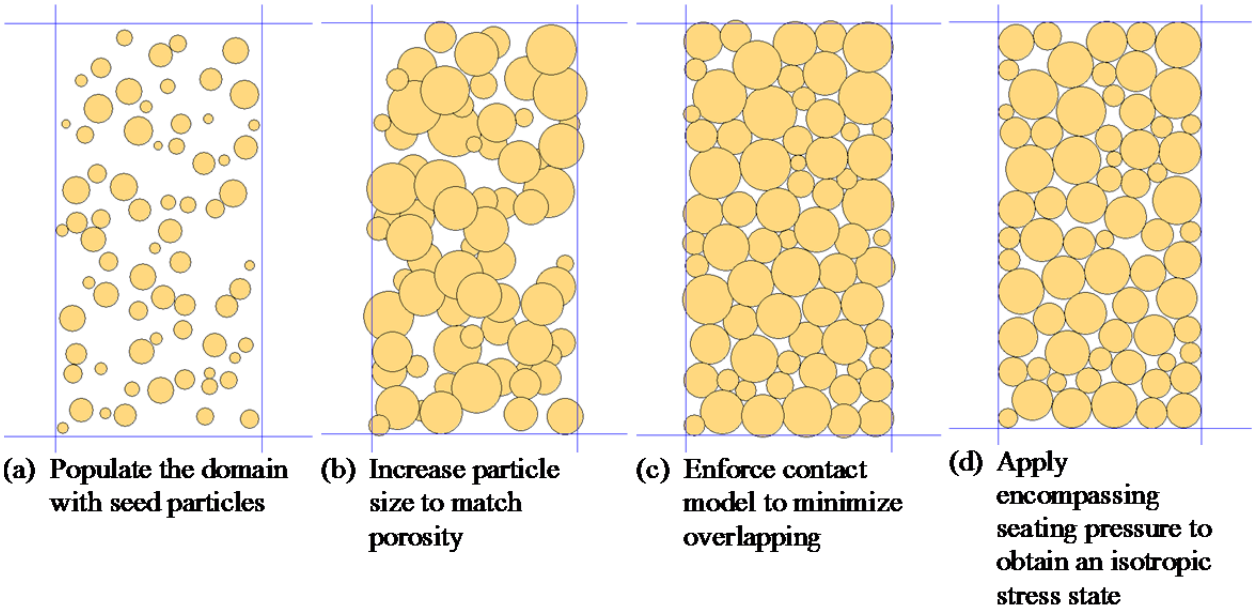


**Figure 2.29** Genesis of a rock sample from bonded particles

Figure 2.29 shows a sample originally created at a porosity of 20% using the Potyondy and Cundall procedure. From that, the sample has been refined to a porosity of 8%, then further to 5%, as shown in Figure 2.30. This approach requires dynamic computation, which tends to be more expensive when more particles need to be inserted. This approach proved to be unsustainable when samples had more than 10,000 particles in its initial state (before the commencement of particle insertion). Thus, an approach similar to the one used by Schöpfer was implemented and it is described below.

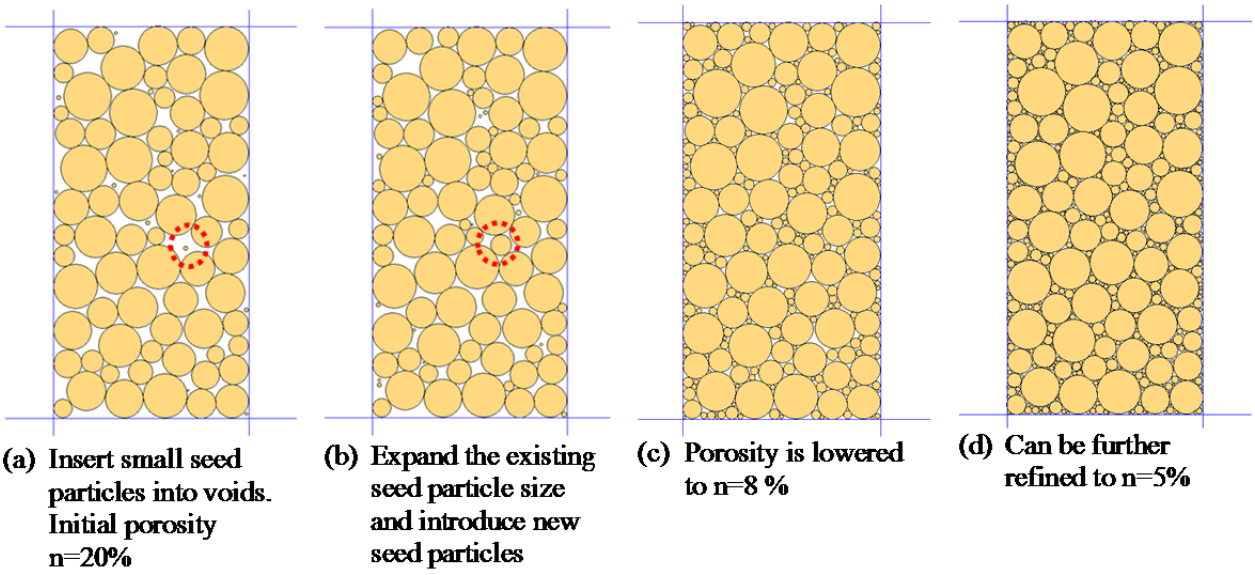


**Figure 2.30** Refine a sample to a small porosity

As in the previous approach, a sample is created by the dynamic procedure developed by Potyondy and Cundall, which is referred to hereafter as *Generation 0*. Then, the voids which can contain particles are identified as follows: First, a closed loop of particles and their contacts are identified as shown in Figure 2.31, using the contacts coordinates. The space where the void is located is shown by the red dashed line. From this encircled shape, the approximate center of the void is located by averaging the contacts abscissas and ordinates, which is shown on the figure as a red dot with a blue cross. From this point, the three closest particles are (depicted by the arrows) identified, and these particles are used for creating another particle that is tangent to these. The Appolonius circle problem is solved in order to find this tangent and the solution is chosen that lies in the spatial void identified. The center of the particle inserted is marked with a red cross. This process is repeated throughout all the voids that exist between particles because voids created between particles and walls are neglected.

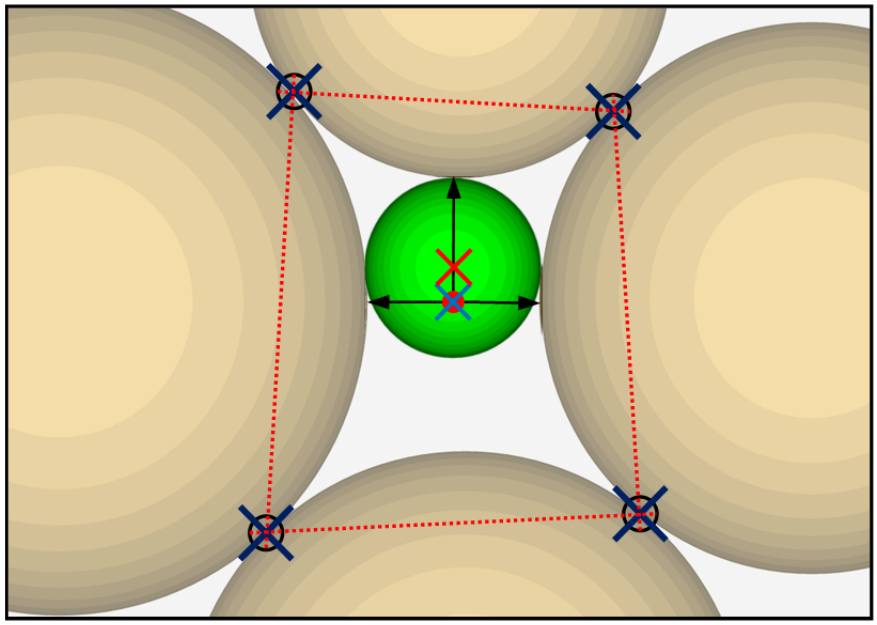

**Figure 2.31** Filling a void via Apollonius' circle

Following the insertion of the first generation of particles in the voids identified from the *Generation 0* sample, a new sample has been created, *Generation 1*. Similarly, several generations of samples can be produced using the predecessor generation as the basis for creating the voids structure, as shown in Figure 2.32. In order to achieve a precise porosity, the generation sample with the closest lower porosity to the target porosity is chosen, and the smallest particles are deleted randomly until the porosity is achieved.

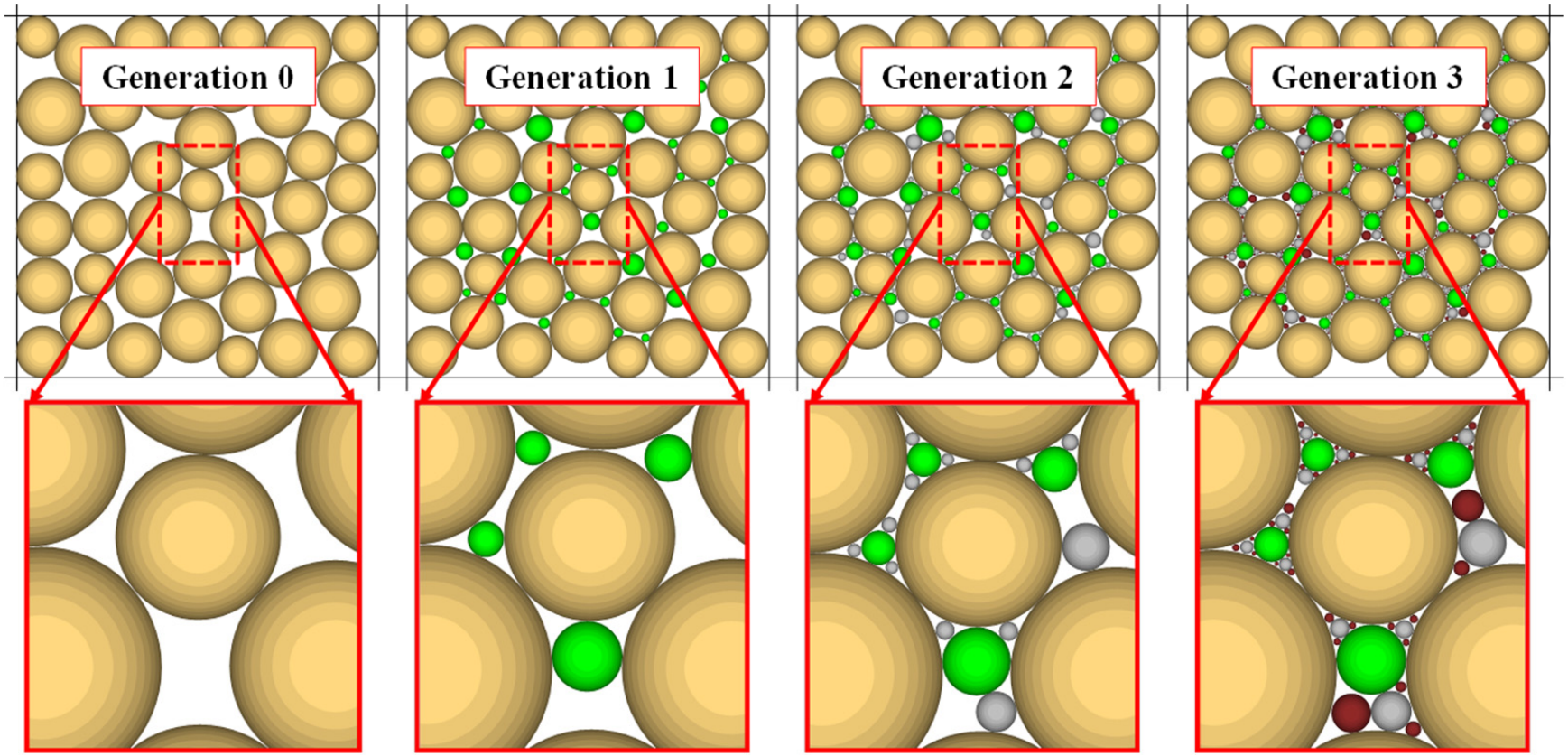


**Figure 2.32** Generation progression when particles are being inserted

### 2.3.3 Discrete Element Simulation of the Rock Scratching Test

The general test procedure and the material property selection for the DEM numerical model are described in this section. The calibration of the material using the unconfined compressive strength test and the aim of choosing different rock-like materials in the numerical model are explained.

#### *2.3.3.1 Geometrical Characteristics of the System*

Determining the appropriate length of a sample is the first issue to be addressed. Richard [17] found that for obtaining stable results the length to be scratched or distance of cutting must be at least ten times the depth of cutting, e.g., for a case of 1.0 *mm* cutting depth, a scratching length of 10 *mm* is required. Because this study focuses only on shallow cuts, it would be expected that cracks, if created, would be shallow as well. This makes it possible to analyze the cutting process considering only a partial size of the sample.

Based on these facts, both height and length can be estimated to obtain a conservative particulate system size that can yield accurate results at a reasonable computational cost. For example, if a rock sample with a height of 30 *mm* and a length of 50 *mm* was used in a laboratory test, the numerical sample dimensions can be greatly reduced, hence, reducing the computational expenses. In this study, it was found that a numerical sample with a height ten times larger than the cutting depth, and length one and a half times longer than the scratching length is sufficient to capture a ductile failure mode without being affected by any boundary condition of the model. A sketch of the proposed model assuming a cutting depth of 1 mm and approximately 17 mm of

scratching length and with respect to laboratory sample dimensions named above is depicted in Figure 2.33.

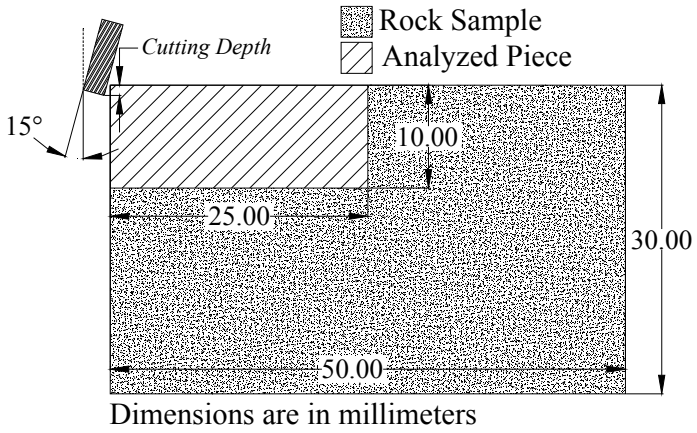


**Figure 2.33** Dimension difference between the numerical model and laboratory sample

From the analysis sample shown in Figure 2.33, and considering the predominant failure mode in the shallow scratching test, a region of particles with identical fineness to the actual size of the grains in a Vosges sandstone is assigned in the top half of the sample. These particles are distributed in the range of diametric sizes from 0.1 *mm* to 0.4 *mm*. To reduce the computational cost, the particle size was increased gradually with depth measured from the bottom of the sample. The top region of the particles is called hereafter the *Cutting Region* as shown in Figure 2.34.

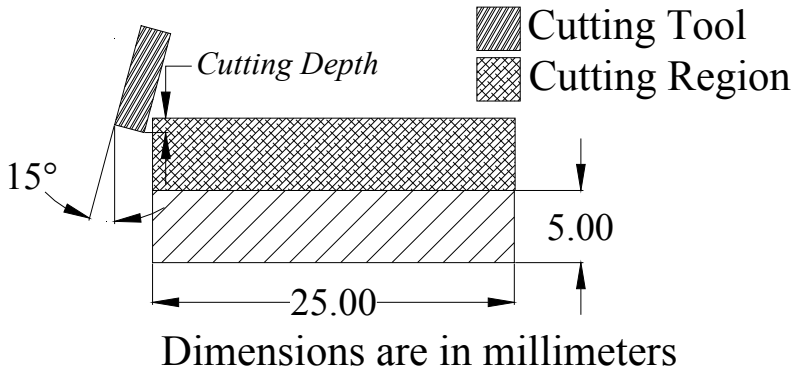


**Figure 2.34** Piece of material analyzed numerically

Lastly, the rake angle of the cutting tool in the model is set to be 15°, the same angle used in experiments in [17]. This angle is depicted in both Figure 2.33 and Figure 2.34.

#### *2.3.3.2 Calibration of the Material*

Due to the availability of scratch test data lacking specific information regarding rock samples [2, 17] general rocks were created for the sake of this analysis. Namely, instead of modeling rocks that are typically found in certain regions, i.e., Berea Sandstone, Carthage Marble, Indiana Limestone, among others, rock-like materials were generated. The engineering classification of intact rocks by Deere and Miller [37] was used as a guide (Refer to Figure 2.35), in which any given rock can be classified by its Uniaxial Compressive Strength (UCS) and the Young's Modulus at 50% of the UCS.

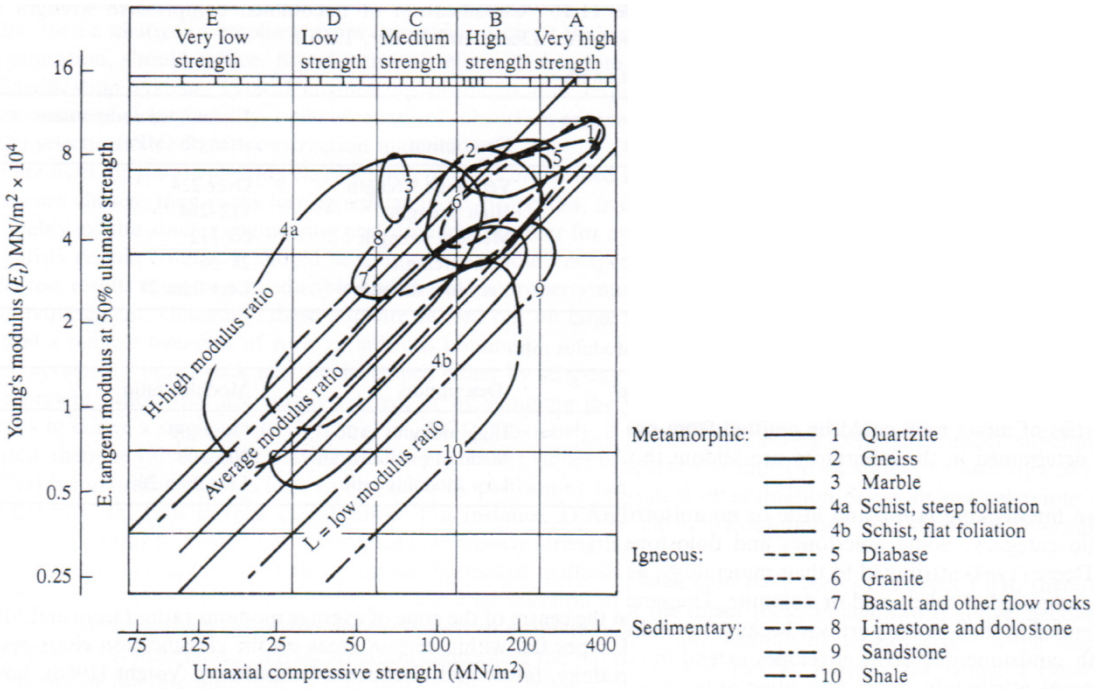


**Figure 2.35** Deere and Miller's engineering classification of rocks taken from Bell [38]

#### *2.3.3.2.1 Laboratory test: Unconfined Compressive Strength Test*

Potyondy and Cundall [3] found that in a PFC2D model, the elastic response of the materials, i.e., Young's Modulus and Poisson Ratio and the unconfined compressive strength, is generally unaffected by the particle size. Thus, the particle size used in modeling the unconfined compressive laboratory tests was selected considering this computation cost. Potyondy and Cundall [3] chose an average diameter of 0.36 *mm* in a rectangular specimen of $63.4 \times 31.7\, mm^2$ for their finest particle system. In this study, the laboratory test sample used an average diameter of 0.52 *mm* in a rectangular sample of$100 \times 50\, mm^2$. The height to width ratio of the sample remains a constant 2 to 1.

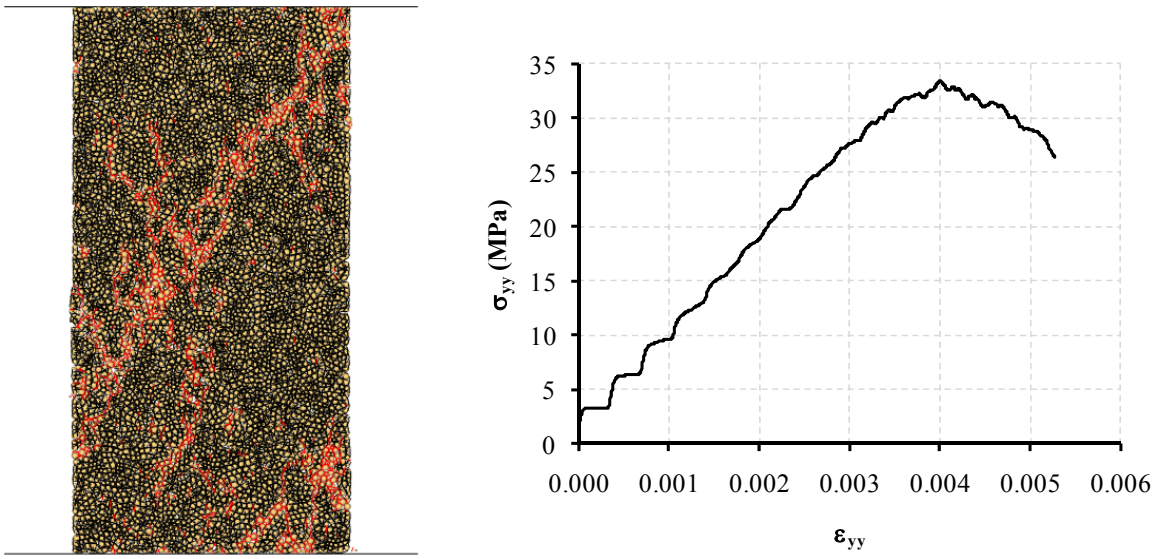


**Figure 2.36** Typical Uniaxial Test in PFC2D, where (a) is the sample at failure and (b) is its respective stress-strain curve

Figure 2.36 shows typical results of a Uniaxial Compressive Test obtained in PFC2D. Broken bonds that failed in tension and shear are denoted by red and magenta lines respectively in Figure 2.36(a) which mimics the failure of surfaces and cracks on a real rock. The parallel bonds that remain intact are represented by parallel black lines while the particles are depicted as light-orange circles in the background. Lastly, the stress-strain curve obtained is plotted in Figure 2.36(b).

#### *2.3.3.2.2 Cases of rocks modeled*

A set of 58 rock-like materials were created, and were classified based on the engineering classification of intact rocks by Deere and Miller [37]. The focus remained on creating a wide spectrum of rock-like materials that would be considered a representative majority of all possibilities of rock types as shown in Figure 2.37.

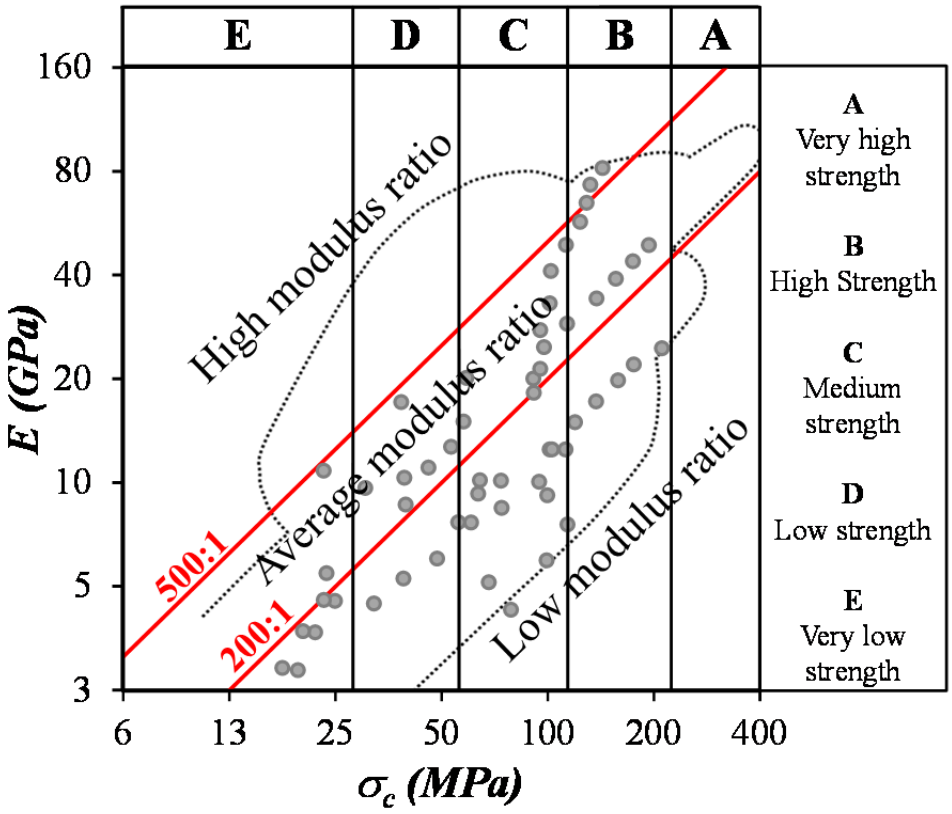


**Figure 2.37** Results of the UCS test obtained in the PFC2D simulation referred to the Deere and Miller classification of rocks [38]

The shaded area represents the union of the rock type boundaries defined in Figure 2.35. The red parallel slopes (500:1 and 200:1) are boundaries that identify the limits between high (above 500:1 slope), average (between 500:1 and 200:1 slopes) and low (below 200:1 slope) modulus ratios. Most of the materials considered occur below the high modulus ratio and cover a wide range from very low to very high unconfined compressive strength. Moreover, it should be noted that the results of the RST are directly related to the UCS, thus, allowing this set of materials to be representative in order to evaluate the ability of simulating RST using the DEM.

#### *2.3.3.3 Boundary and initial conditions in the RST simulation*

The boundary conditions (BCs) in a DEM system can be imposed by walls, particles and gravity. The BCs in walls are given through motion, i.e., translational and rotational velocity; the gravitational field, the acceleration due to gravity; and BCs in the particles by force, moment, or motion applied to the centroid of the particles. Moreover, if the velocity of the particles is not fixed, it can be altered due to the law of motion during contact with another entity, i.e., wall or ball.

The specimen created is bounded by walls on the sides and at the bottom. These walls provided fixed BCs. The cutter is modeled as a segmented wall that moves at a constant speed during cutting. The walls are rigid and can be assigned with a coefficient of friction. Figure 2.38 depicts the simulation before scratching takes place. Two wall BCs are indicated and numbered. The number (1) represents walls at zero velocity while the number (2) is assigned to a segmented wall, mimicking the cutting tool, where the translational velocity is specified but the rotational velocity is zero.

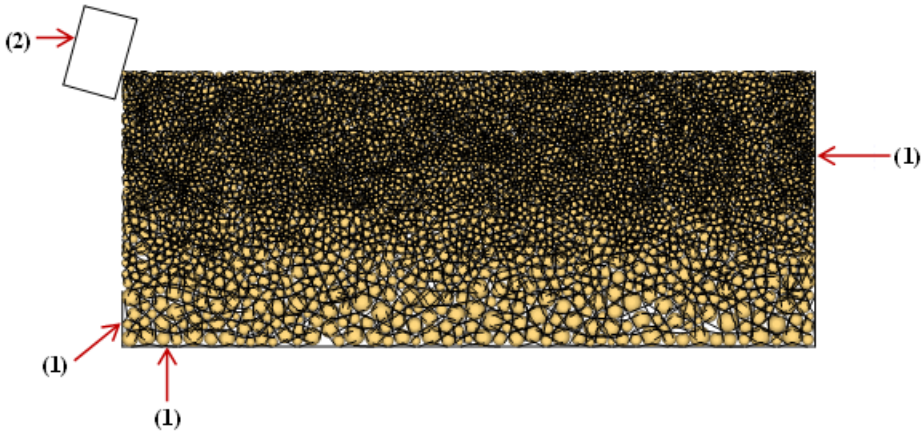


**Figure 2.38** Boundary conditions in the rock scratching model

Walls have normal and shear stiffness values similar to balls. In this study, the stiffness of the walls was assigned a value 10% larger than the stiffness of the balls. The friction coefficient between the walls at zero velocity and the particles is set as 0.1.

### 2.3.4 Discrete Element Simulation of Biaxial Tests Under High Pressure Confinements

PFC possesses an environment designed for performing triaxial tests in the 3D version or biaxial tests in the 2D version that has been widely used for the calibration of rocks. In this environment, the confinement pressure is applied through rigid walls which can be improved as named in the literature review through a *membrane boundary* [13].

The PFC2D has a spanning chains algorithm that creates an effect, similar to the *membrane boundary*, identifying the particles on the outer surfaces as previously seen in the Ledgerwood study [15] (Refer to Figure 2.10). However, some preliminary results of the rock cutting process simulation under high pressure (higher than 100 MPa) showed fictitious responses that are discussed in the last section (**SIMULATION OF THE MECHANICAL BEHAVIOR OF ROCKS UNDER HIGH PRESSURE CONFINEMENT – Foundation for future work**). Due to these results, a different method for applying boundary pressure is proposed in this study, which is discussed in the section **Confinement pressure boundary**. Finally, important aspects of the mechanical behavior of rocks under high confinement pressure are addressed with the purpose of discussing the viability to implement them in the DEM simulation.

### *2.3.4.1 Confinement pressure boundary*

The confinement pressure boundary is created by the use of an algorithm that loops through the particles within a window and identifies the nearest particle to a frame of reference, depicted in the left side of Figure 2.39 as the datum. This process is done for an area of interest, as can be seen in the figure below, where the particles of the edges in dark gray are the membrane boundary of the sample. Forces are applied to these particles in order to generate a pressure field able to reproduce external pressure.

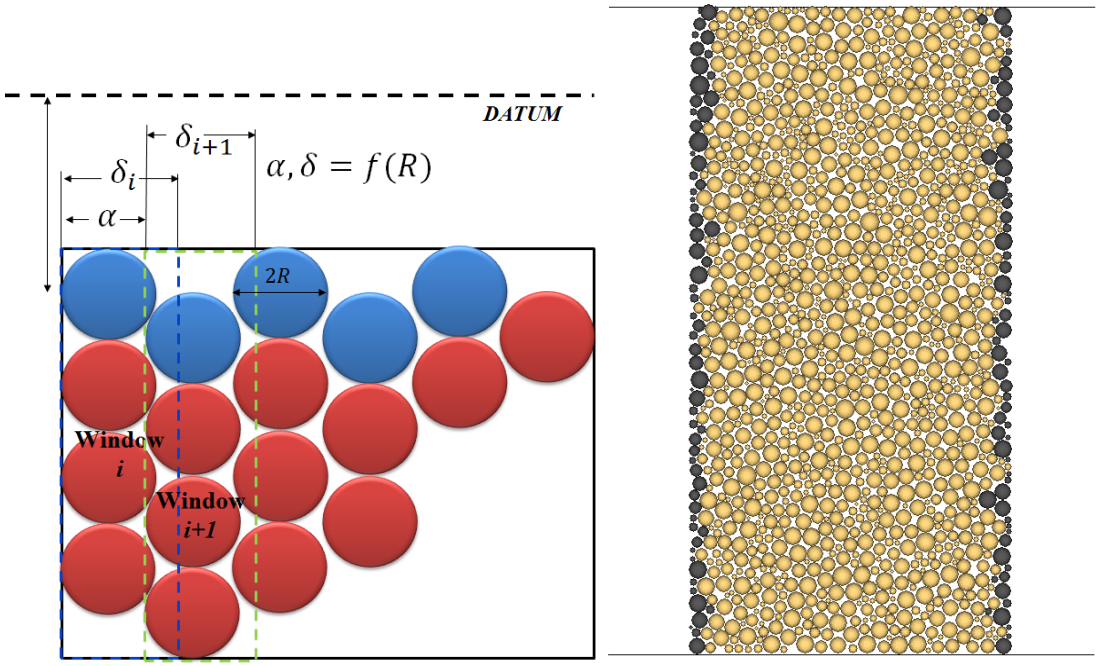


**Figure 2.39** (a) Sketch of the identification of the boundary, and (b) result of the confinement pressure boundary algorithm in a DEM sample for biaxial test

This implementation allows for large deformation on the surfaces exposed to pressure conditions, without the need for spanning chains of particles. Previous results show that this new approach improves the unrealistic failure mode seen in the cutting process.

#### *2.3.4.2 Mechanical behavior of rocks under high pressure confinements*

In this section, the brittle-ductile transition in rocks will be detailed and discussed. The brittle-ductile transition will be the foundation for corroborating the modeling endeavor of this study. This transition is achieved by increasing pressure and/or temperature. Pressure is the factor that is investigated in this study. When rocks are subjected to high pressure, several factors contribute to create a bridge between brittleness and ductility. Here, the factors (or factor) of the ones observed in experiments have the potential to be modeled and implemented in our DEM simulations will be identified. Then, whether the application of these factors dovetailed behavioral similitudes between numerical and experimental results will be evaluated.

A brief description of the confining pressure role in the stress-strain behavior is discussed along with the macroscopic failure and microstructural changes.

##### *2.3.4.2.1 Confinement in the stress-strain behavior*

The evolution of the stress-strain curves with respect to confinement possesses some general aspects listed below, and that can be observed in different cases as depicted in Figure 2.40:

1. When confinement pressure increases, the strain reached at the macroscopic failure, tends to increase until the brittle-ductile transition happens.
2. Stress-strain levels get higher at higher confinement pressures
3. When confinement increases, and at large strains (after macroscopic failure), the stress-strain curves tend to increment the slope passing through strain softening, plasticity and strain-hardening.

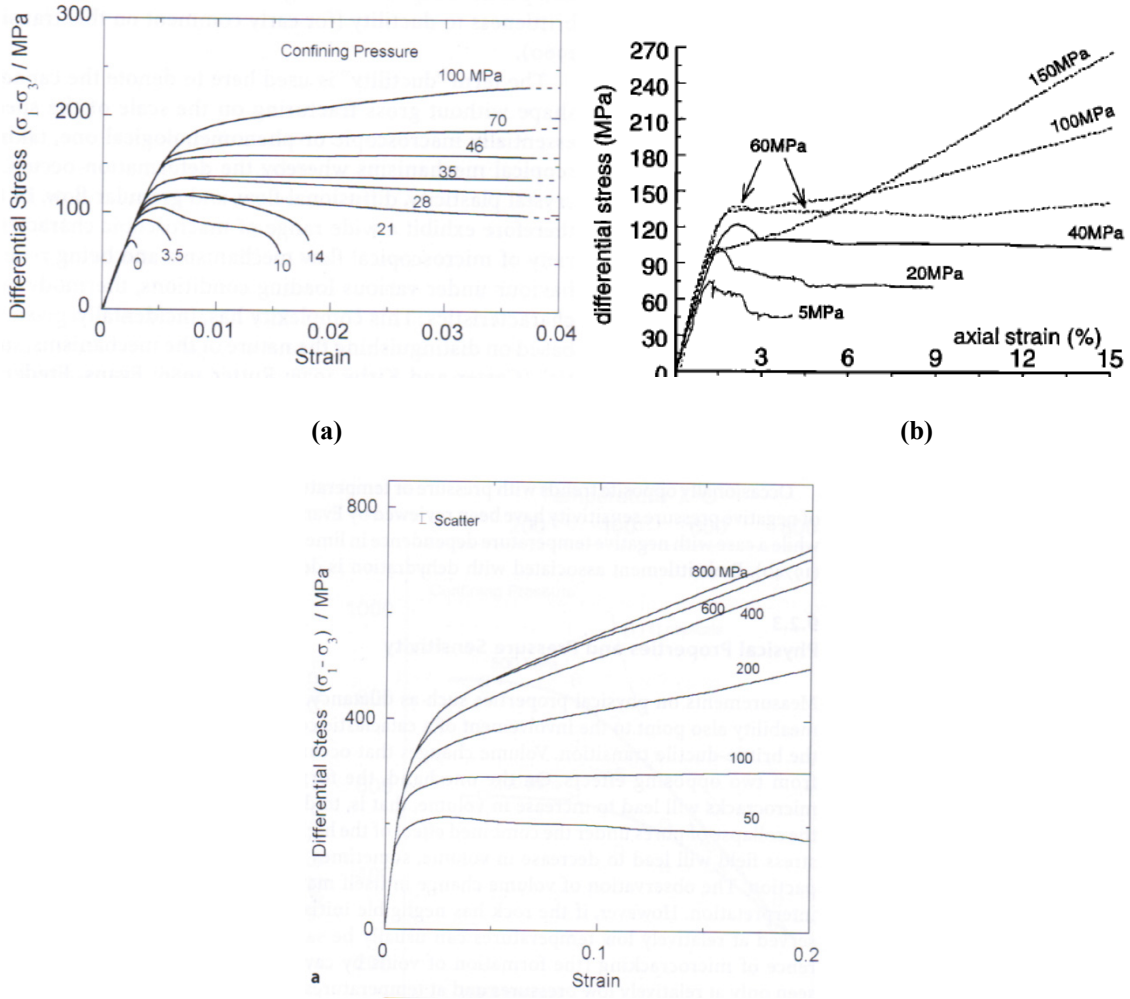


**Figure 2.40** Stress-strain curves of (a) Wombeyan marble [39], (b) Adamswiller sandstone [40], and (c) Carrara Marble [39]

### *2.3.4.2.2 Brittle faulting to Cataclastic flow*

Physically, two deformation processes might lead to ductility in rocks. The first process considers that grain deformation and macroscopic deformation happen in unison. In the second, the macroscopic results are influenced by reconfiguration of grains, resulting in localized relative movement between grains or a group of grains. According to Paterson and Wong [39], the latter

distinguishes between two categories, cataclastic flow and microplastic granular flow. The cataclastic flow is considered in our study because it discards the influence of temperature.

Visual inspection performed by Wong [40], confirms that when rocks failed under the brittle regime, shear localization is found in a detailed shear-band through the sample. While in the ductile regime, damage is manifested by the combination of independent shear bands. Figure 2.41 depicts the evolution of the failure in function of the confinement pressure, where at 3.5 MPa of confinement pressure a single shear failure can be seen, while at 35 MPa and 100 MPa, the combination of several shear bands failure comprise the damage. It is worthwhile to point out, that despite the high pressure the rock was still monolithic after failure. It was criticized that Ledgerwood's simulation results under high pressure developed a failure mode not representative of rocks (Refer to page 30).

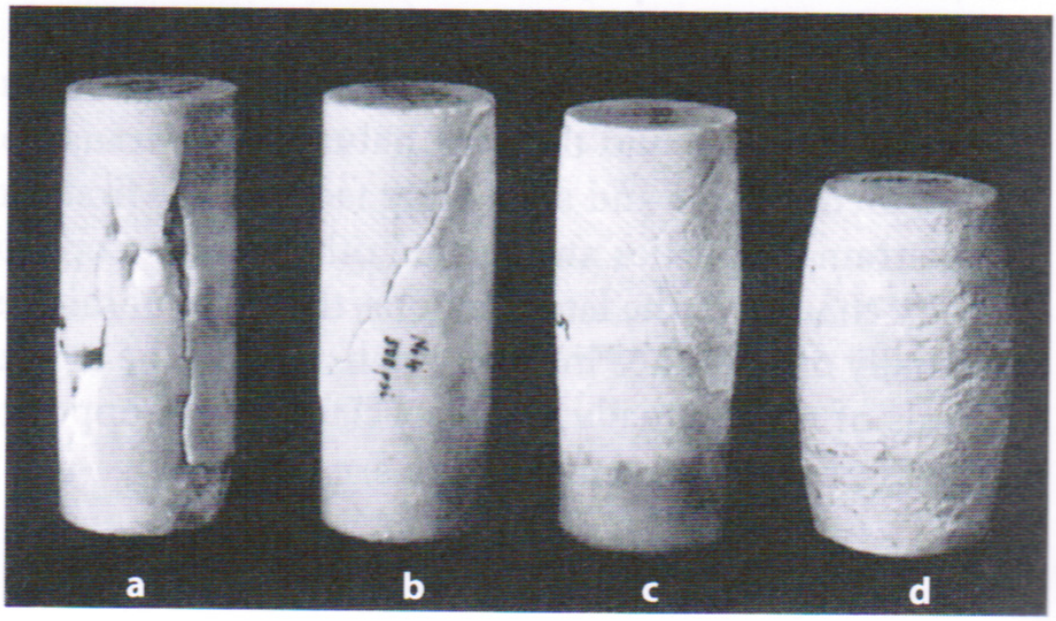


**Figure 2.41** Failure Types in Wombeyan marble at (a) atmospheric pressure, (b) 3.5 MPa, (c) 35 MPa and (d) 100 MPa of confinement pressure [39]

### 2.3.5 Discrete Element Simulation of Rock Cutting Under Pressure

The simulation of the RST test under pressure will be performed following the same procedure that has been widely used by the researchers named in the literature review under the section Discrete Element Modeling of RST under Pressure. The simulation environment is similar to the one described in the Discrete Element Simulation of the Rock Scratching Test, with respect to the geometry and boundary conditions, but with the difference that a new boundary condition will be applied on the top of the rock specimen using the Confinement pressure boundary proposed in this study. A drawing taken from a technical memorandum of Itasca consulting group is depicted in the figure below.

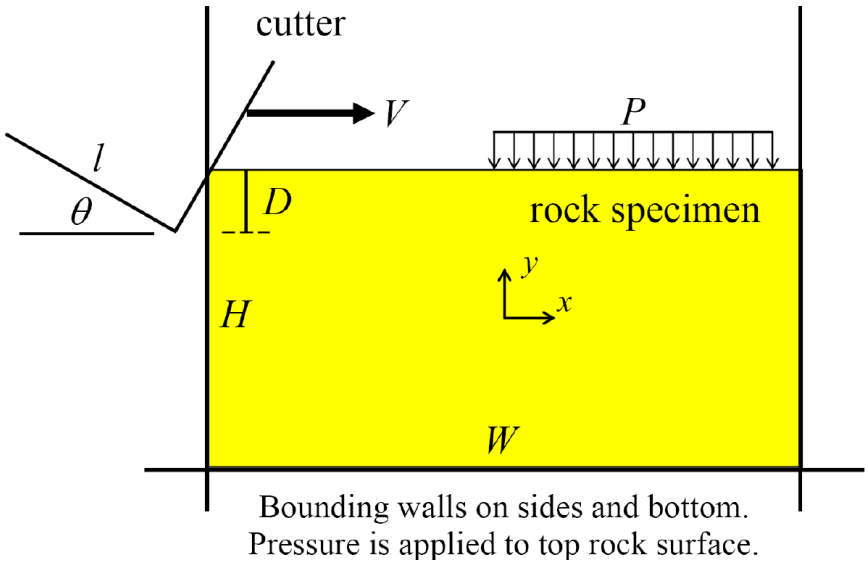


**Figure 2.42** Sketch of the simulation environment for rock cutting under pressure (http://itascacg.com/pdf/pfc/ex_rockcut2d.pdf)

# 3.0 DEVELOPMENT OF THE ROCK SCRATCHING TEST MODEL

Summarized herein are the most important results found throughout the research on the objectives outlined in the previous section. The cutting specific energy of the rock-like materials created is related to their respective unconfined compressive strength, and these results are compared with the ones obtained via the RST [2, 17]. The mechanical behavior of the rocks under pressure is discussed, and the different factors that have been taken into account in order to improve the failure and deformation mechanisms. Finally, the improvement of the rock cutting process under pressure thanks to the implementation of the *Confinement pressure boundary* is shown.

## 3.1 SIMULATION OF RST USING TWO-DIMENSIONAL DEM

### 3.1.1 Validation Data Base Population

In order to develop the model for the RST, a database of rock like material must first be populated and validated with expected mechanical behavior. These macro-properties have been acquired with the procedure described in the Sensitivity Analysis. The simulated material behavior is then validated against standard mechanical behavior based on an engineering classification of rock materials.

The chosen engineering classification system for validating this rock behavior was the system devised by Deere and Miller [37]. This classification system requires the Young's modulus and the unconfined compressive strength which is then plotted as shown in Figure 2.35 of the previous section. It is important to note from this figure that the mechanical behaviors calculated from uniaxial compression strength are encompassed by the contours based on rock types numbered 1 through 10 in shown in Figure 2.35. This boundary was used in the validation of the numerical rock material database to ensure all samples fell within expectation.

Therefore, the constructed boundary of expected rock behavior is shown along with the results obtained from the numerical rock like materials in Figure 2.37. It is clear that all values fall within the expected range of typical rock behavior based on known rock types. Additionally, it can be seen that an even distribution of numerical rock like material has been created. The database includes rock materials ranging from low to high Young's modulus and unconfined compressive strength values.

### 3.1.2 Establishing Model Inference Space

Before the RST model development, critical parameters were first identified which could potentially affect both the magnitude of response and failure type. These variables will be studied independently and special attention will be paid to behavior at extreme values to establish a reasonable inference space for these model parameters. This will both ensure the production of reasonable and realistic results as well as to identify parameter sensitivity. Parameters were identified based on the literature review and laboratory testing.

#### *3.1.2.1 Cutting depth influence on horizontal forces on RST*

First, the effect of the cutting depth on the magnitude of the horizontal forces of the RST was investigated. It has been suggested that a critical cutting depth exists which serves as a boundary for the failure mode experienced by the rock. This critical cutting depth is highly dependent on the characteristics of the specific rock used, such as type and strength. Generally, a stronger rock exhibits a smaller critical cutting depth and likewise a weaker rock exhibits a larger critical cutting depth.

The results from this analysis are shown in Figure 3.1 below and testing was performed on a low-strength rock (refer to Deere and Miller). Literature indicated and testing conferred that As the critical cutting depth appeared to be approximately 1.2 mm. It can be seen in Figure 3.1 that the relationship between cutting force and cutting depth is approximately linear and fits the trendline shown well until the critical cutting depth.

Additionally, the failure mode experienced by the rock changed for cutting depths exceeding the critical cutting depth. The observed failure mode for cutting depths less than 1.2 mm was a ductile failure whereas the observed failure mode for cutting depths greater than 1.2 mm was a brittle failure.

While the data remains approximately linear following the critical cutting depth, the data points are much more scattered following this critical cutting depth. However, this behavior is unrepresentative of expected rock behavior as failure cannot linearly increase indefinitely with cutting depth [1]. The cutting force should approach a limiting value which is not observed in this plot. Therefore, this model is limited to the analyses of shallow cutting in the RST.

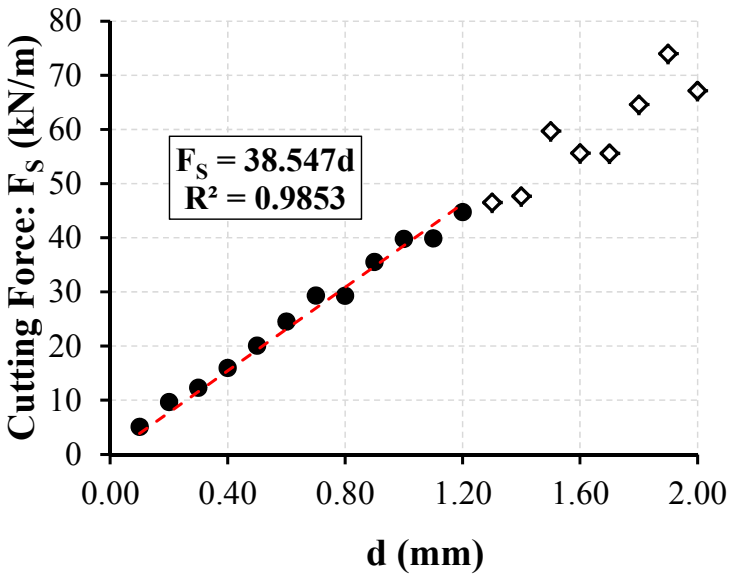


**Figure 3.1** Analysis of critical cutting depth

### *3.1.2.2 Effects of rock elastic modulus*

The average cutting forces for shallow RSTs have been shown to correlate well with the unconfined compressive strength of rocks [1, 2, 18, 41]. In order to assess the reliability of our DEM model, we adopted a suite of rock samples and investigated if a similar correlation could be obtained through simulation. To produce a suite of samples, we took a route of using a basic structure like that from our typical Vosges sandstone, but changing the modulus and strength parameters so that they spanned over a wide range of $E/\sigma_c$ values. To get a sense of possible variation in the cutting forces, we began by looking into the impact of having $\sigma_c$ fixed, while changing $E$ values. Figure 3.2 shows shallow cut results on four different samples created with approximately the same $\sigma_c$ but different Young's Modulus. The resulting average force varied from 45*kN/m* to 65*kN/m* with $E/\sigma_c$ varying between 95 – 770. As a base line for comparison, we also created a suite of samples using exactly the same parameters and found that the different particle arrangement alone induced a smaller variation. With a total of 10 random samples, the

mean cutting forces were 37.97*kN/m* with a standard deviation of 4.44*kN/m*. Combining these two factors together we concluded that at a given $\sigma_c$, simulation results could have a range of average force variation of about 20 to 30% from the mean if only the bond strength and stiffness were changed.

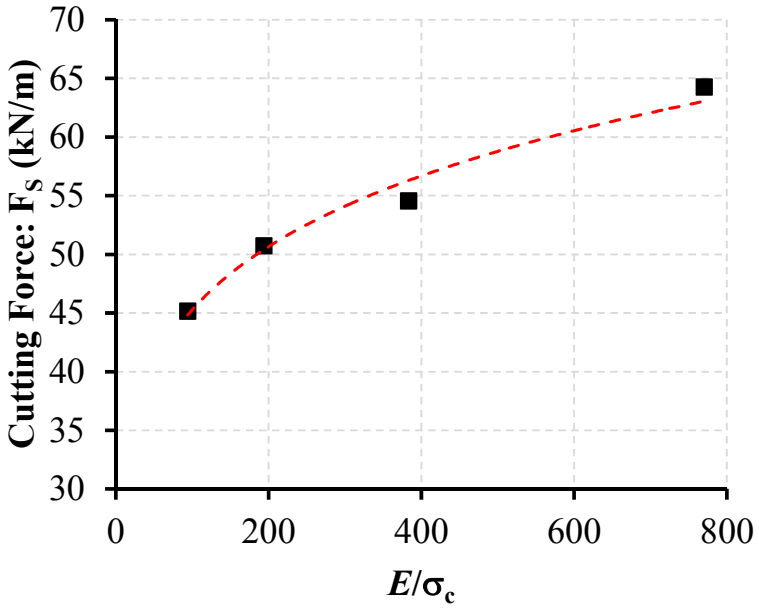


**Figure 3.2** Shallow cut results with varying Young's Modulus values

### *3.1.2.3 Selection of damping and cutting speed*

In modeling a RST, damping coefficients of the rock and the advancing speed of a cutter were two intertwined factors that played significant roles on both the resulting cutting forces and the fragmentation patterns obtained. To match laboratory RST results, it was critical to reconcile these two factors in a systematic manner.

Impact of damping coefficients of rocks in cutting was first studied by Lei et al. [30]. We have confirmed that, under a given cutter speed, a low damping coefficient in the rock would lead to a failure characterized by substantial chip formation. As the chips were pushed away, the

cutter would often lose contact with the rock sample. The intermittent contact between the cutter and the rock sample yielded a discontinuous cutting force history and a low average cutting force. On the other hand, a cutter tended to have a better contact with the rock sample when the damping factor was high, and failure would be seen mostly through grinding.

In a similar manner, the advancing speed of a cutter would affect the cutting force and the fragmentation process. It turned out, that changing the cutting speed would have the same effect as changing the material damping. This point is highlighted by a comparison depicted in Figure 3.3. Figure 3.3 (a) shows a low cutting speed of 0.25 m/s induced chipped failure in a shallow cut for a rock with a damping of 0.7, and a similar chip was observed for a low damping of 0.05 under a higher cutting speed of 2 m/s. The actual cutter speed in the laboratory RST was low at 4 mm/sec, and it was not feasible to adopt that speed in the simulation. Moreover, we have found using a local adaptive damping, $\alpha$, of 0.7 provided good results in simulating uniaxial compression tests; and to be consistent throughout the modeling process, this level of damping was kept. Thus we tuned the cutting speed such that both cutting forces and fragmentation process were well modeled. In this respect, the study has selected a cutting speed of 2 m/s. This set of the cutting parameters were employed in extensive simulation of shallow cuts satisfactorily.

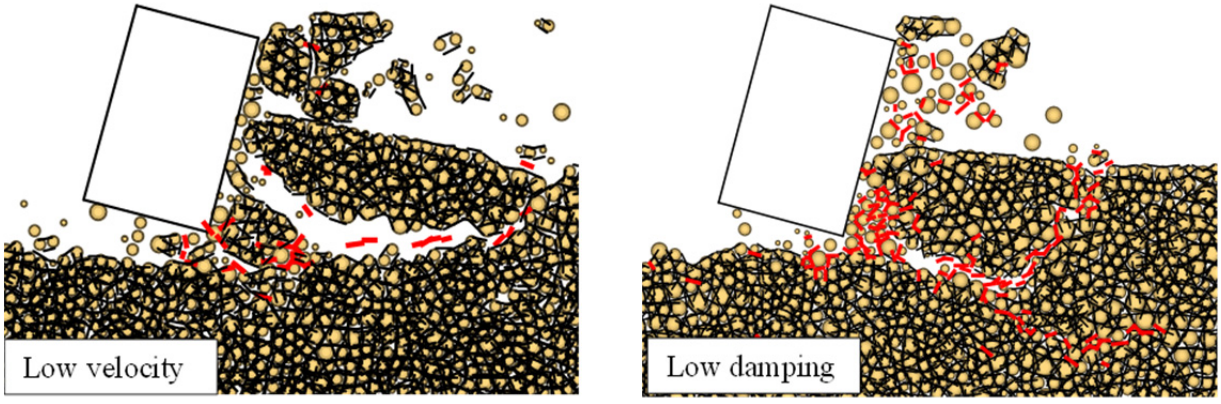


**(a)**

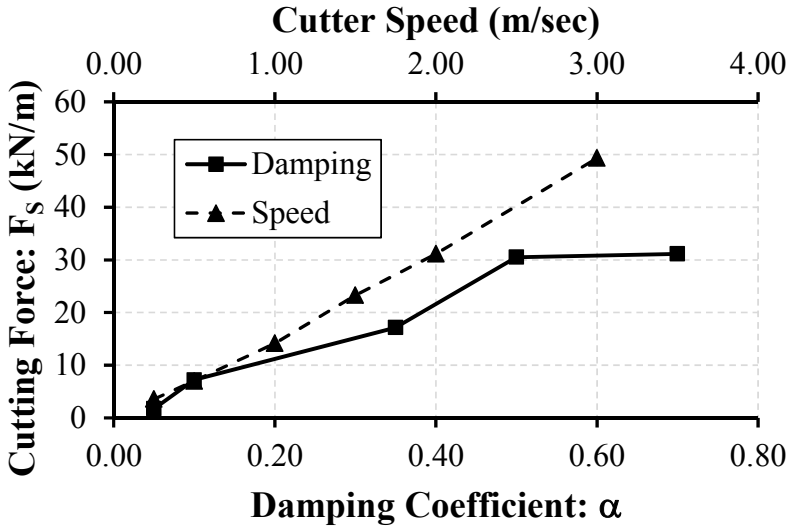


**(b)**

**Figure 3.3** Influence of cutting speed and damping coefficient on a) failure mode and on b) the average cutting forces.

Finally, the damping coefficient was also analyzed for deep cutting, and it was found that the failure mode was more representative for low damping coefficients, and the cutting forces tended to be more shaped as a sawtooth wave, however, it was considered that having different

damping coefficients for the shallow and deep cutting cases was not a consistent with the benchmark that we wanted to deliver in this study.

### 3.1.3 Significance of Particle Crushing for RST Calibration

The implementation of particle crushing consisted of two steps. Step one was to determine the crushing strength of a particle. Step two was to decide on the post crushing configuration. A major deviatoric stress failure criterion was employed. The post crushing configuration proposed by [42] was adopted. With that, a crushed particle was replaced by a number of smaller particles arranged in a particular manner without bonds.

The major deviatoric stress on a particle was computed from the average stress tensor. Within a particle it was defined in terms of the peripheral forces and their position vector as follows,

$$\overline{\sigma}_{ij} = \frac{1}{V_p} \sum_{c=1}^{n} r_i^c F_j^c \tag{1}$$

where, $V_p$ is the volume of a particle, $F$ is one of the $n$ contact forces acting on the particle, $r$ is a position vector measured from the center of the particle to the contact force point.

Data to this point has shown good correlation with the rock scratching test results for low strength rocks, defined as rocks with an unconfined compression strength less than $75MPa$ as shown in Figure 3.4 below which shows good correlation between the model and laboratory data for low strength rocks.

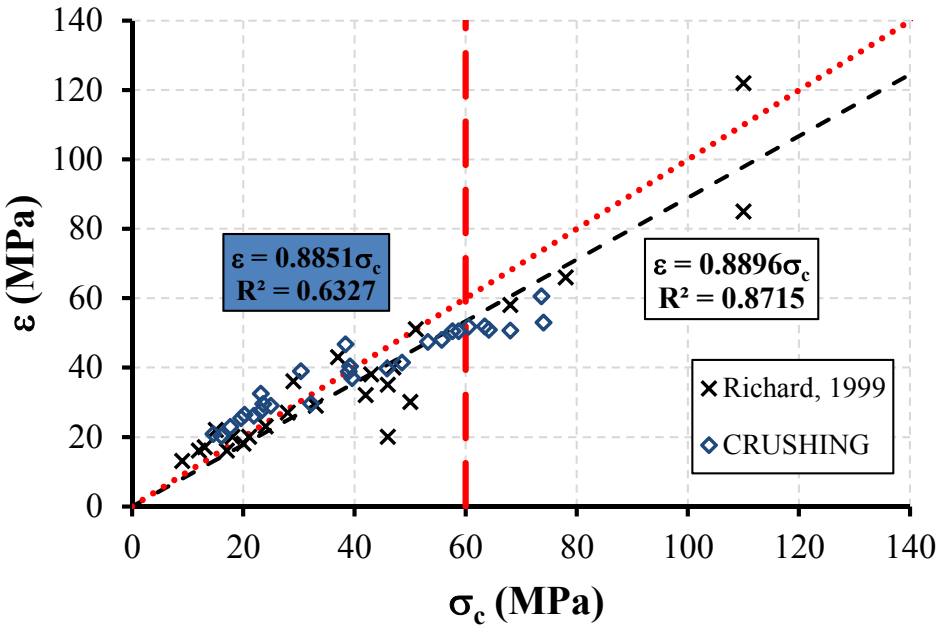


**Figure 3.4** Initial results considering particle crushing

To further investigate the discrepancy of the rock scratching test data for rocks with an unconfined compression strength greater than 60*MPa*, the significance of particle crushing effects was considered. Previous work (Mendoza 2010) has indicated that considering particle crushing in the rock scratching test improves the fit of the data as shown in Figure 3.5 below. This improvement can be attributed to additional contact provided between the crushed particles and the cutter which ultimately creates a smoother and more representative force history plot as well as slightly increasing the cutting specific energy.

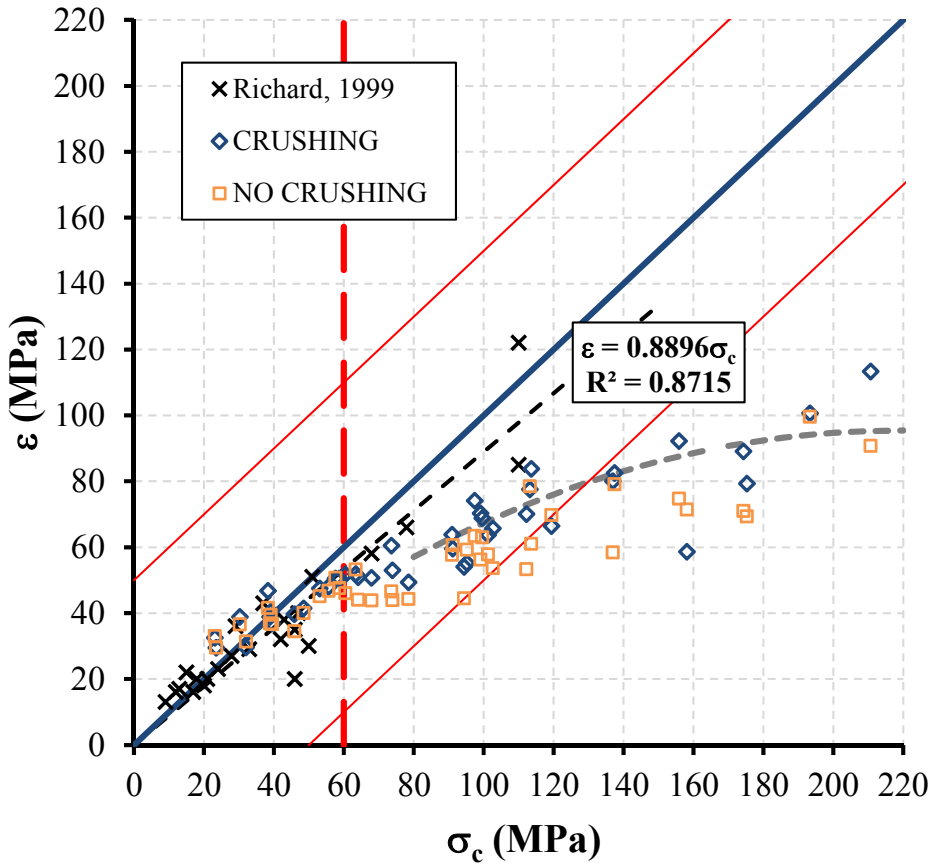


**Figure 3.5** Effect of considering particle crushing

These initial improvements seen from including particle crushing effects primarily improved the model for low strength rocks. Shown in Figure 3.5 above, the data incorporating particle crushing for low strength rocks (occurring below the dotted line shown corresponding to an unconfined compression strength under 80*MPa*) produced a better fit. These improvements did not reflect for moderate to high strength rocks and the fit of the data did not improve when considering particle crushing effects as can be seen from Figure 3.5.

To improve the prediction for moderate to high strength rocks, the influence of the cutter was then considered. The contact between the rock and the cutter can be described by a friction coefficient. Richard (1999) has shown that a friction coefficient of 0.69 corresponds to a worn

PDC cutter. Investigating the effect of this relatively extreme value should reveal any possible effects from the cutter friction coefficient. Figure 3.6 below shows the results without considering the effects of particle crushing comparing friction coefficients of 0.25, representing the standard model value, and 0.69, representing a worn PDC cutter.

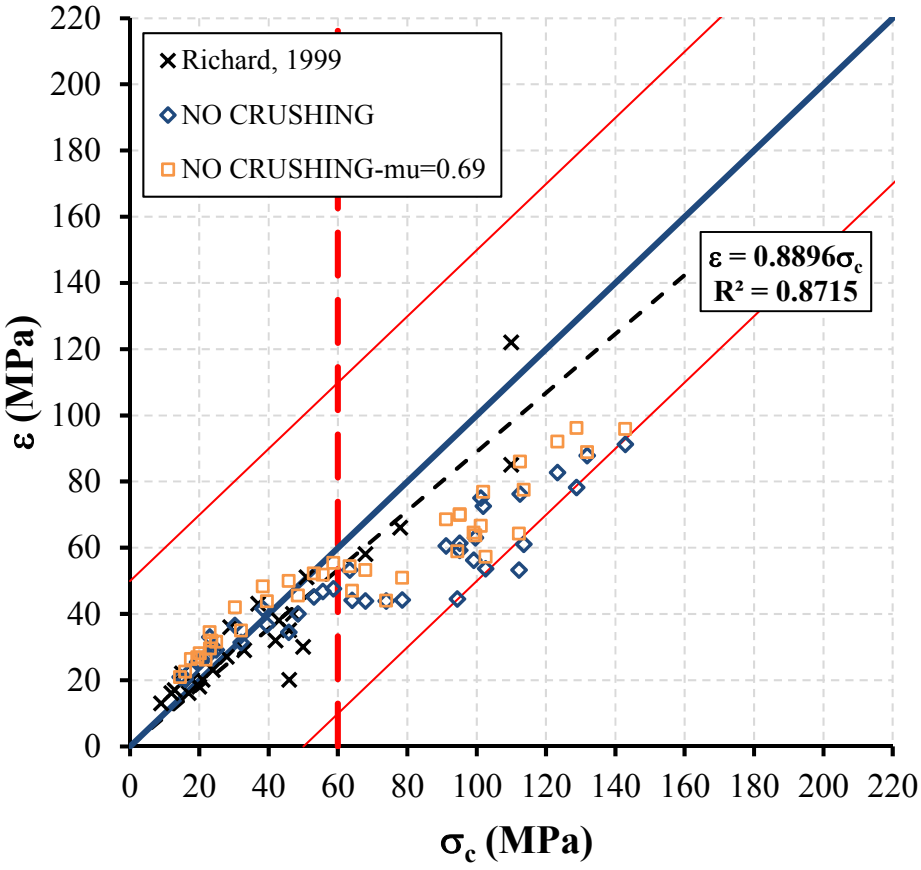


**Figure 3.6** Effect of cutter friction without considering particle crushing

This Figure shows that varying the coefficient of friction of the rock cutter did not produce a better fit for moderate to high strength rock data. The same friction coefficients were then considered with rock crushing and the results are plotted in Figure 3.7 below.

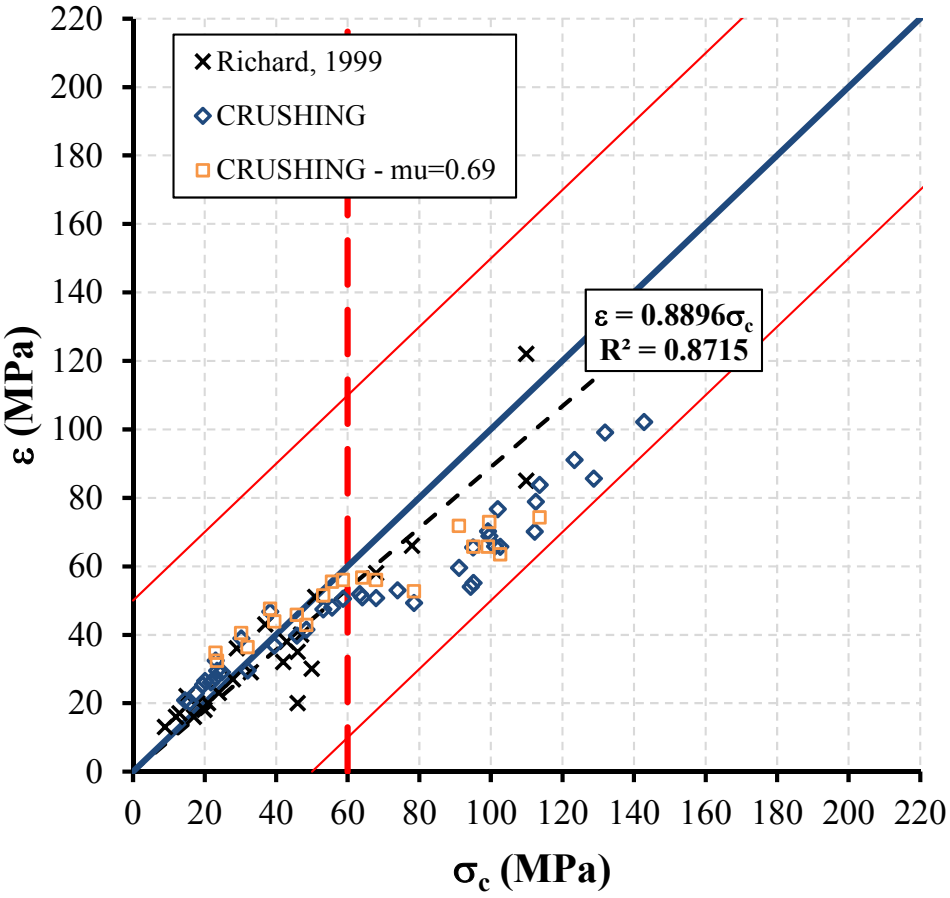


**Figure 3.7** Effect of cutter friction considering particle crushing

The effect of varying the friction coefficient when particle crushing effects are considered also did not produce a better fit and the effect of the friction coefficient appears to be negligible.

The next factor considered which could affect the results for moderate to high strength rocks was the cutting depth. As previously discussed, the failure mode of the rock is dictated by the cutting depth where a shallow cutting depth produced ductile failures and a deeper cutting depth produced brittle failures. Therefore, varying the cutting depth would reflect a change in failure mode which could possibly result in a better fit for moderate to high strength rocks. In this case, a shallower cutting depth of half the control cutting depth was considered and the results are shown in Figure 3.8 below.

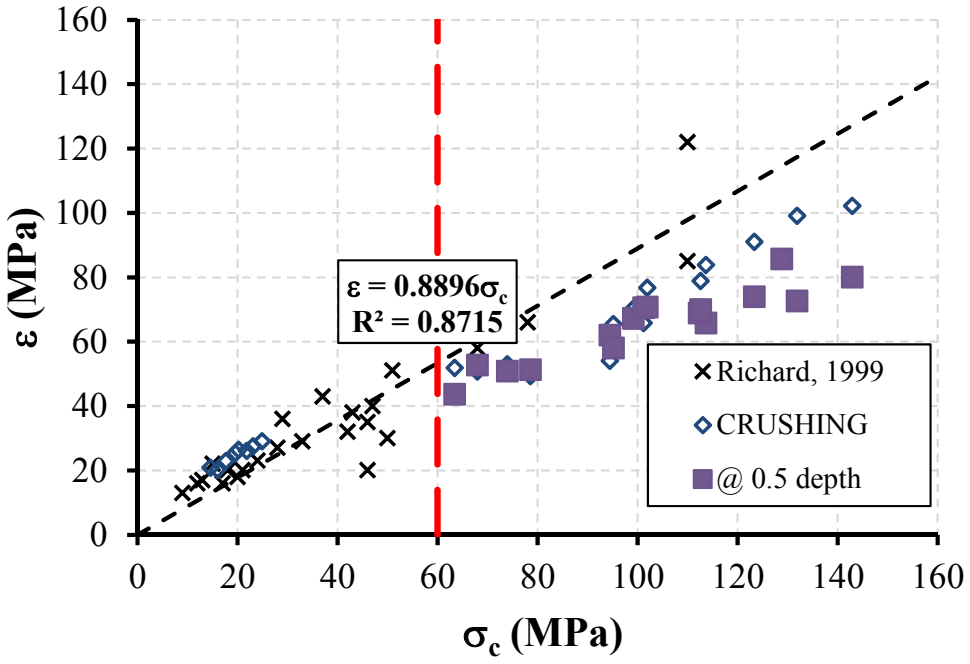


**Figure 3.8** Effect of decreasing cutting depth

It can be seen from Figure 3.8 that despite decreasing the cutting depth to avoid a brittle failure mode, the cutting specific energy did not match the theoretical results.

The next factor considered which was thought to potentially affect the results from moderate and high strength rocks was the modulus ratio, defined as the elastic modulus divided by the unconfined compression strength. It was speculated that a pattern could exist between the low modulus values, defined as values below 150, and high modulus values, above 150. Particle crushing was considered in both cases. The results from this analysis are given in Figure 3.9 below.

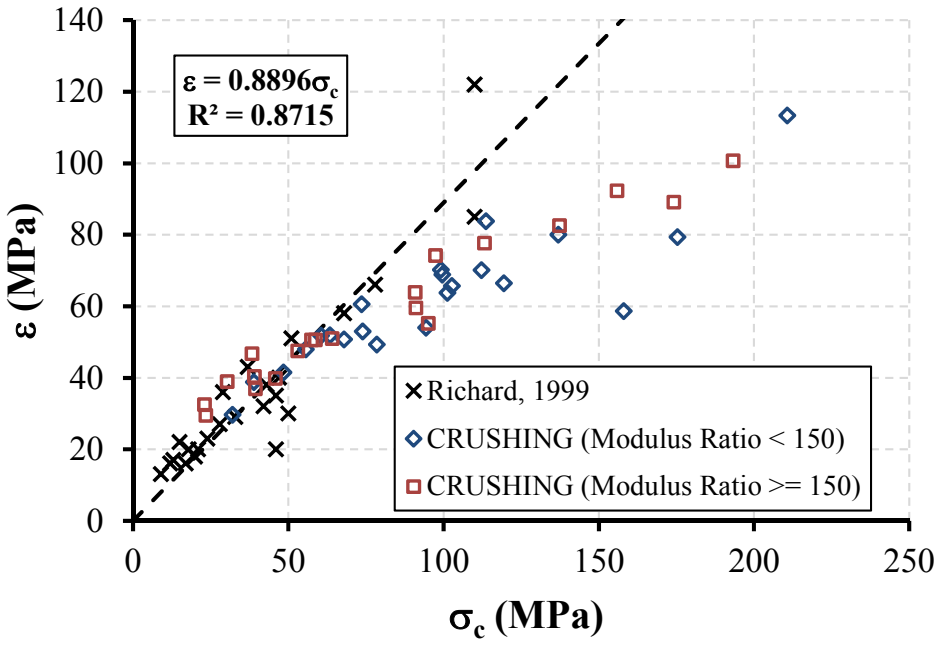


**Figure 3.9** Effect of varying modulus ratio considering particle crushing

It can be seen from this figure that no trends were present between the low and high modulus values. Additionally, the effect on the results also appears to be negligible and there is still very clear scatter present for moderate to high strength rocks. However, to better define and investigate this scatter, specific modulus values were chosen, rather than simply a broad division between low and high modulus ratio values. Eight specific modulus ratio values between 127 and 469 were investigated and the results are plotted in Figure 3.10 shown below.

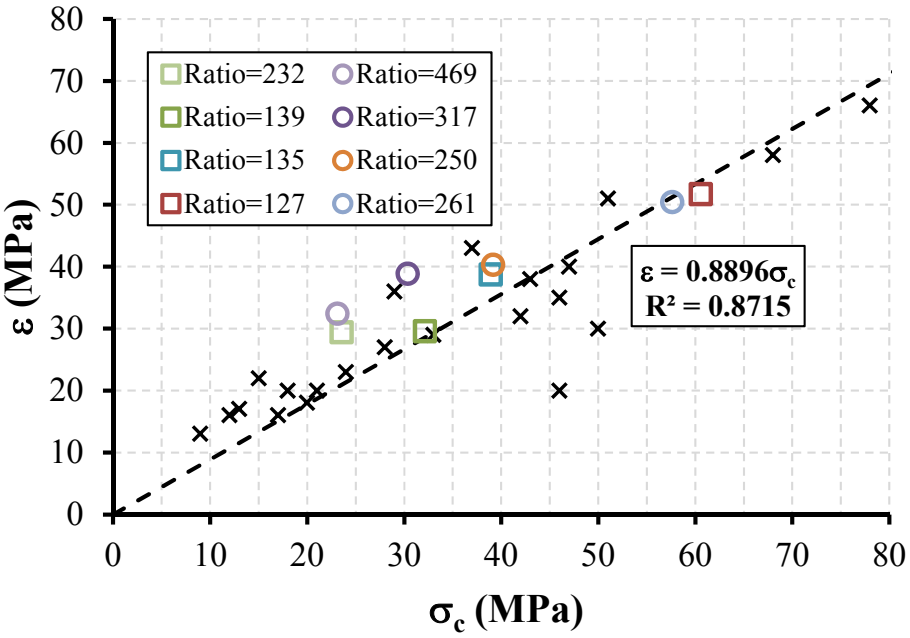


**Figure 3.10** Analysis of specific modulus ratio values

Two conclusions can be drawn from this plot. First, varying the modulus ratio does not appear to reflect in any trends present for the cutting specific energy versus unconfined compression strength plot. Secondly, varying the modulus ratio did not appear to have any effect on the results to better fit the laboratory data to the data produced by the model. Therefore, more variables must be considered in order to better fit the data for moderate to high strength rocks.

To continue investigating this discrepancy in the agreement of the data, the significance of particle crushing was revisited, but was approached considering different factors. Rocks are assumed to be composed of various particles (grains) and are generally characterized by the most abundant particle type present in the rock. For example, sandstones are characterized by being comprised primarily of silica. Crushing strength is assumed to be representative of rocks taken as a whole; however, considering that particles vary for each rock type then by extension, crushing

strength should vary for each rock type as well. This would produce further complications to the incorporation of particle crushing in the model.

Particle crushing strength is also known to be particle size dependent with high variability. The Weibull distribution has been used to successfully model this variability ([43]; [44] & [45]). However, laboratory tests revealed diverging results for the investigated range of particle sizes. Figure 3.11 below summarizes relevant published data. It can be seen from this plot that different rock types, in this figure, silica or quartz, experience different characteristic crushing strengths.

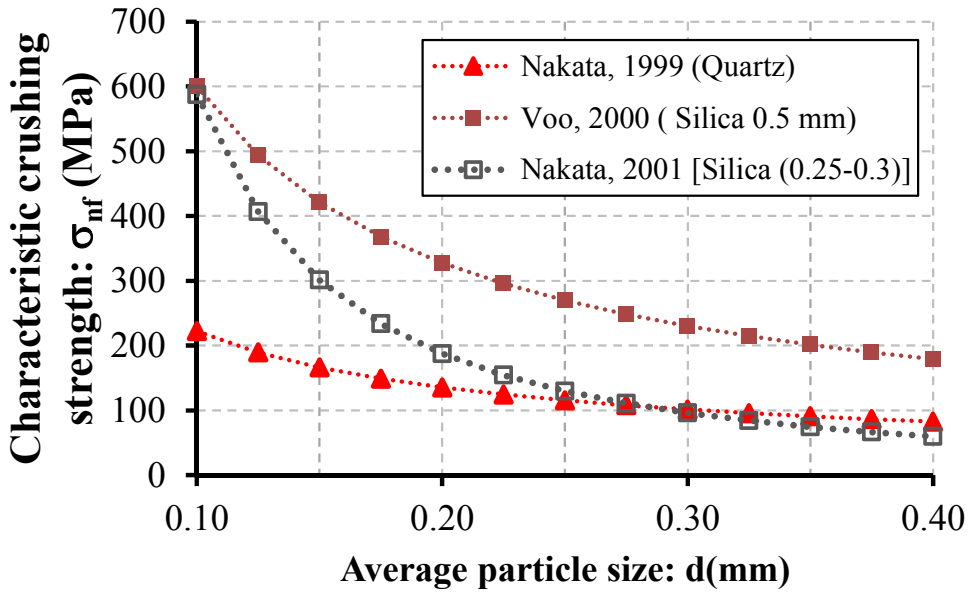


**Figure 3.11** The size-dependent crushing strength characteristics of a single particle

Because it was the intent of this investigation to examine the effects of incorporating particle crushing, particles which more easily experienced crushing, defined as those with a low characteristic crushing strength would be preferred for computational efficiency. Therefore, the

results obtained for quartz by [43] will be incorporated in this model because as shown in Figure 3.11, these quartz particles have the lowest characteristic crushing strength values.

Incorporating particle crushing was found to improve the agreement of the model and experimental data. This improvement in agreement can be wholly attributed to the change in failure mode. Figure 3.12 below shows results from the model obtained both considering and ignoring particle crushing effects. Figure 3.12 (a) highlights data point A, which does not incorporate particle crushing. The same data point but incorporating particle crushing is shown in Figure 3.12 (b) and is labeled as point B. It can be seen that incorporating particle crushing has increased the calculated strain and the point has raised above the trend line. This observed change indicates that the force transmission pattern has shifted when particle crushing effects are incorporated. This caused the failure mode to shift from a brittle failure when particle crushing effects are ignored to a ductile failure when particle crushing effects are incorporated and as seen in the figure, the average force, and consequently the specific energy, increased.

Points C and D shown in Figure 3.12 (b) below describe samples with identical parameters but point C has exhibited a ductile failure while point D has exhibited a brittle failure. The difference in failure mode experienced can be attributed to the built-in randomness in sample generation.

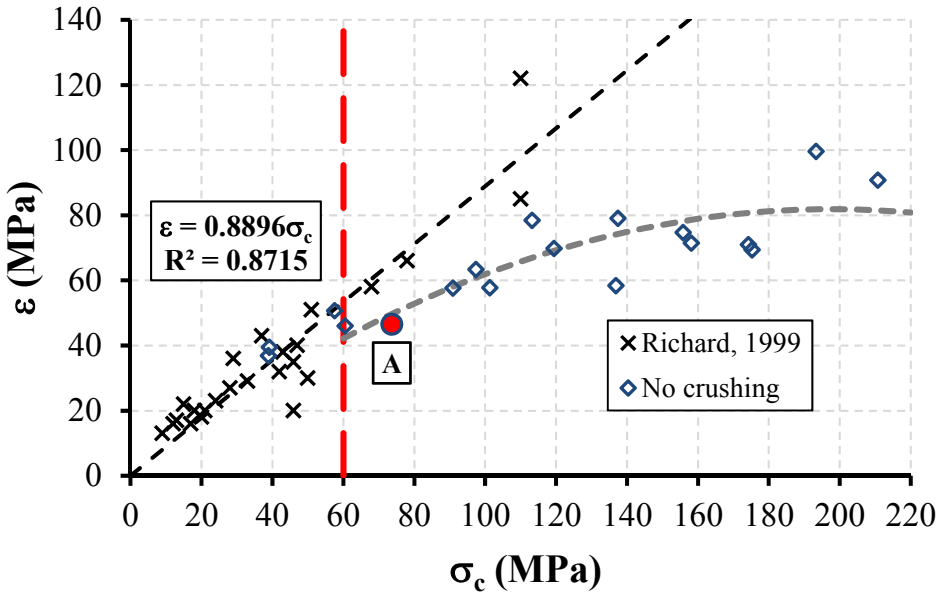


**(a)**

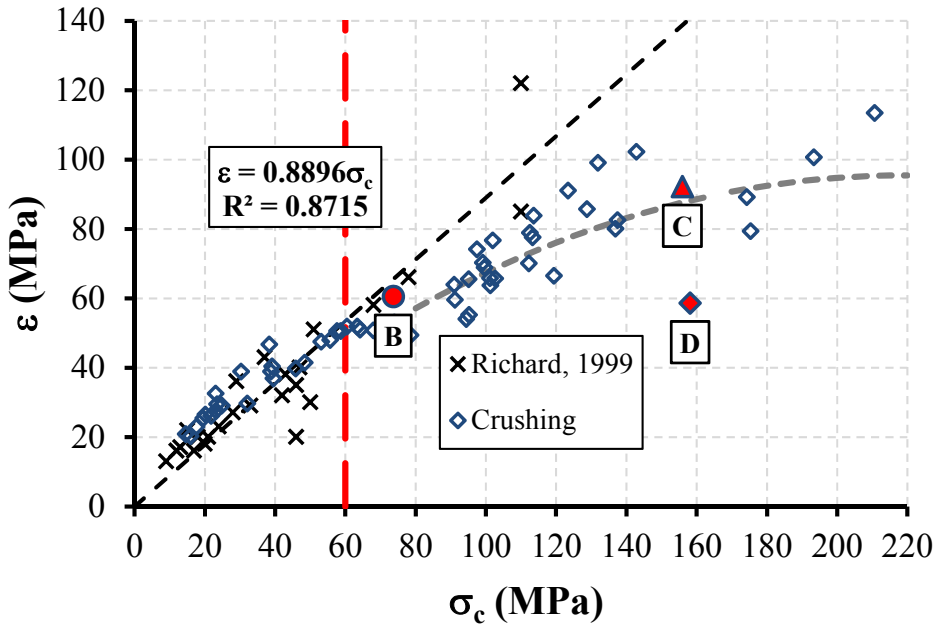


**(b)**

**Figure 3.12** Analysis of calibration methods without considering particle crushing (a) and with considering particle crushing (b)

Therefore, improvements were obtained in agreement between laboratory data and the RST model results for cutting history forces, failure mode, and failure patterns when particle crushing was incorporated. However, the behavior of high strength rocks, or rocks with an unconfined compression strength higher than 60$MPa$, is still not represented by this model. The laboratory data still clearly diverges from the model predictions. It can be speculated that particle crushing strength should vary with the unconfined compression strength of the rock samples. Therefore, a higher particle crushing strength for high strength rocks would be more representative and should be adopted for better agreement. However, due to the limited data available considering particle crushing strength, this is not currently a viable solution and a simpler, more efficient representation is presented.

To additionally support the conclusions drawn about the effect of incorporating particle crushing, specific simulation results were analyzed by considering failure. Several snapshots were taken at different points of the cutting process for low and moderate strength rocks showing the velocity vectors of the entities (particles and walls). Figure 3.13 below shows the results when particle crushing is considered. Velocity vectors in front of the cutter suggest a smooth flow of particles, defined as when the cutting is completed with a shearing motion that does not create any kind of chipping. The results obtained without considering particle crushing were identical. The lack of dependence on the presence of particle crushing can be attributed to the fact that in low strength samples, greater strength is required to crush the particles rather than causing the particles to debond.

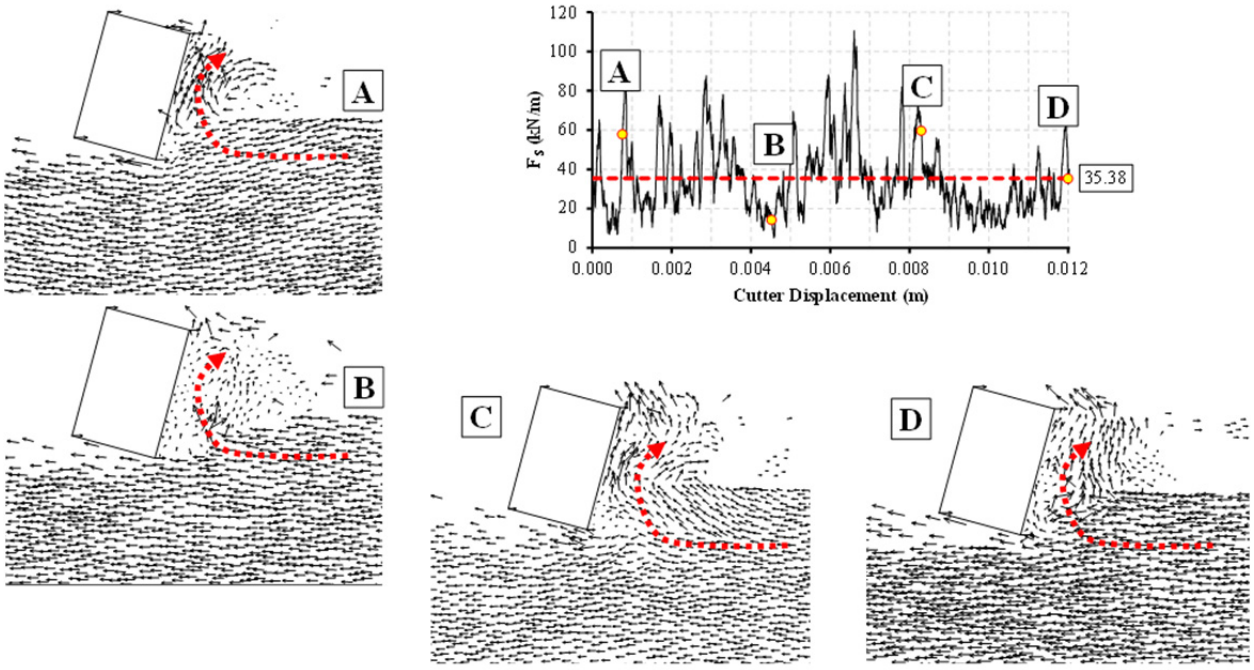


**Figure 3.13** Interaction of cutter with low strength rock – crushing and no crushing

For moderate strength rocks, however, there is a difference in results depending on whether particle crushing is considered. The flow of particles in front of the cutter for crushing is similar to that observed for the low strength rock. However, when particle crushing is not included, chipping develops in the front of the cutter (where chips are designated in the figure with a red dashed line) and interrupts the flow of the particles. This interruption lowers the cutting forces due to decreasing contact area in front of the cutter and records a less smooth force time history as a result. This provides further evidence that considering particle crushing decreases chipping.

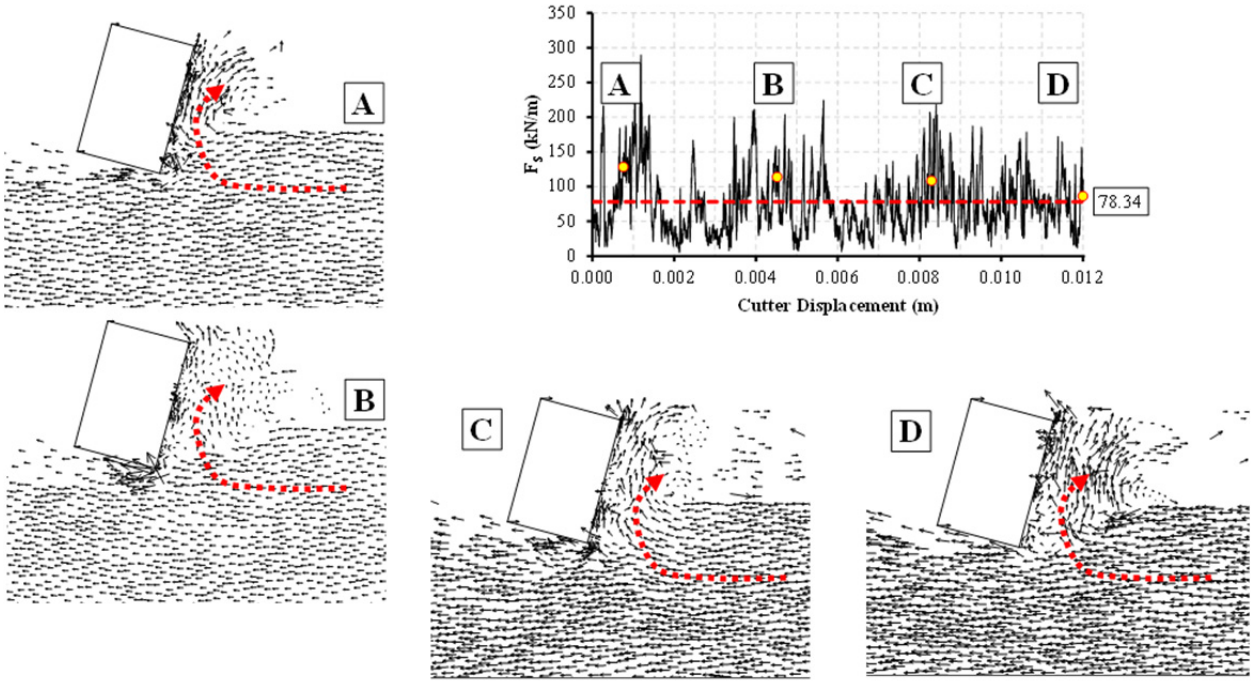


**(a)**

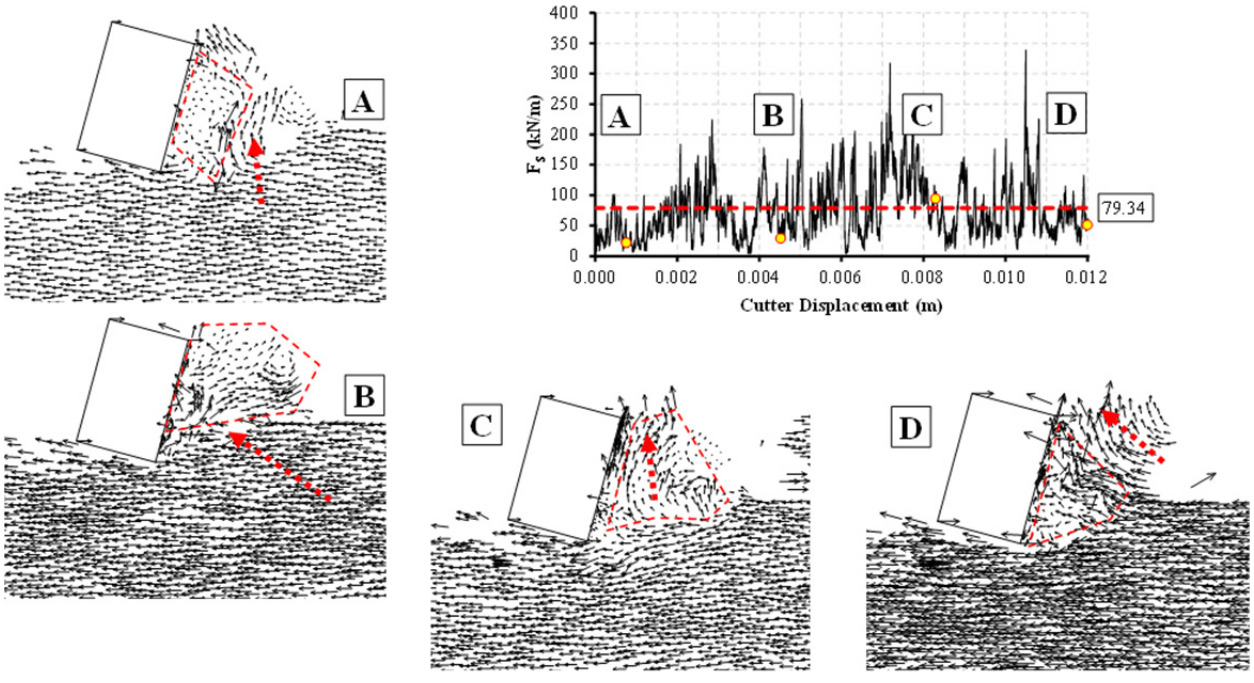


**(b)**

**Figure 3.14** Interaction of cutter with moderate strength rock – (a) crushing and (b) no crushing

This chipping effect that occurs for moderate strength rocks is magnified for a deeper cutting depth. Figure 3.15 below depicts the interaction between chips in front of the cutter and the flow of the particles. This can be seen easily from the particles because this is a deep cutting case; however, for a shallow cutting case, where brittleness is introduced in the cutting process (recall from Figure 3.14 above), the velocity vectors are required to clarify and verify whether the rock is undergoing a brittle or ductile failure.

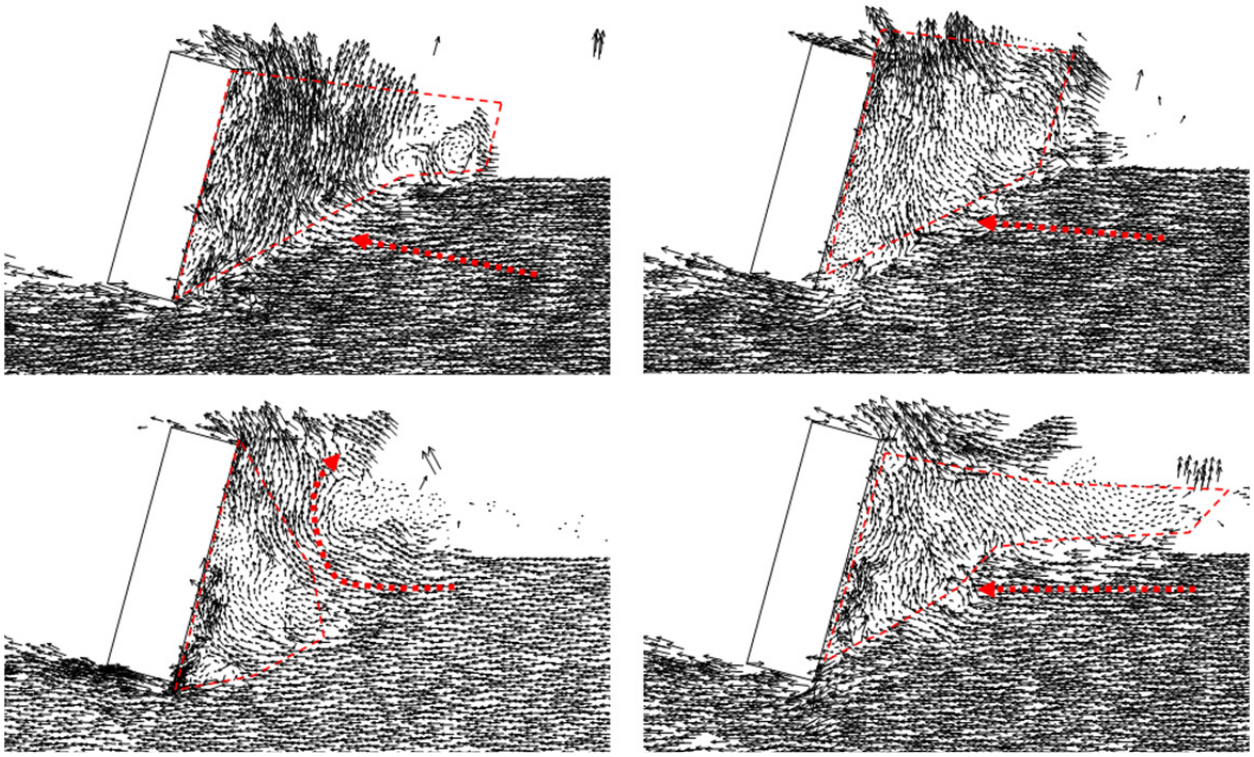

**Figure 3.15** Deep cut, no crushing

### 3.1.4 Evidence for Model Calibration Based on Particle Size

Despite the disagreement with data from higher strength rocks, the improvements of the model as a result of particle crushing effects provided an indication that considering other particle-level variables could provide a better fit between the model and laboratory test results for higher strength rocks. Rather than consider particle crushing, the effect of the particle size will now be investigated, specifically its effect on the unconfined compressive strength.

The unconfined compressive strength can be described as a function of the characteristic (average) particle size as shown in Figure 3.16 below. Therefore, rocks with smaller particles tend to have a higher compressive strength while rocks with a lower compressive strength tend to be comprised of larger particles. The effect of the particle size on compressive strength is more pronounced for rocks with a strength higher than $60MPa$. Interestingly, this correlates approximately to the point at which the current RST model no longer agrees well with laboratory data because of the poor correlation between the cutting specific energy and the unconfined compressive strength.

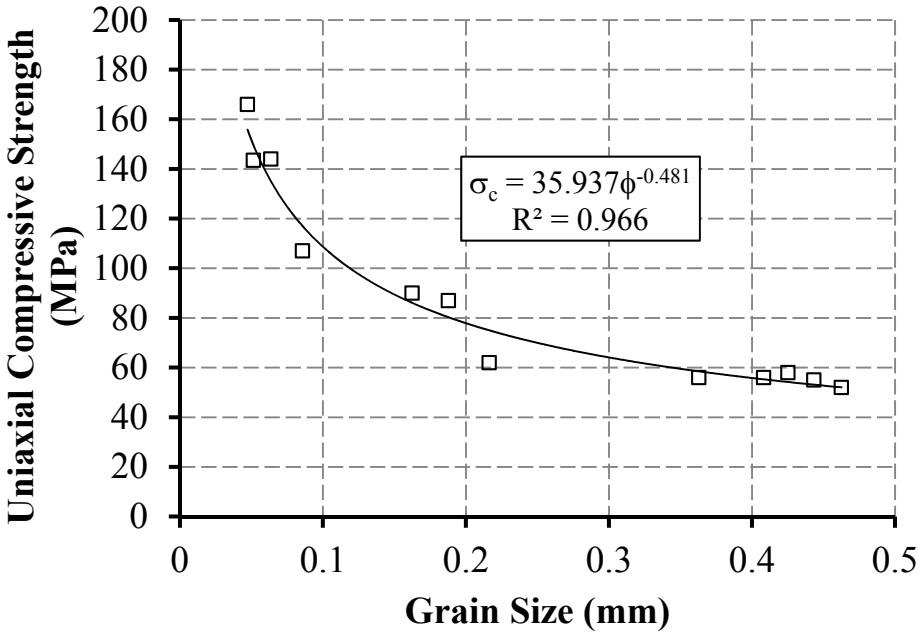


**Figure 3.16** UCS defined from particle grain size, Wong et al 1996

### 3.1.5 DEM Simulation Sensitivity to Particle Size

Since particle size has now been identified as a potential means of calibrating the current DEM model, the ability of the DEM model to replicate the mechanical response exhibited in the work by [46] (1996) must first be checked. Conducting a suite of unconfined compression strength tests, which would quantify the influence of particle size on uniaxial strength, could verify this replication. However, previous work by [3] has shown that the resolution of the DEM model subjected to unconfined compression strength testing does not significantly affect the final macroproperties.

The effect of incorporating particle size effects in the model still required investigation despite the previously observed limited effects of absolute particle size. Considering that

absolute particle size was not considered significant, relative particle size could be further investigated. In order to consider the importance of relative particle size, the particle size distribution range was identified as a possibly impactful variable. This approximate range of particle size distributions was described by the ratio of maximum particle radius to minimum particle radius, referred to as $R_{rat}$.

To analyze this effect of varying this particle size distribution ratio, three unconfined compression strength tests were performed for each material considered. To accomplish this, three samples were created using the same microproperties and $R_{rat}$; however, the particle arrangement differed for the three samples to incorporate randomization for each material. Additionally, different $R_{rat}$ models still contained the same number of particles. The results from varying $R_{rat}$ were normalized and shown in Figure 3.17 below. The effect of varying the $R_{rat}$ on different mechanical properties of the rock are shown for three different properties: Young's modulus ratio, Poissons ratio, and unconfined compression strength.

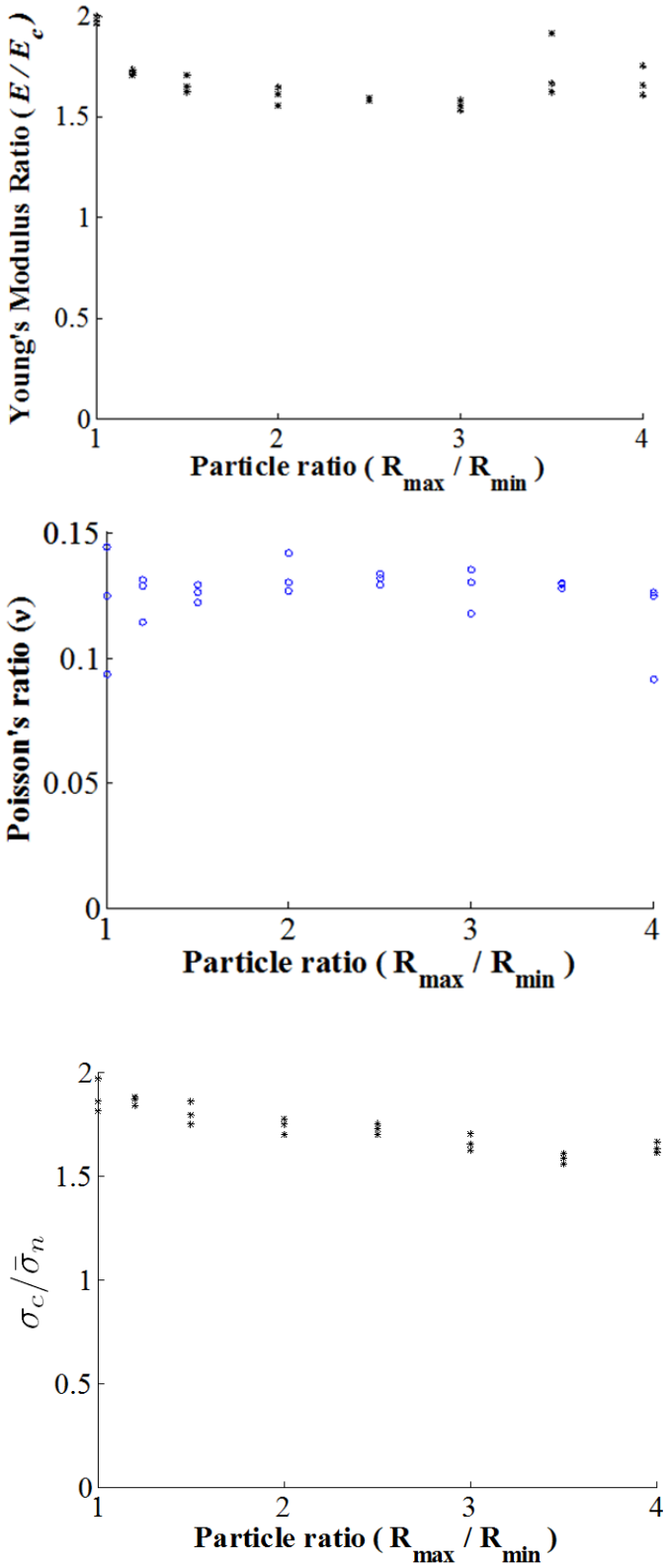


**Figure 3.17** Sensitivity of particle size to (top to bottom): Young's modulus, Poisson's ratio, and UCS

It can be seen from these plots that there is not a significant relationship between the particle size and the macroproperties (such as Young's modulus, Poisson's ratio, and unconfined compressive strength). These results align with those obtained by Potyondy and Cundall and further show that not only the resolution, but the range between maximum and minimum radii, have no influence on the unconfined compressive strength results.

Therefore, there was a lack of a discernible relationship between the particle size, the resolution of the model, and the macroproperties. The independence of these three factors to each other can be attributed to the sufficient contact between the platens and discrete particles. In general, if the contact area between the particles and the wall is able to consistently transfer forces between the two components, then a size effect is not expected to occur because the forces are being averaged at the walls. If these conditions are satisfied, then there are sufficient particles to ensure the flow of forces from one extreme of the model to the other in a steady manner.

### 3.1.6 RST sensitivity to particle size

The sensitivity of the RST test to particle size was then investigated despite the fact that the unconfined compression strength test did not show dependency to this variable in preliminary testing. However, the nature of the test itself is significantly different depending on the number of particles in contact with the wall which represents the cutter during the actual rock scratching. Because of this assumption of the model, the sensitivity of the test to particle size will be considered.

The analysis began by considering low strength rocks. The default $R_{rat}$ used in the model to this point, and considered standard in this analysis, was 3.5. Sensitivity was evaluated by

analyzing the model with a lower bound $R_{rat}$ of 1.66 and an upper bound of $R_{rat}$ of 4.5 but while maintaining a consistent $R_{min}$. For all cases it was found that the dominant failure mode was still ductile, specifically shallow, failure. A relationship was observed, however, between the $R_{rat}$ and the RST results and is shown in Figure 3.18 below. This plot indicates that a larger $R_{rat}$ produces results which align better with the expected results. Therefore, for low strength rocks, larger particles better capture the behavior of the cutting specific energy.

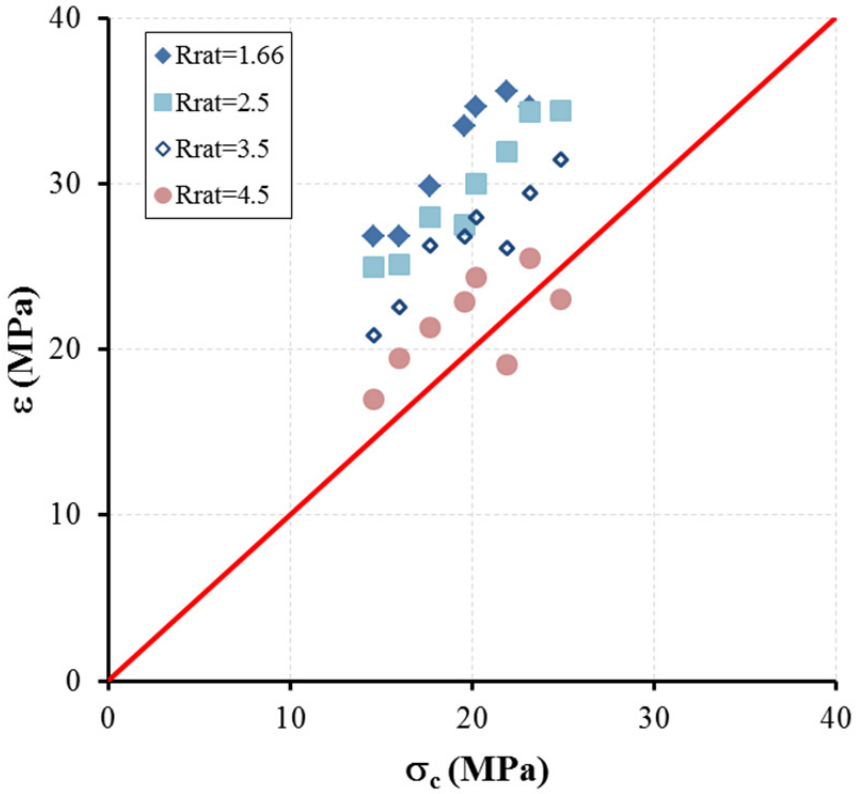


**Figure 3.18** Effect of varying $R_{rat}$ on very low strength DEM rocks under RST

To further investigate this observation, the RST was performed again on the same low strength rock samples using the same particle size distribution range (given by $R_{rat}$ = 4.65) but the minimum radii was varied. Figure 3.19 below presents two cases with a difference in $R_{min}$ between the two cases of approximately 40%. Again, the dominant failure mode was found to be

a ductile failure. It appears that a lower particle radius improves the model as shown in Figure 3.19 where the RST tests run with a lower particle size better fit the line of unity between the specific cutting energy and the unconfined compressive strength. Therefore, the results of the RST appear to be directly dependent on the actual particle size rather than the particle size distribution.

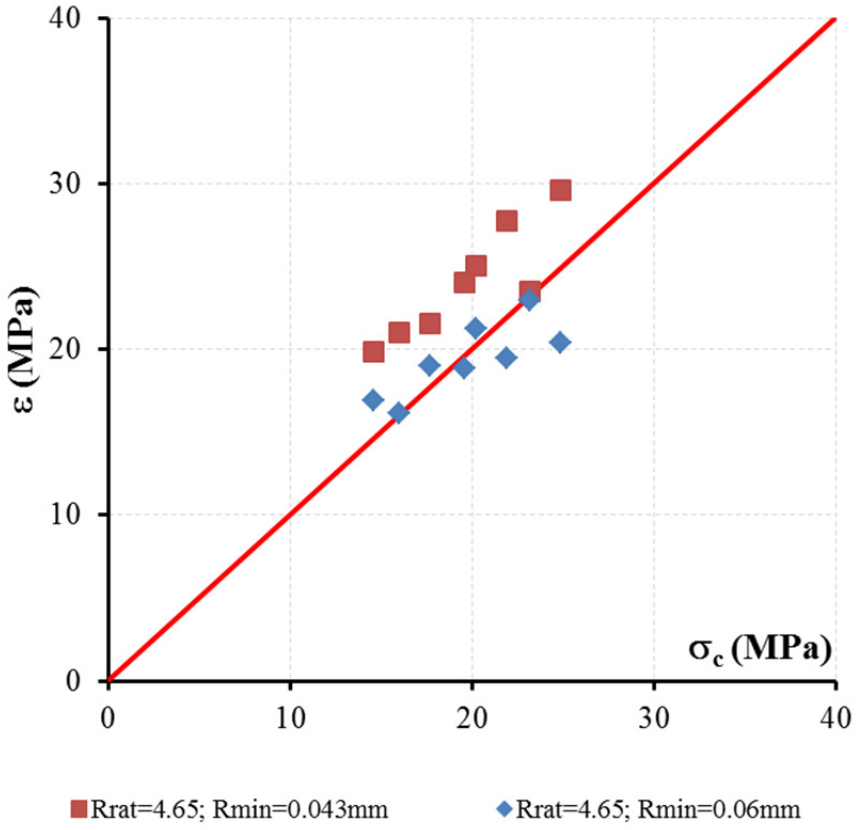


**Figure 3.19** Effect of varying $R_{min}$ with $R_{rat}$=4.65 on very low strength DEM rocks under RST

Once the relationship between the RST results and the particle size had been established, the model could be calibrated with respect to particle size in order to obtain a best fit for the line of unity for low strength rocks. Returning to the default $R_{rat}$ value of 3.5, iterative trials revealed

that an increment of 50% of the original particle size yielded the results most aligned with the line of unity. These results are shown in Figure 3.20 below.

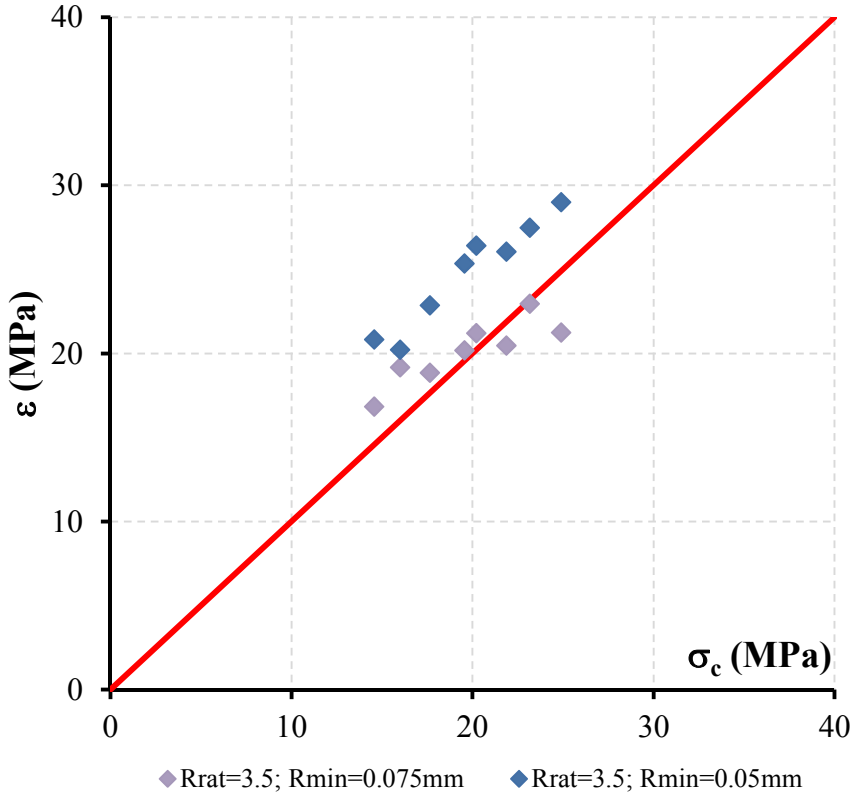


**Figure 3.20** Effect of varying $R_{min}$ with $R_{rat}$=3.5 on very low strength DEM rocks under RST

### 3.1.7 Application of Sensitivity Results and Final Model Calibration

Once the RST model was calibrated using particle size effects for low strength rocks, this significance was investigated for high strength rocks with the intent of calibrating this more problematic part of the model. The same procedure used for investigating the significance of particle size effects for low strength rocks was used for high strength rocks. First, the $R_{rat}$ was

varied but while maintaining a constant $R_{min}$. In order to retain a ductile failure mode, a shallower cutting depth was adopted because the critical cutting depth is smaller for high strength rocks [1], [2]. The results from varying the $R_{rat}$ for high strength rocks are given in Figure 3.21 below.

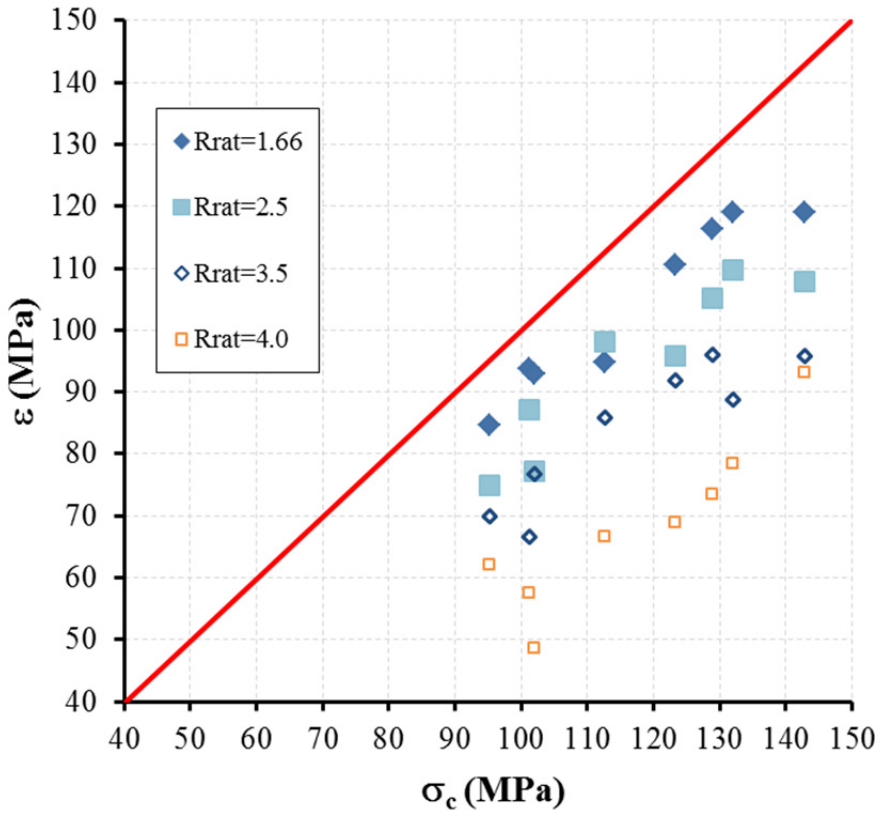


**Figure 3.21** Effect of varying $R_{rat}$ on medium and high strength DEM rocks under RST

As seen from Figure 3.21, the significance of particle size for the results of the RST for high strength rocks is even more pronounced than that of low strength rocks. Therefore, it seems that an optimal particle size based on the strength for different rock types. The intact rock classification method used by Deere and Miller [37] categorizes rocks based on unconfined compression strength and Young's modulus and will be used for rock classification. Recall the

conclusion from the section **RST sensitivity to particle size** that for very low strength rocks (defined as an unconfined compression strength less than 30*MPa*) with an $R_{rat}$ = 3.5, the minimum particle size to yield best fit results was found to be $R_{min}$ = 0.075 mm. High strength rocks, defined as rocks with an unconfined compression strength greater than 110*MPa*, the minimum particle size to best fit the expected results was found to be $R_{min}$ = 0.025 mm. Figure 3.22 shows the improvements of these two strength extremes comparing the adjusted minimum particle sizes (shown with solid points) with the original minimum particle size of $R_{min}$ = 0.05 mm (shown with hollow points).

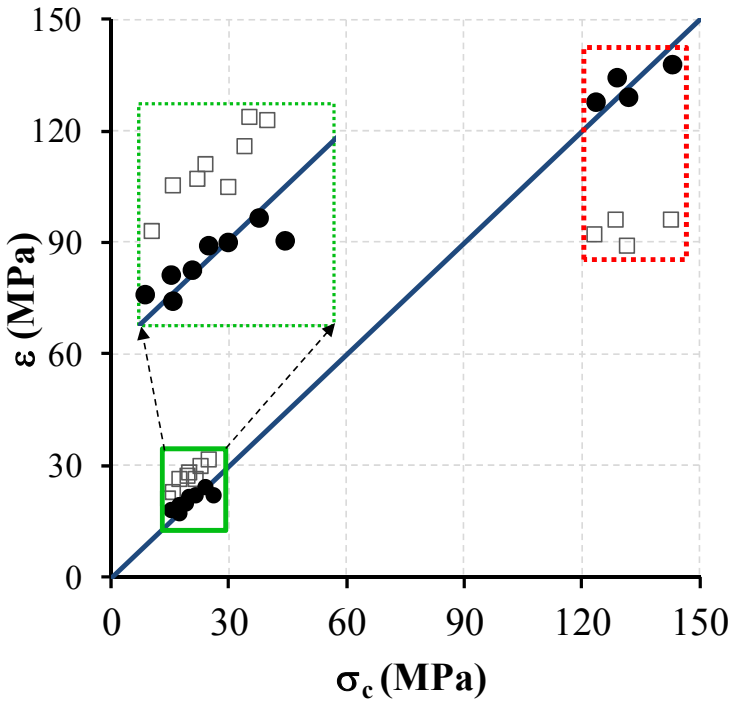


**Figure 3.22** Model improvements at extreme values from adjusting particle size

Additionally, the initial results revealed that within the range of results with an unconfined compression strength of 30*MPa* to 60*MPa* (considered low strength rocks) fit the expected results well when the default particle minimum radius of $R_{min}$=0.05 mm was used.

Additionally, medium strength rocks, or those rocks with an unconfined compression strength between 60*MPa* and 110*MPa* best fit the expected results with a minimum particle radius $R_{min}$ of 0.03 mm. However, all samples maintained the same ratio of maximum particle radius to minimum particle radius of 3.5. Therefore, it was found most practical to use this information to assign optimal minimum particle sizes to ranges of rocks that shared similar characteristics rather than refine the relationship as much as the observed trend (refer to Figure from Wong et al 1996). Here, the rock ranges are based on the uniaxial strength and the strength classification for intact rocks by Deere and Miller [37] is used. Table 3.1 shown below summarizes the particle distribution and size for each rock type based on this strength classification.

**Table 3.1** Particle distribution and size by rock type based on strength classification

| **Class** | **Description** | **Uniaxial Compressive strength: UCS (MPa)** | **Minimum particle radius: $R_{min}$ (mm)** |
|---|---|---|---|
| A | Very high strength | > 224 | N/A |
| B | High strength | 112 – 224 *(> 110)** | 0.025 |
| C | Medium strength | 56 – 112 *(60 – 110)** | 0.030 |
| D | Low strength | 28 – 56 *(30 – 60)** | 0.050 |
| E | Very low strength | < 28 *(< 30)** | 0.075 |

* The values between parenthesis are the ranges that we are approximating

In conclusion, the initial RST results obtained from the full set of samples using PFC2D software yielded values that differed in less than 5% for rocks with an unconfined compressive strength less than 60*MPa*. For rocks with a strength exceeding this value, the RST results do not align with expected values, as seen in Figure 3.23 below. Several variables were investigated such as stiffness of the sample, the influence of particle crushing, the particle distribution range

(defined as the difference between the smallest and largest particle), the particle size variance, and the damping ratio, among others.

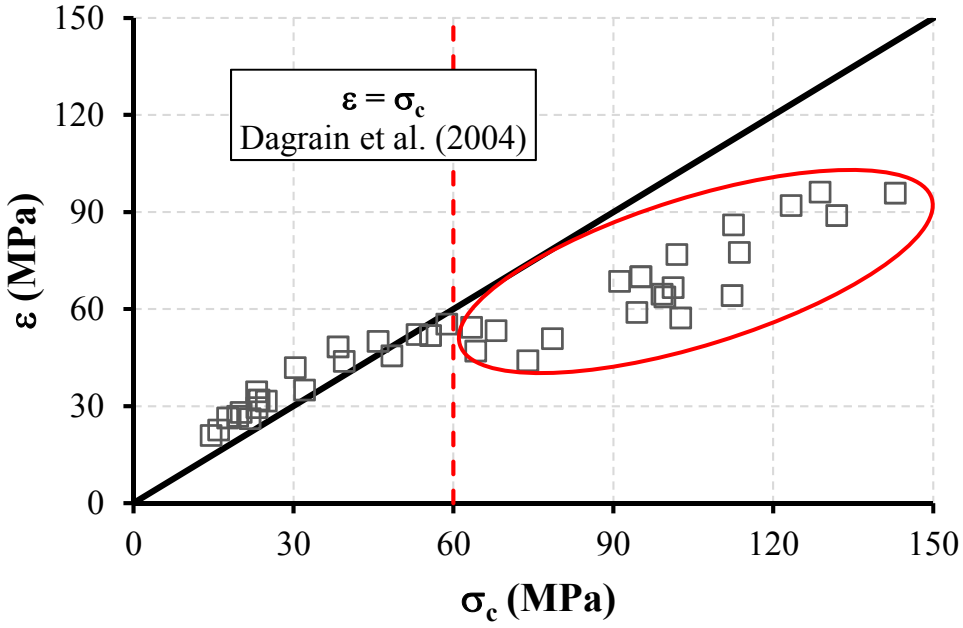


**Figure 3.23** Preliminary RST simulation results in a set of 58 samples

Each of the variables influences the results differently. For instance, decreasing the damping ratio changes the failure mode of the cutting from ductile to brittle; decreasing the velocity of the cutter similarly influences cutting behavior; but these do not significantly impact the cutting forces. It was the particle size, however, which most strongly affected the RST model. Recall that the elastic response of the PFC2D rock-like materials was unaffected by the particle size as concluded by Potyondy and Cundall [3], thus the unconfined compressive strength was independent of particle size; however, it was found that the RST maintains dependence on the geometrical characteristics of the particles as depicted in Figure 3.24 below.

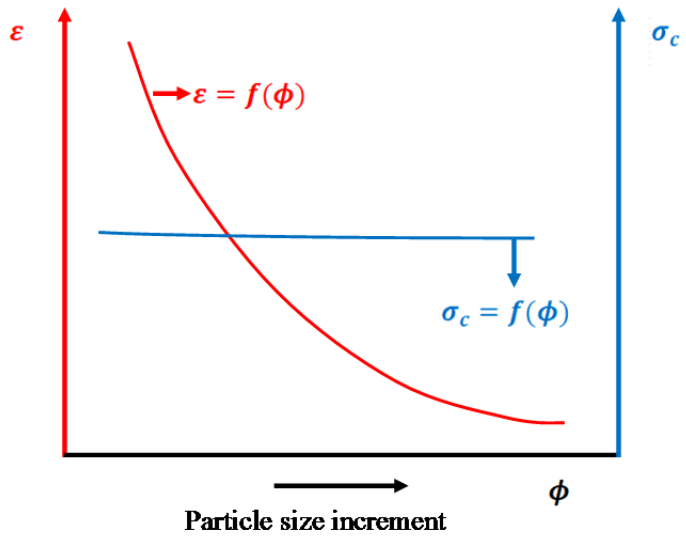


**Figure 3.24** Influence of the particle size in both the cutting specific energy and the unconfined compressive strength

When considering the effect of particle size, the RST results improved to align well with experimental results obtained by Dagrain [2]. Both results, the experimental and the numerical, are displayed in Figure 3.25.

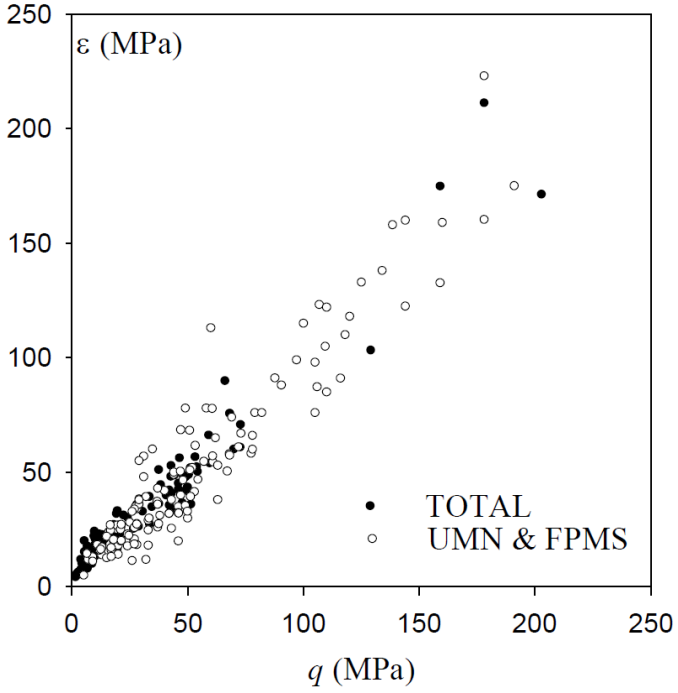


**(a)**

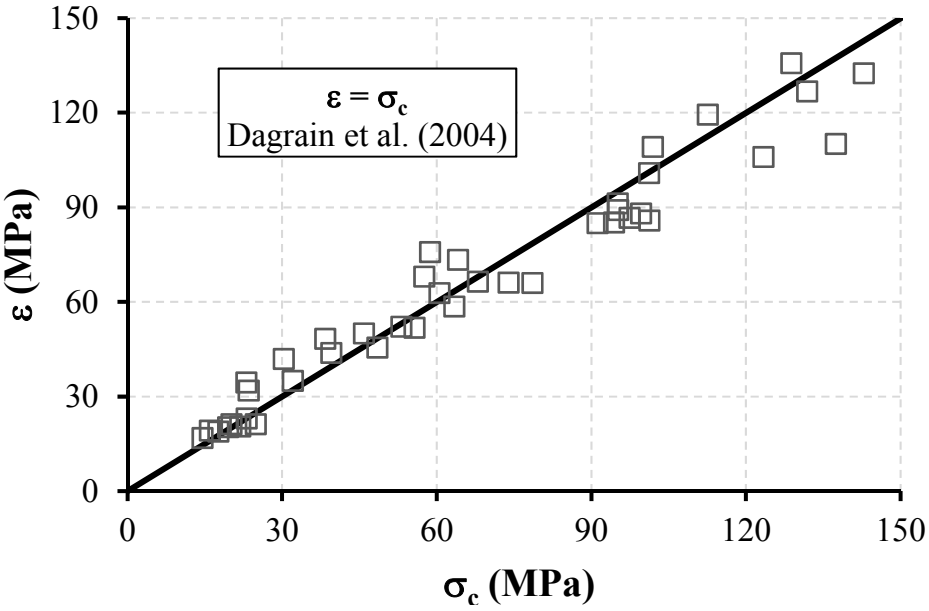


**(b)**

**Figure 3.25** RST (a) experimental [2] and (b) numerical results

### 3.1.8 On the Variability of DEM Modeling of RST

The cutting force history has proven to be an extremely daunting task to reproduce via numerical modeling. In the modeling of the RST using DEM, different types of force history patterns have been reported as shown in Figure 3.25 below, but none closely resemble the 'white noise' history that is recorded in reality.

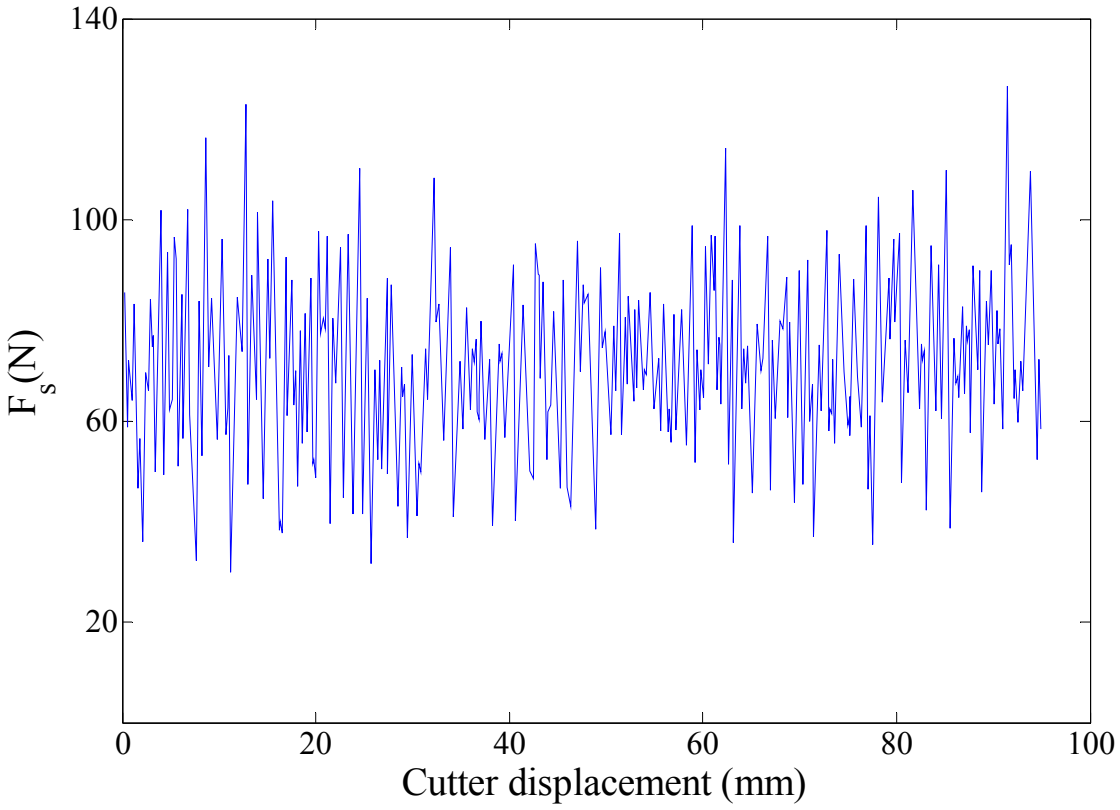


**Figure 3.26** Cutting forces history for Vosges Sandstone after Richard (1999) [1]

Despite efforts to replicate the cutting force history and the improvement that earlier studies presented (refer to Figure 3.27 below) [47] (2010), there is still significant variability within the cutting forces, hence, imposing a bigger margin of error when forces are averaged in

order to obtain the cutting specific energy is needed. Further investigation of this problem will now be presented and discussed.

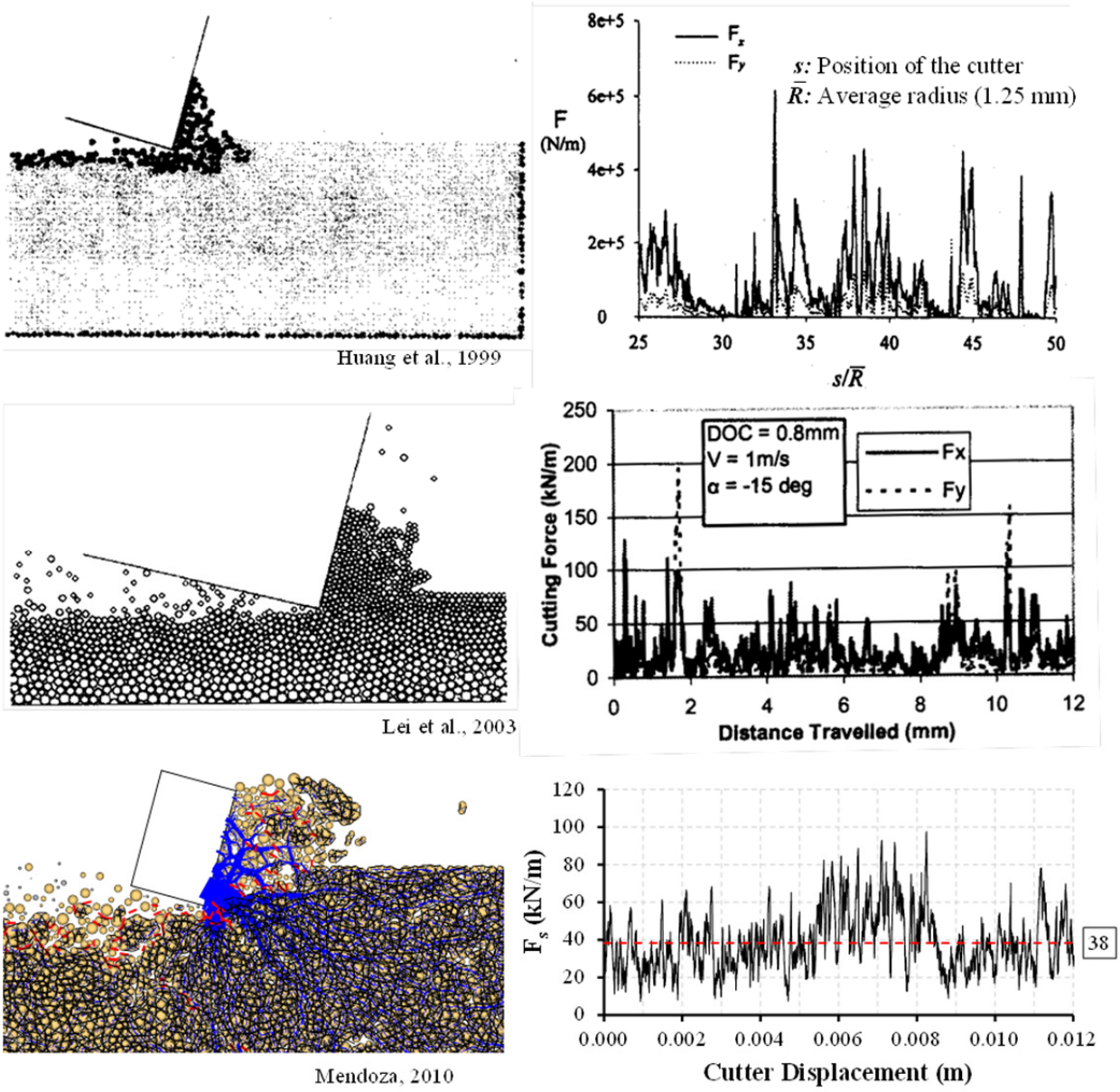


**Figure 3.27** Comparison of cutting force histories

Meticulous observation of the simulated cutting process provided insight as to why the variability was so much larger than expected. It was observed that the chain of forces in front of

the cutter vanish while the rock is being cut due to the loss of contact with the cutter face. With this information, it can be hypothesized that despite the fact that the 2D model has an implicit unit depth, it may not be enough to capture the rock's variability in the direction of the depth. While scratching can be, and often is, represented with a 2D model, there is information lost with the missing dimension. However, it would be possible to implement this information implicitly using a 2D model if the following consideration is made. The sketch shown in Figure 3.28 below shows a rock sample divided into three slabs. If each division represented a 2D model and the cutting forces obtained from each case were averaged, then a representative force history from the entire rock would be obtained.

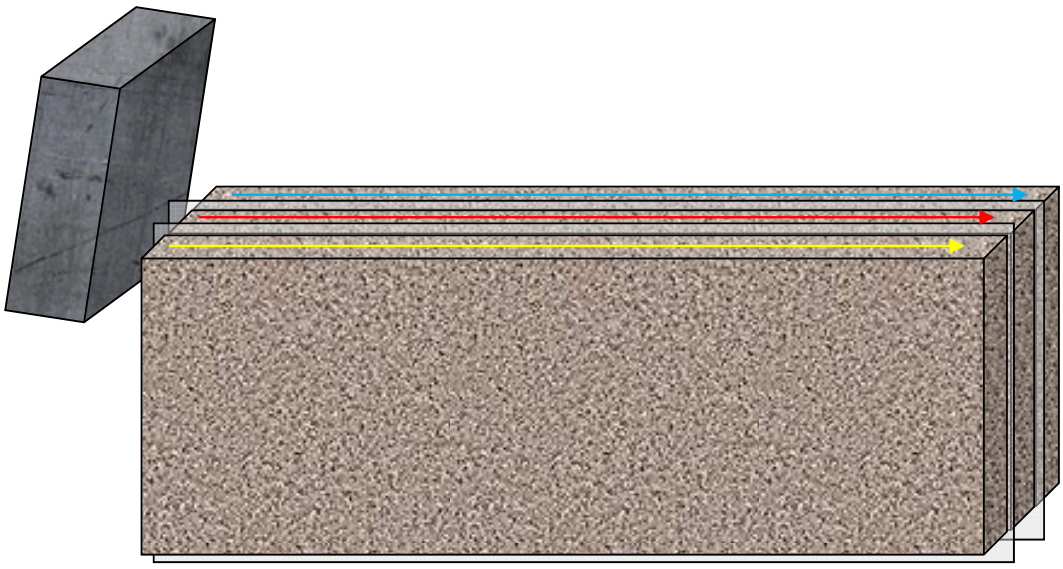

**Figure 3.28** Division of 3D rock sample into 2D slices

To test this hypothesis, ten RST tests were performed to the same rock (material), that is, rocks with the same microproperties but with a different particle arrangement. The results from these cutting force histories are depicted in Figure 3.29 below. From these plots, it is clear that the particle arrangement controls the shape of the force history. Furthermore, the averages from

the forces tend to fall close to a common value but the scatter of these average forces demonstrate the magnitude of the variability of the cutting force histories in the 2D model.

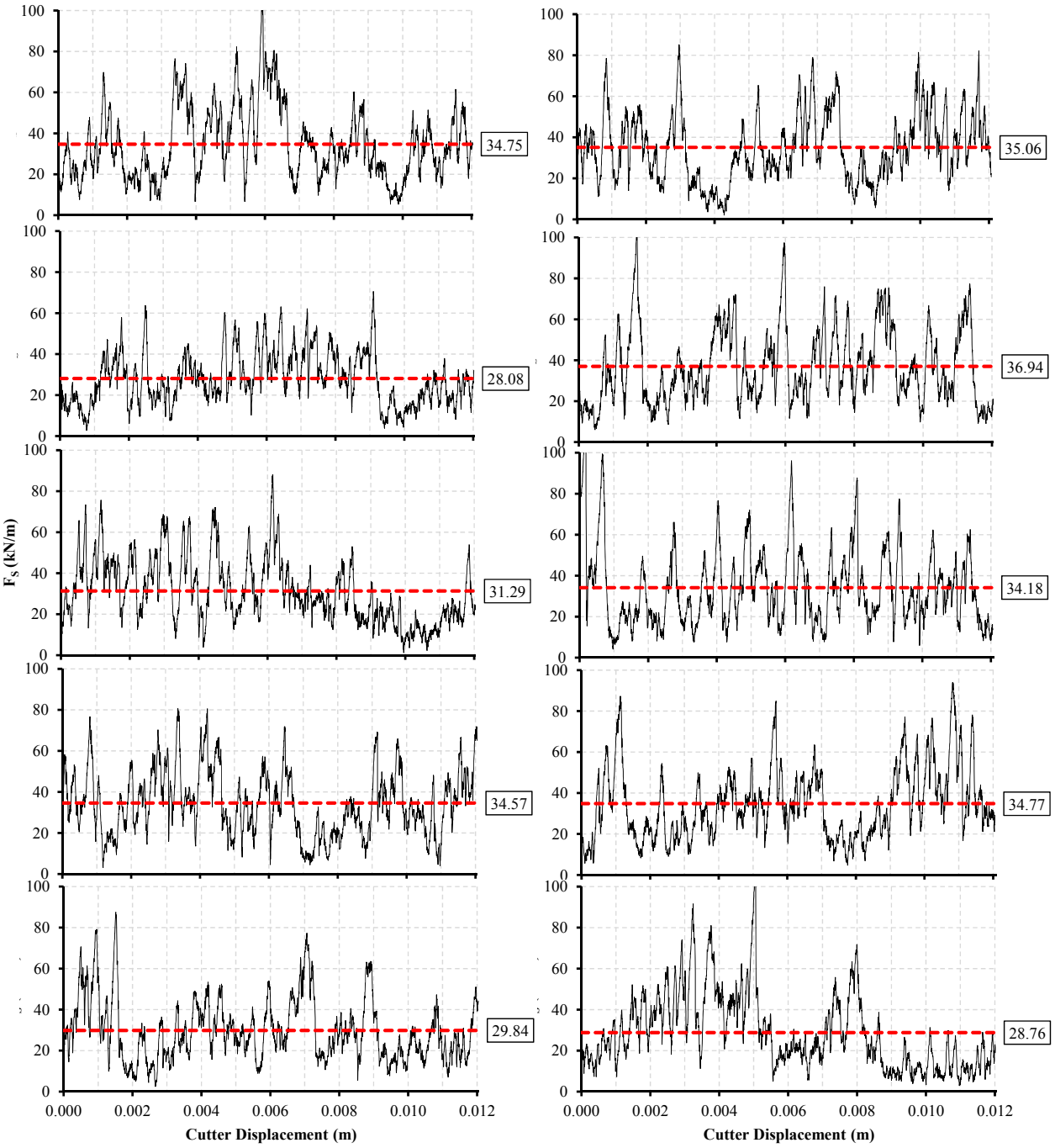


**Figure 3.29** 10 cases of RST force histories

The forces from these results were then summed at every point and average values were obtained. Figure 3.30 below shows the result of the procedure described above. These results verify that the cutting force history variability decreases dramatically and therefore, the confidence values associated with the averaged forces is much higher. Additionally, the results also validate the hypothesis regarding missing information in the depth direction of the 2D model and offer a method of obtaining results as consistent as those obtained with a 3D model (Refer to the section **3D Rock Cutting Simulations)**.

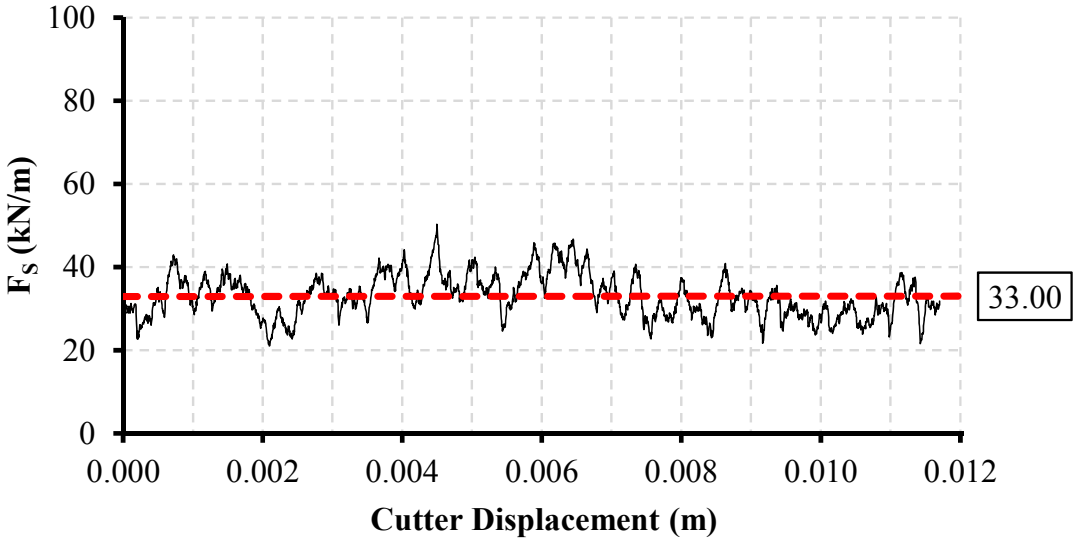


**Figure 3.30** 10 averaged cases of RST force histories

## 3.2 3D ROCK CUTTING SIMULATIONS

Three-dimensional simulations of the RST were also performed in order to pinpoint the differences with the results from the simpler 2D analysis. For the three-dimensional analysis

groove cutting and slab cutting analyses were first performed to a rock with very low strength, UCS = 20$MPa$.

Figure 3.31 shows the 3D cutting sample before being cut and during the cutting process using a narrow cutter as used in groove cutting. Broken bonds are indicated by particles colored red or magenta in the figure below.

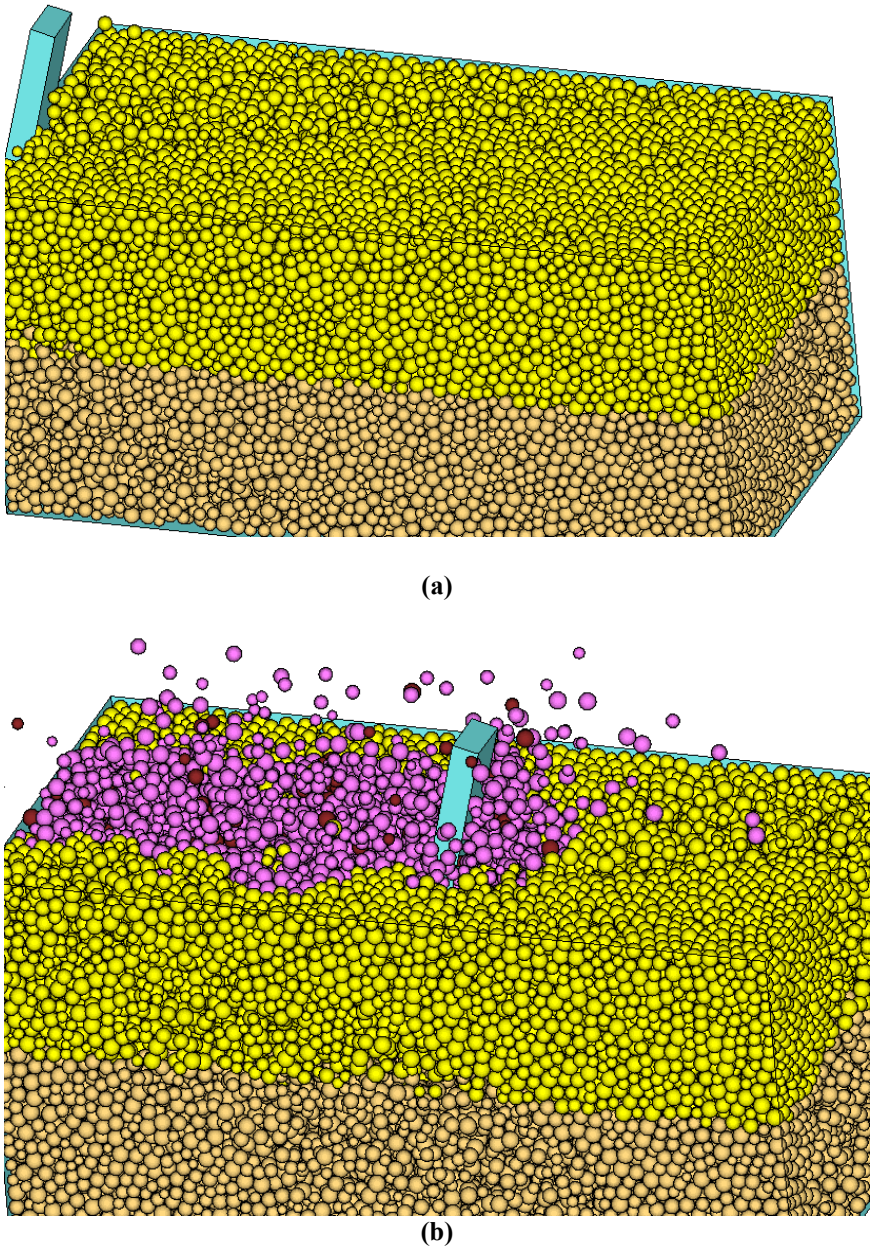

**(a)**

**(b)**

**Figure 3.31** DEM modeling of groove cutting (a) initial configuration (b) a snapshot during cutting

The cutting force histories for the cases of the narrow cutter and the slab cutter are depicted in the Figure 3.32 below. The narrow groove cutter resulted in scattered data as shown in Figure 3-34 (a) while it can be seen that the slab cutting test results were relatively smooth, as seen in Figure 3-34 (b) below. However, both sets of data result in the same average value.

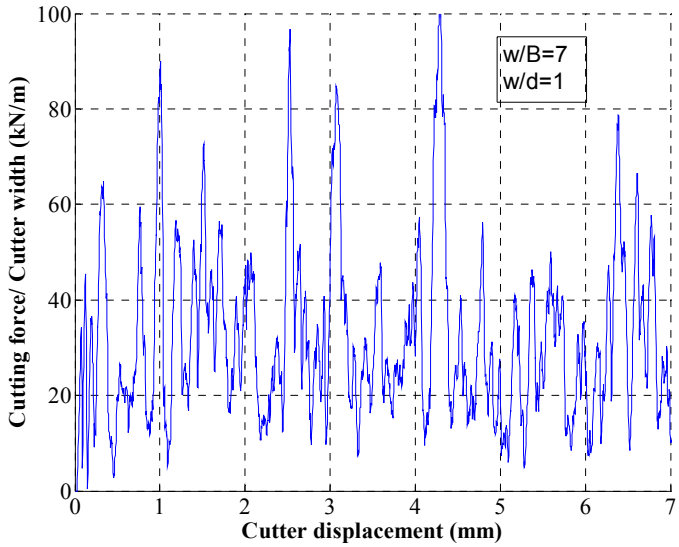


**(a) *w/d*=1**

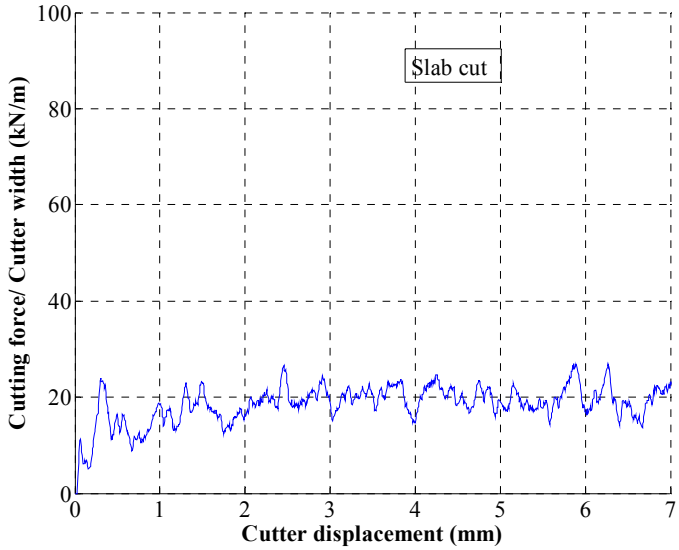


**(b) *w/d*=7**

**Figure 3.32** Cutting force time histories for (a) a narrow groove cut, and (b) a slab cut

These results agreed well with the analysis and hypothesis made in the section ***On the Variability of DEM Modeling of RST***, which combined the two-dimensional results in order to decrease the variability of the overall results. Like the 2D results, the trends found in the 3D results can be attributed to the amount of particles in contact with the cutter. A wider cutter reduced the variability of the cutting results as expected and consistently, a narrower cutter increased the variability of the results. In 3D analysis, however, the particle flow in front of the cutter is much clearer than that seen in the 2D analysis and no chipping developed. Altogether, PFC2D has the ability of modeling the white noise pattern of the horizontal forces as observed in the three-dimensional simulations and in the laboratory results. This is corroborated with Figure 3.33 below where rock scratching tests were performed in 2D and 3D samples with close uniaxial compressive strengths.

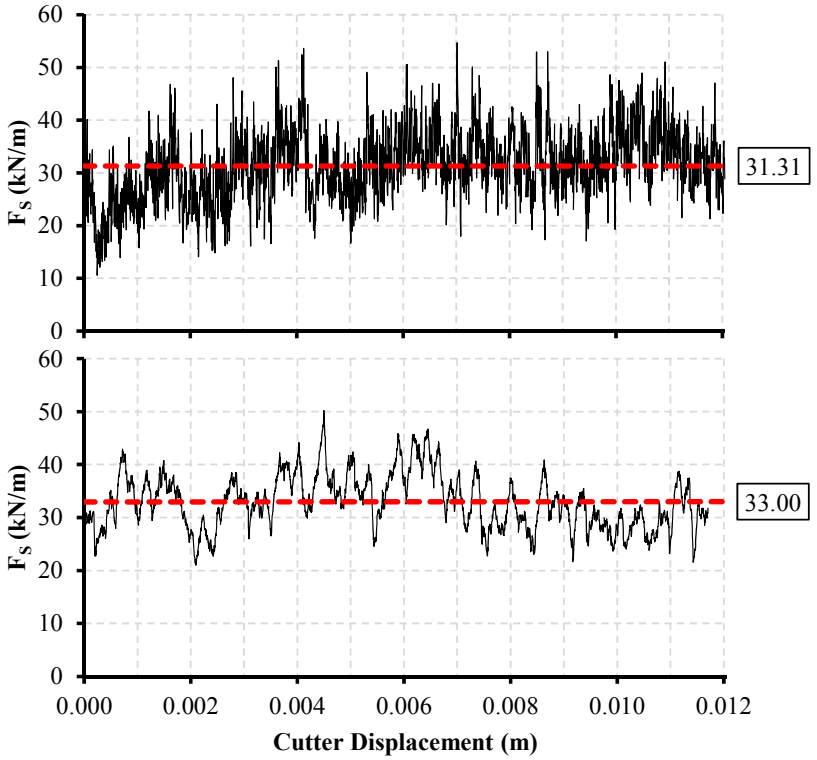


**Figure 3.33** Force history of DEM 2D and 3D Rock Scratching Tests

# 4.0 IMPLICIT MODELING OF POROSITY IN A DEM ROCK MODEL

In general, rock porosity is not typically reproduced in a Discrete Element Model. Thus, rock-like numerical materials, from dense hard rocks to porous soft rocks, are being created without considering the influence of this parameter on the mechanical responses. This study explores whether or not the current approach of not incorporating the actual rock porosity in a discrete element model affects the validity of the results.

Specifically, it has been hypothesized that if the macroproperties of a rock (e.g., Unconfined Compressive Strength (UCS), Young's Modulus, Tensile Strength), are captured in a discrete element model, the porosity does not need to be explicitly incorporated. To test this hypothesis, the UCS, direct tension, rock scratching and indentation tests were modeled with the discrete element model and the results with respect to different porosity levels were compared.

## 4.1 JUSTIFICATION OF IMPLICIT MODELING OF POROSITY

### 4.1.1 Influence of Porosity on Unconfined Mechanical Properties

It is intuitive that rocks with a denser particulate structure are more likely to have higher strength than those with a less dense particle arrangement. It can be seen from Figure 4.1 that the uniaxial strength and stiffness are affected by the porosity of a rock sample. Therefore, rocks with lower

porosities are not only stronger but also stiffer than those with higher porosity values. There are exceptions to this general trend, but this overarching relationship, rather than potential exceptions, will be the focus of this study.

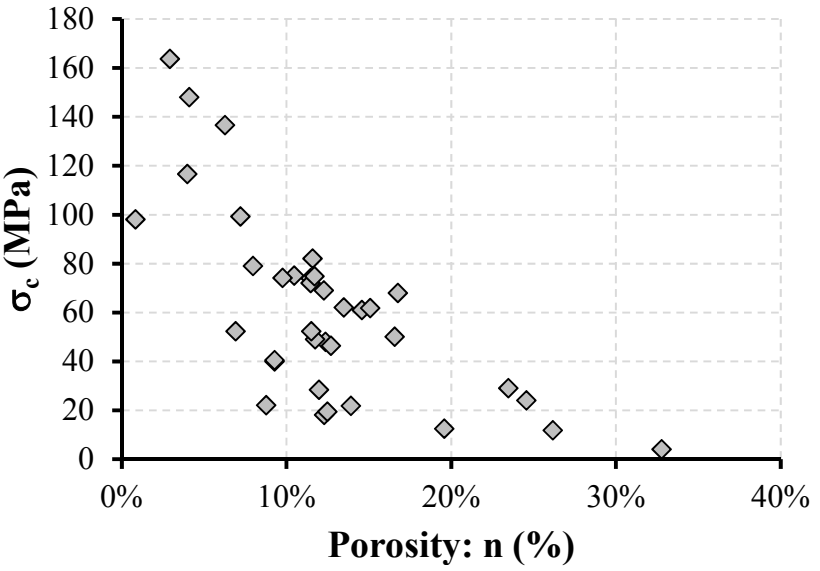


**(a)**

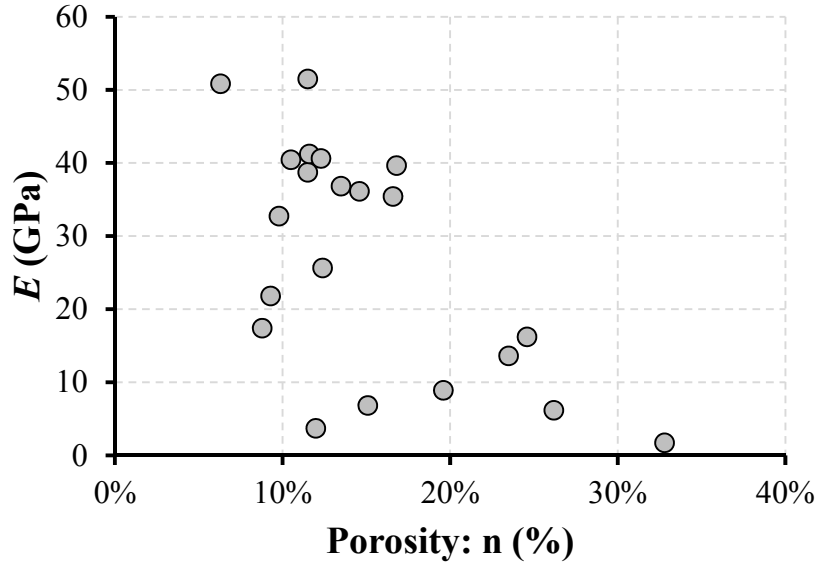


**(b)**

**Figure 4.1** Compilation of (a) Unconfined Compressive Strength (UCS) and (b) Young's Modulus results of rocks with different porosities. Bell (2000) [38]; Hale & Shakoor (2003) [48]

One of the most comprehensive and extensive studies regarding the influence of porosity on mechanical properties in a DEM model by Schöpfer et al. [36] confirms this relationship between stiffness or strength and porosity. This study, conducted for three-dimensional rock materials, also observed the trend that increasing porosity led to decreasing strength and stiffness. In the present study, however, the two-dimensional case was investigated and similar trends observed.

In the present study, a sample with very low strength was first created which yielded an initial porosity close to 16%, considered a standard value for a PFC2D sample generation procedure. Using this sample, porosity was decreased using the method described in the section ***Creating a rock sample of low porosity***. Samples with porosities of n = 12%, 10% and 8% were created, and first subjected to UCS testing. Three samples, each with different particle arrangements, but with identical material and porosity values were used in each test and the results were averaged and are presented in Figure 4.3. The microproperties used for this case study are given in Table 4.1.

**Table 4.1** PFC2D microproperties

| GRAINS (PARTICLES) | CEMENT (PARALLEL BONDS) |
|---|---|
| $\boldsymbol{\rho = 2630\ kg/m^3}$<br>$\boldsymbol{E_c = 1\ GPa}$<br>$\boldsymbol{R_{max}/R_{min} = 3.5}$<br>$\boldsymbol{R_{min} = 0.2 \times 10^{-3}\ m}$<br>$\boldsymbol{k_n/k_s = 1\ \therefore\ k_n = 2tE_c\ , t = 1}$<br>$\boldsymbol{\mu = 0.5}$<br><br>**Where,**<br>$\boldsymbol{\rho}$ : Density<br>$\boldsymbol{n}$ : Porosity<br>$\boldsymbol{R_{max}}$ , $\boldsymbol{R_{min}}$ : Maximum and minimum radius, respectively<br>$\boldsymbol{E_c}$ : Young sModulus<br>$\boldsymbol{k_n}$ : Normal Stiffness<br>$\boldsymbol{k_s}$ : Shear Stiffness<br>$\boldsymbol{\mu}$ : Friction | $\boldsymbol{\bar{\lambda} = 1}$<br>$\boldsymbol{\bar{R} = \bar{\lambda} \times min(R^{(A)}, R^{(B)})}$<br>$\boldsymbol{\bar{E}_c = 1\ GPa}$<br>$\boldsymbol{\bar{k}^n/\bar{k}^s = 1\ \therefore\ \bar{k}^n = \bar{E}_c/(R^{(A)} + R^{(B)})}$<br>$\boldsymbol{\bar{\sigma}_c = 0.5\bar{\tau}_c = (mean \pm std.dev.)}$<br>$\boldsymbol{\therefore\ mean = 10\ MPa\ ;\ std.dev. = 23\%}$<br><br>**Where,**<br>$\boldsymbol{\bar{\lambda}}$ : Bond Radius Multiplier<br>$\boldsymbol{\bar{R}}$ : Bond Radius<br>$\boldsymbol{R^{(A)}}$, $\boldsymbol{R^{(B)}}$: Radius of particle in contact A and B, respectively<br>$\boldsymbol{\bar{E}_c}$ : Young's Modulus<br>$\boldsymbol{\bar{k}^n}$ : Normal Stiffnes<br>$\boldsymbol{\bar{k}^s}$ : Shear Stiffnes<br>$\boldsymbol{\bar{\sigma}_c}$ : Normal Strength<br>$\boldsymbol{\bar{\tau}_c}$ : Shear Strength |

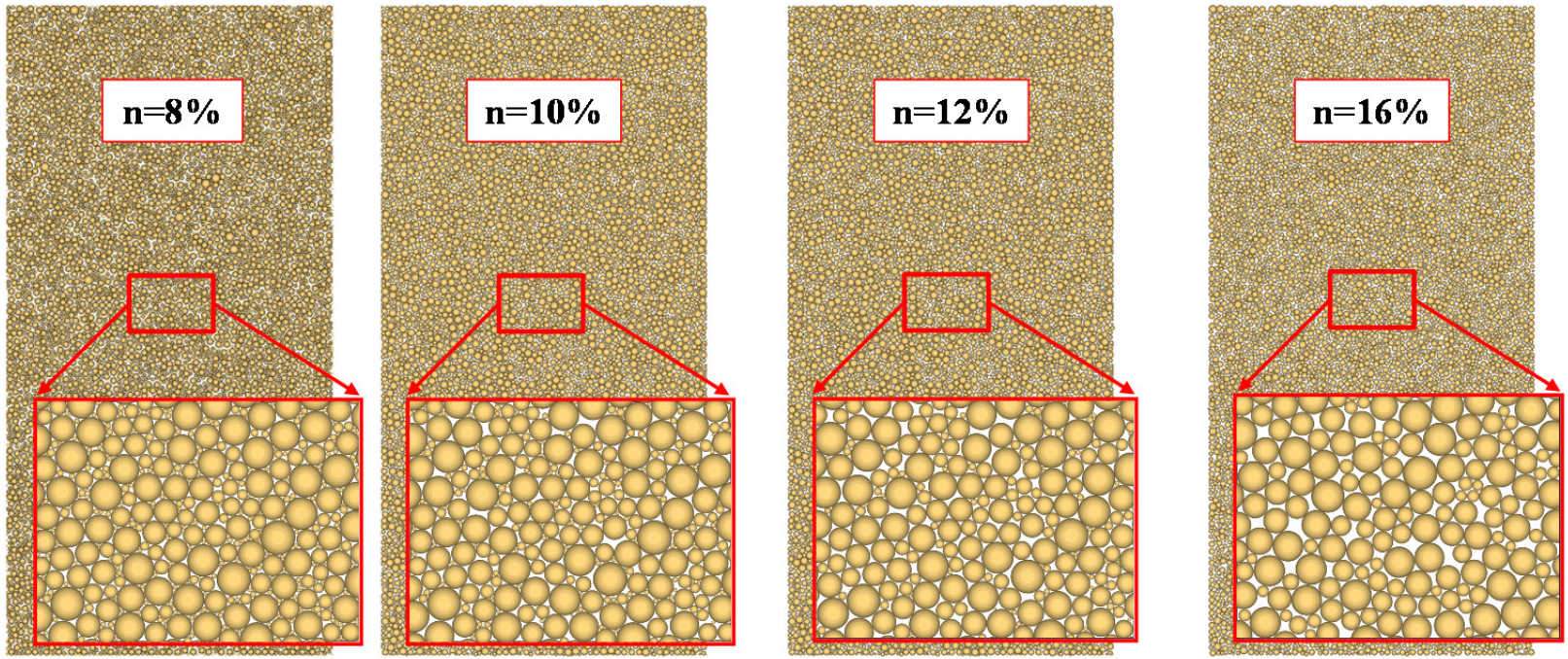


**Figure 4.2** DEM samples with varying porosities

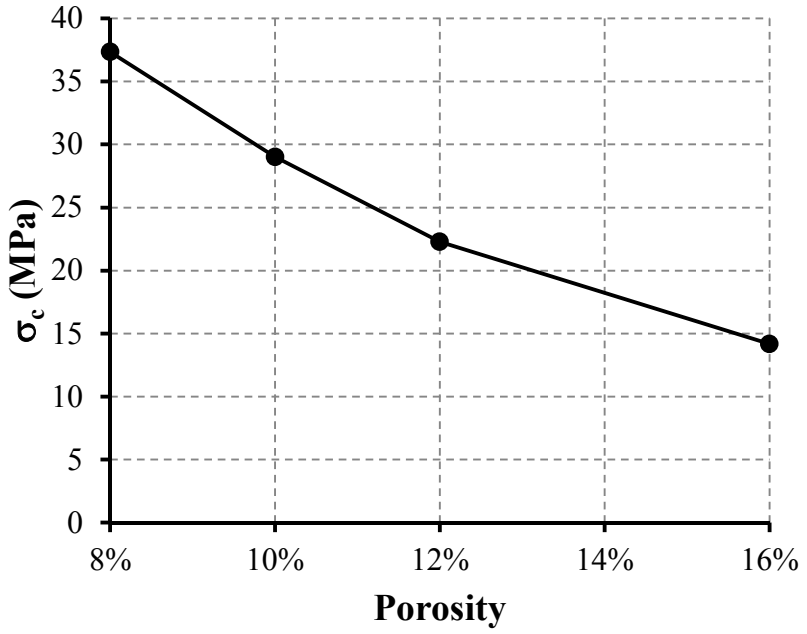


**(a)**

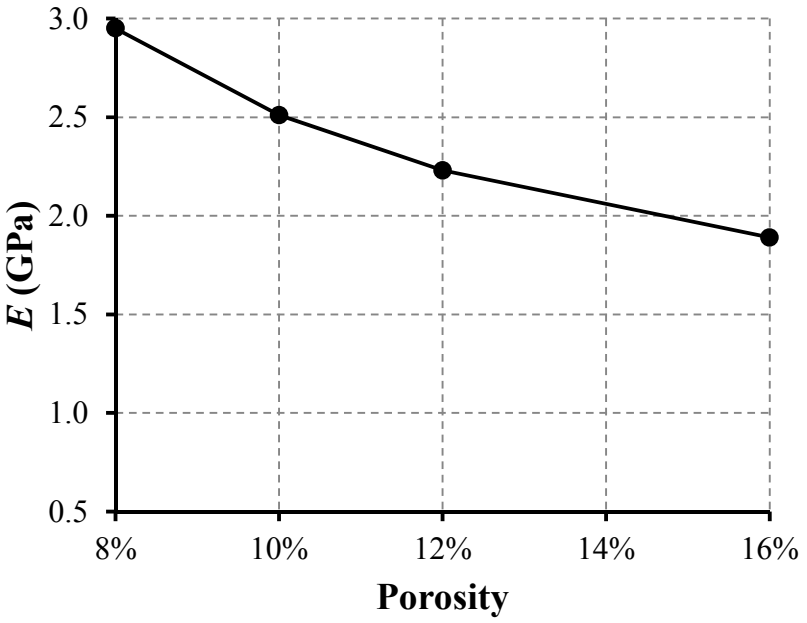


**(b)**

**Figure 4.3** DEM macroproperties of a rock with different porosities: (a) UCS and (b) Young's Modulus

In order to check the validity of the trend observed from the results, the strength and stiffness values were normalized and plotted against normalized laboratory results compiled and presented as described above and are shown in Figure 4.4 below

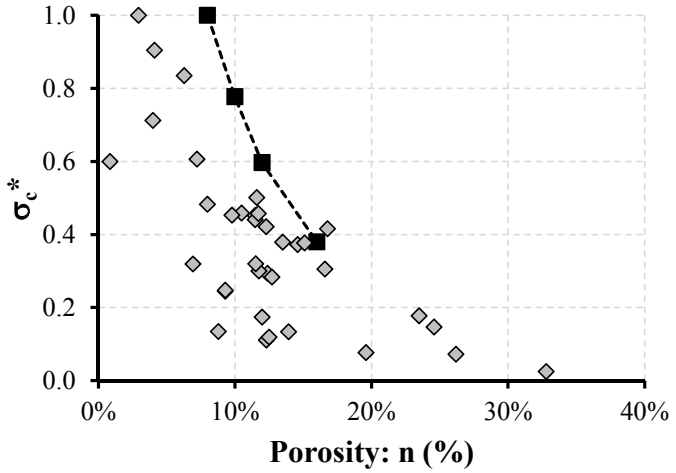


**(a)**

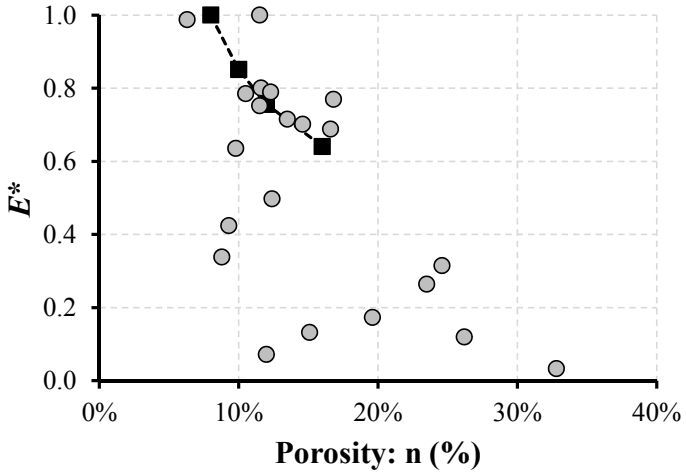


**(b)**

**Figure 4.4** Comparison of trends of laboratory and simulation normalized results (a) UCS and (b) Young's Modulus

These results indicate that DEM can easily capture the influence of porosity on the mechanical properties of a rock sample; however, the computational efficiency can substantially decrease as porosity increases, especially for values typical of shales and dolomites. This is a strong contributing reason to further pursue the analysis of implicitly modeling porosity.

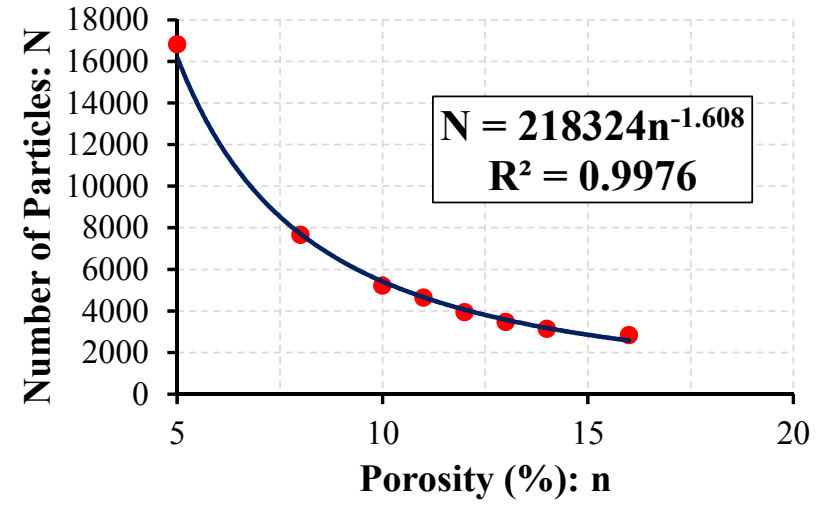


**(a)**

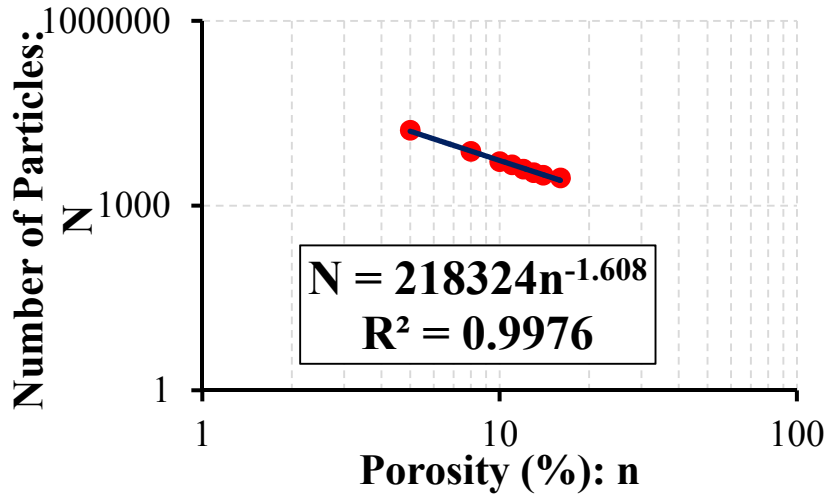


**(b)**

**Figure 4.5** Effect of decreasing porosity on number of particles present in a sample

The effect of increasing porosity on decreasing computational efficiency can be seen from Figure 4.5. A rock sample was created with an initial porosity of 16% and approximately 2500 particles. When the original porosity of the sample was decreased by half (to n = 8%) the number of particles required doubled. A system with more particles requires more calculations and therefore, more total time is required for the simulation.

### 4.1.2 Effects on Particle Contact Distribution

Inserting new particles into an existing sample represents a modification of the internal contact structure. Therefore, in order to check if the skeleton formed by the particle arrangement experienced modification due to the particle insertion procedure, several samples with different porosities were created and number of contacts and contact particle distribution were analyzed.

Based on the particle insertion procedure, three generations of samples were created. Each generation was characterized by inserting a particle into each existent void formed between particles by means of solving the Apollonius' circle problem. It should be noted that the voids created by particles and walls are not taken into consideration. The first particle insertion procedure created the sample that will be referred to herein as **Generation 1**. Likewise, for the second and third particle insertion, the samples will be referred to as **Generation 2** and **Generation 3**, respectively. The initial sample is referred as **Generation 0**. A more detailed description of this procedure can be found in the section, ***Creating a rock sample of low porosity***.

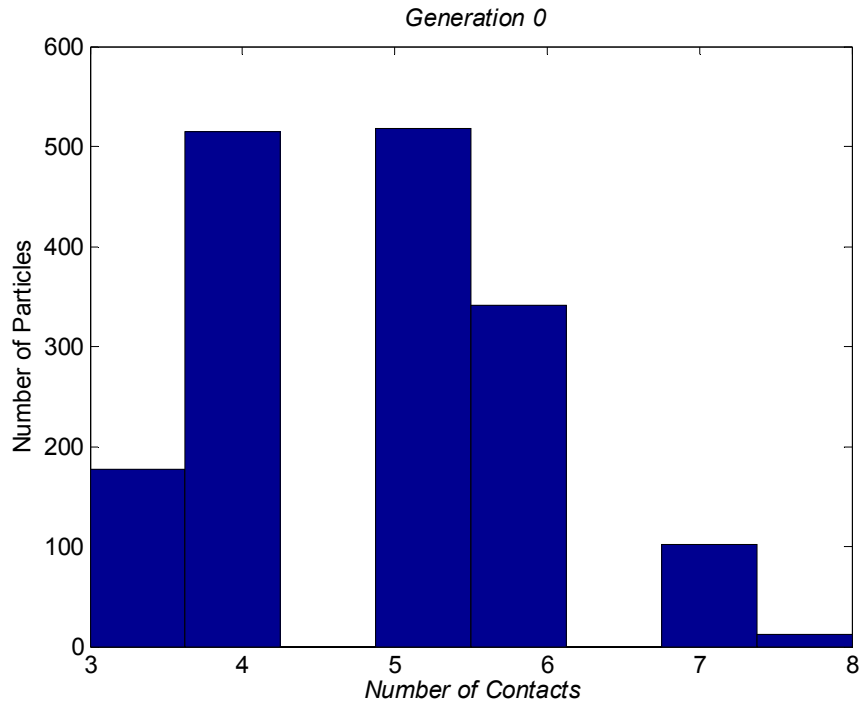


**(a)**

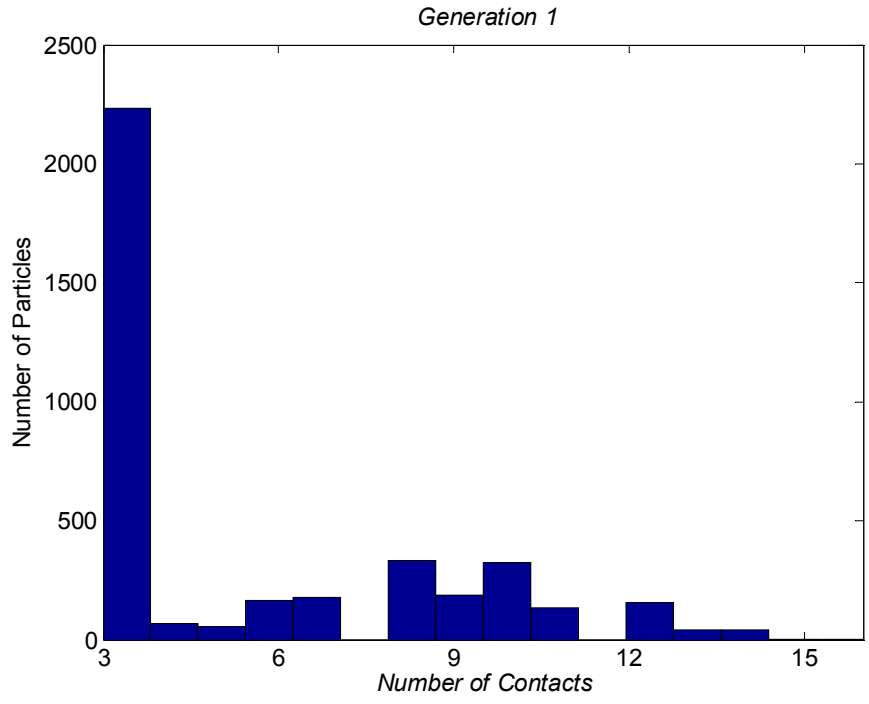


**(b)**

**Figure 4.6** Histograms of the number of contacts in (a) the initial sample and (b) its first generation

Figure 4.6 shows histograms of the number of contacts of the particle for the original sample and its first generation. As the initial sample has particles with 8 contacts, it is expected that for the first generation these same particles will contain twice the original contacts. Consequently, the same will happen for future generations, as depicted by the plot on the left of Figure 4.7. As stated above, it was expected that the **Generation 3** sample would have particles with 64 contacts, as shown on the right side of Figure 4.7

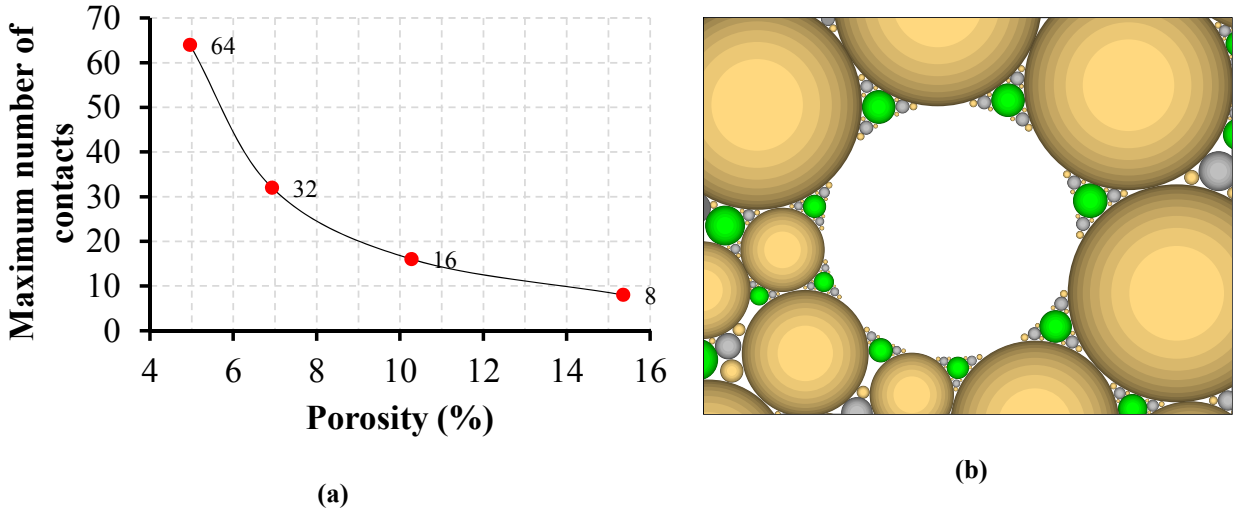


**Figure 4.7** (a) Maximum number of contacts for each sample Generation and (b) the void of left by a particle surrounded and contacted by 64 particles in its boundary.

It becomes clear that particle insertion modifies the initial particle size distribution. However, the extent and effect of these modifications on the mechanical response of the particulate skeleton is not yet clear.

To add credibility to the mechanical results from samples of different porosities (recall from Figure 4.4) the same samples (with porosities of n=8%, n=10%, n=12% and n=16%) were subjected to three different types of confinement environments (refer to Table 4.2) in order to

evaluate whether or not the particle contact structure and/or the diffusion pattern of the contact forces would undergo significant changes as a result of these varying porosities.

**Table 4.2** Different state of stresses to evaluate forces and contact distribution

| Case | State of Stresses | |
|---|---|---|
| **Isotropic** | $\sigma_{yy} = \sigma_{xx}$ | **ISO** |
| **Anisotropic 1** | $\sigma_{yy} > \sigma_{xx}; \sigma_{xx} = 0.5\sigma_{yy}$ | **ANI1** |
| **Anisotropic 2** | $\sigma_{yy} < \sigma_{xx}; \sigma_{xx} = 2\sigma_{yy}$ | **ANI2** |

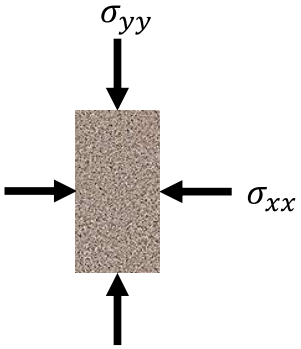


The results of this evaluation are presented from Figure 4.8 to Figure 4.10. Rose diagrams are used to depict the internal forces and direction of the particle contact distribution. It can be seen from the plots that the direction of the contact is a topological characteristic that remains unmodified by particle insertion. It can also be seen that this characteristic is not affected by varying the state of stresses.

Despite the fact that the cases analyzed in this study were always initialized using an isotropic state of stresses, an unexpected observation was made worthy of further investigation. The samples that had undergone anisotropic treatment yielded macromechanical results significantly different to the isotropic case. This finding is discussed further in the section ***EFFECT OF THE INITIAL STATE OF STRESSES ON THE DEM MACROMECHANICS***.

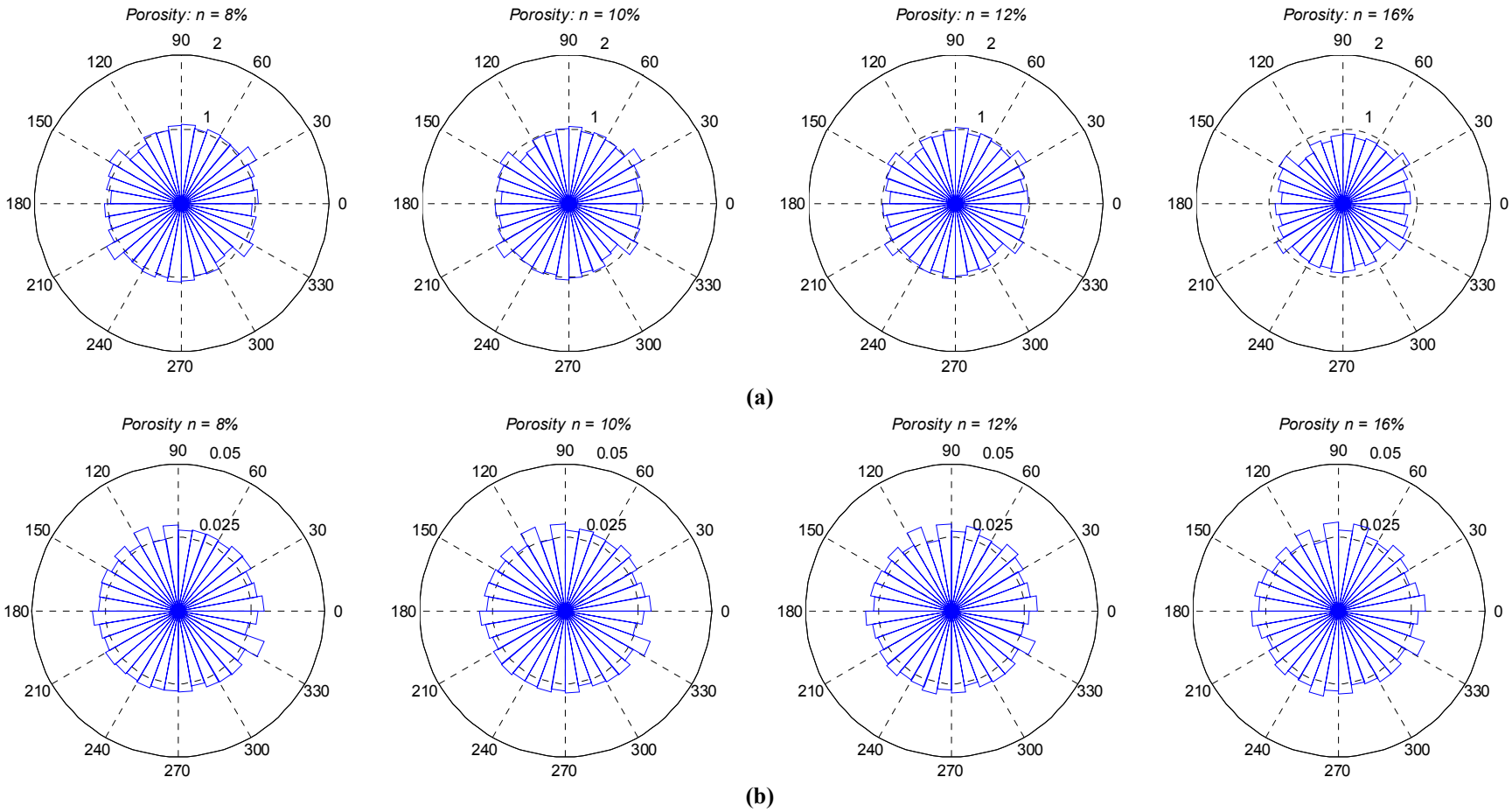


**Figure 4.8** (a) Internal forces of the isotropic state and (b) its particle contact distribution

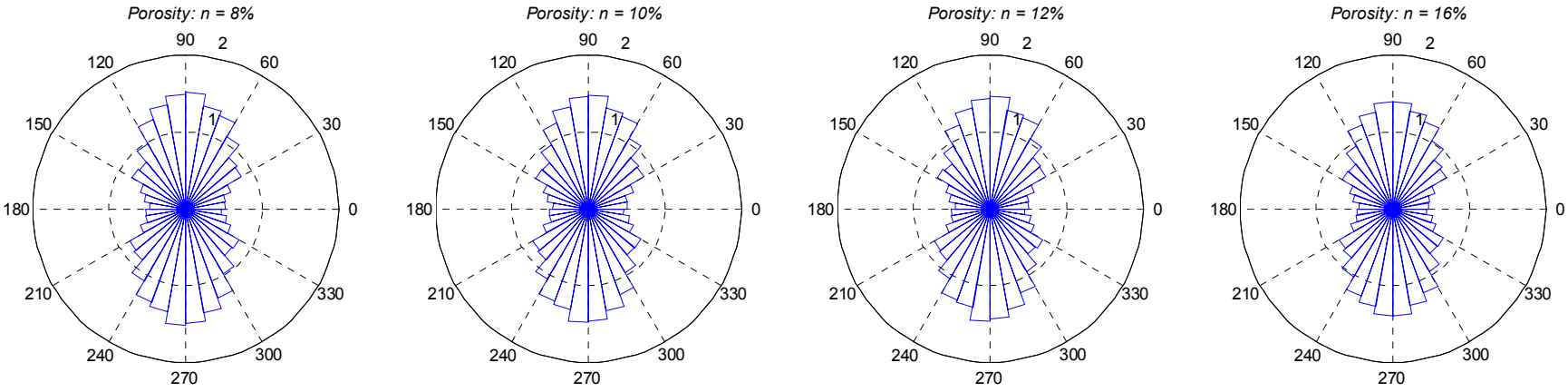


**(a)**

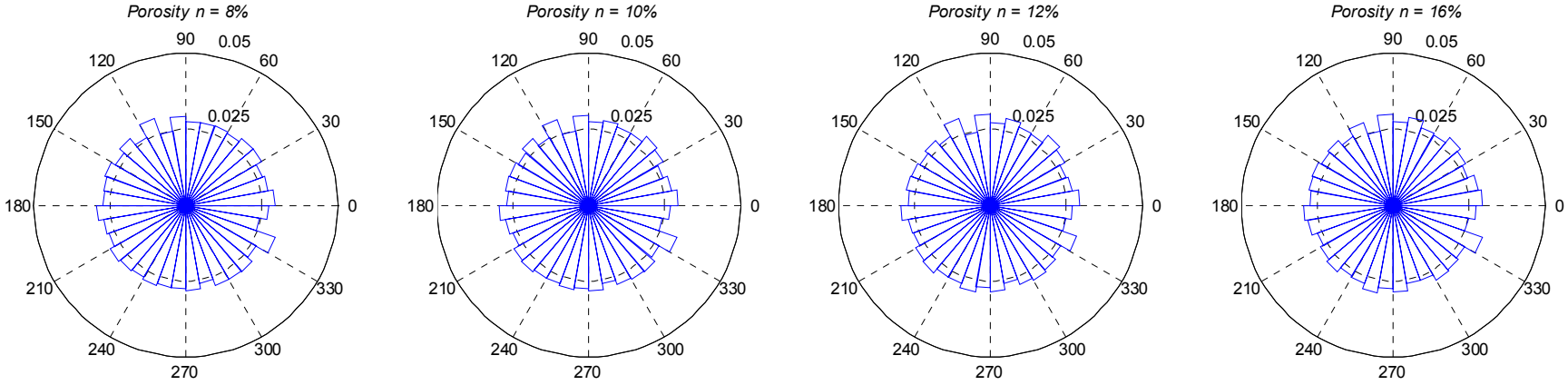


**(b)**

**Figure 4.9** (a) Internal forces of the anisotropic state (Case I) and (b) its particle contact distribution

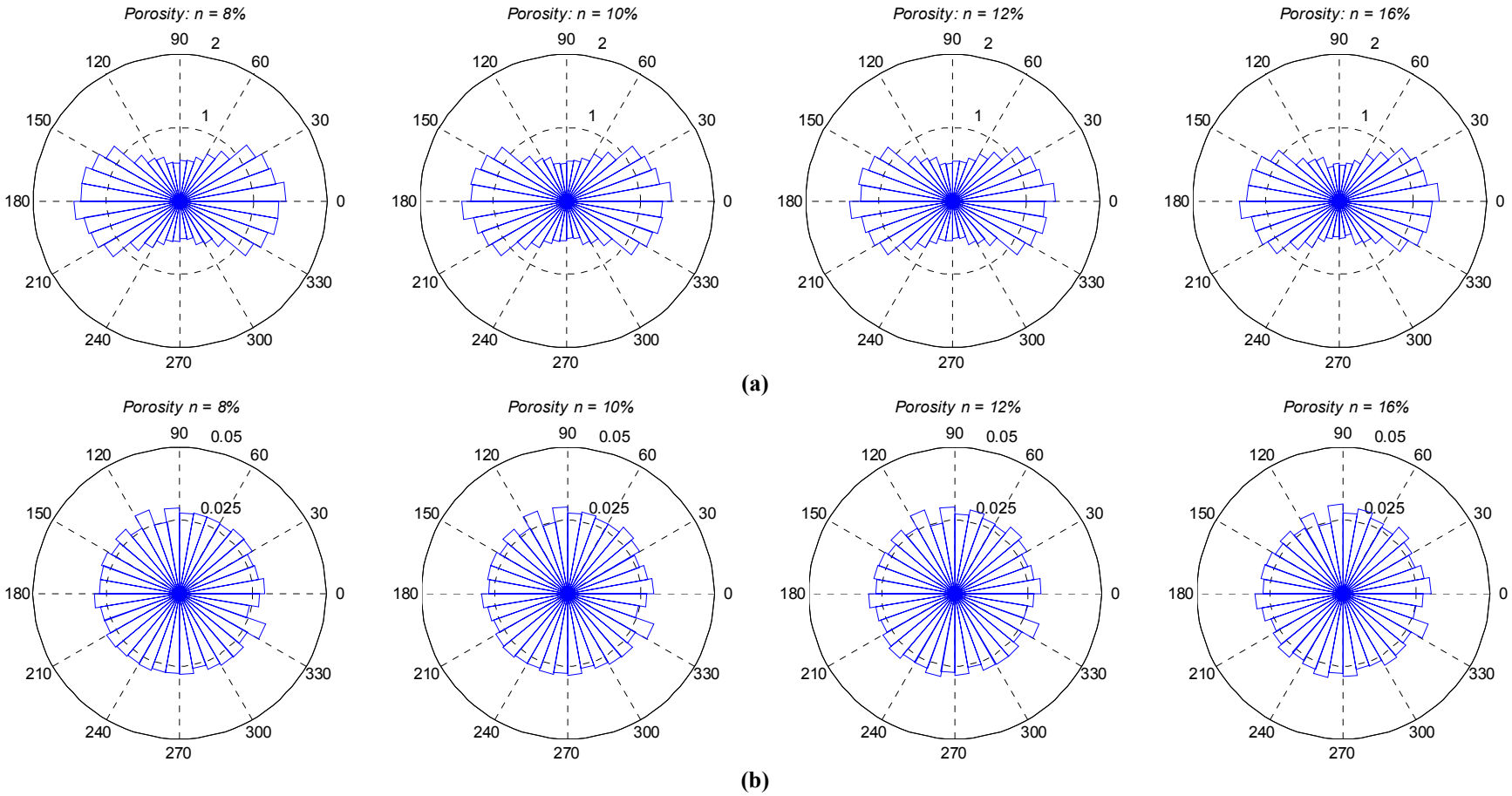


**Figure 4.10** (a) Internal forces of the anisotropic state (Case II) and (b) its particle contact distribution Anisotropic 2 forces

## 4.2 IMPLICIT MODEL BASED ON VARYING MICROPROPERTIES

Once it had been established that the structure of the particle contacts remained unchanged for decreasing porosity values, the implicit modeling of porosity could continue. Two porosity samples are considered: the default n = 16% value and the denser n = 8% sample.

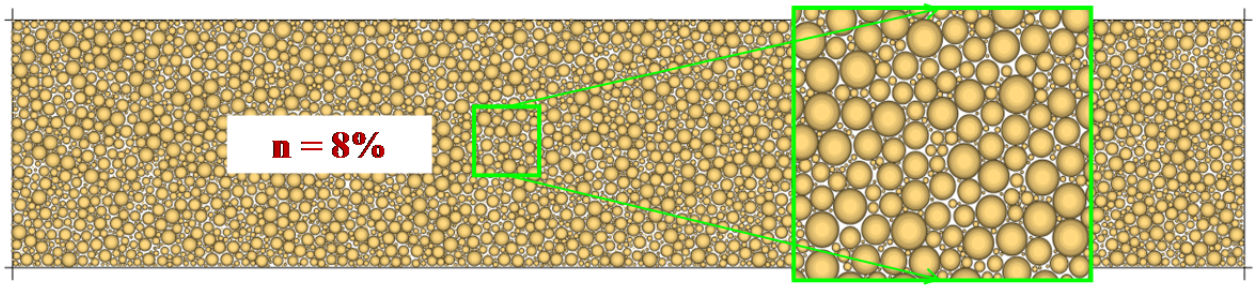


**(a)**

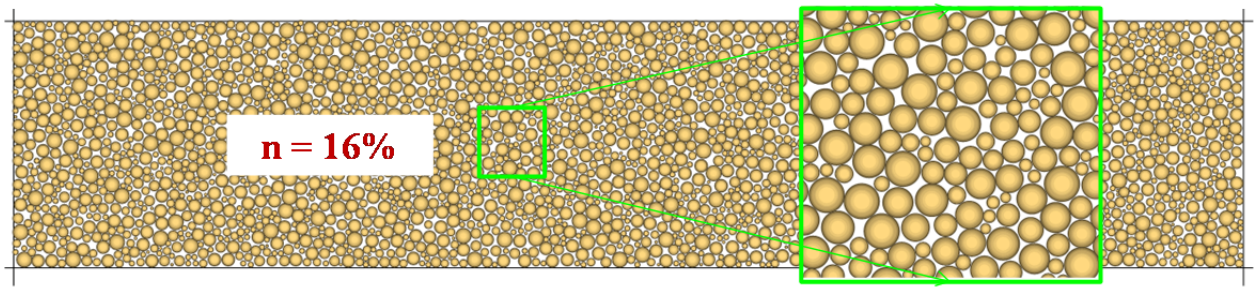


**(b)**

**Figure 4.11** Particle arrangement of DEM rocks with (a) porosity n=8% and (b) porosity n=16%

The current hypothesis to be tested is that explicit modeling of porosity is unnecessary if relevant macroproperties are incorporated. The macroproperties to be obtained are yielded from the UCS test, i.e., uniaxial strength and Young's modulus, which are the most critical

characteristics to be matched between rock samples with different porosities. Also, these properties can be related directly to rock cutting results, thus, scratching tests are performed to the samples after calibrated in order to validate the macromechanical results.

For the DEM models, a basic parameter set was first constructed based on the published Vosges sandstone data. The model was first built for Vosges sandstone because of the extensive data available, but was then extended to consider porosity effects. The base two-dimensional input for the various particle and bond parameters were originally selected to match the properties of Vosges sandstone Besuelle et al. [49]. The properties for the sample with a porosity of n=8% are as follows: (1) rock particle density, $\rho$=2630 $kg/m^3$; (2) Young's modulus of particle and parallel bond were set to the same value of 1$GPa$; (3) minimum particle radius, $R_{min}$=0.05 $mm$, and the maximum to minimum particle radius ratio was set at 3.5; (4) particle surface friction coefficient, $\mu$=0.5; and (5) the mean normal and shear bond strength were set at 10$MPa$ and 20$MPa$, respectively. Furthermore, both the normal and shear bond strength were assumed to follow a Gaussian distribution with a coefficient of variation of 23%. The ratio of normal to shear stiffness of both particles and bonds were set equal to one.

The microproperties of the sample with porosity n=16% were modified as follows: Young's modulus of particle and bond were both increased to 1.7$GPa$; the mean normal and shear bond strength were increased to 22$MPa$ and 44$MPa$, respectively. These modifications produced similar macroproperties based on the average of the results of three samples (each sample with different particle arrangement).

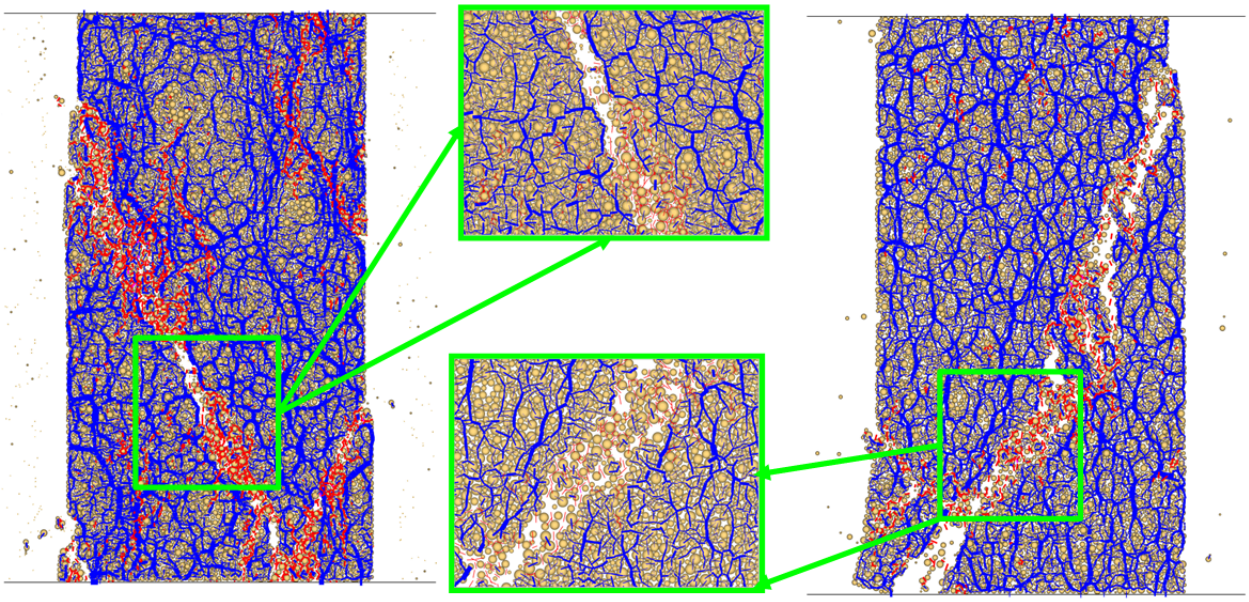

**Figure 4.12** UCS failure configuration for DEM rocks with the same macroproperties but with porosity n=8% on left and porosity n=16% on right

In summary, the follow results were achieved: The n=8% sample had a uniaxial strength of 37.35*MPa* and a Young's modulus of 2.95*GPa*; while the n=16 % sample had a uniaxial strength of 38.62*MPa* and a Young's modulus of 3.00*GPa*. Figure 4.12 shows the failure patterns and some corresponding details for the n=8% sample on the left and n = 16% on the right. The stress-strain curves of the samples shown above are given in Figure 4.13. These curves are nearly identical with respect to the slope of the elastic region and the yield strength.

These results support the hypothesis; however, these models have to be investigated further by means of a different mechanical process. The RST has been chosen to display the ability of the DEM model to produce equivalent results from samples with different porosities.

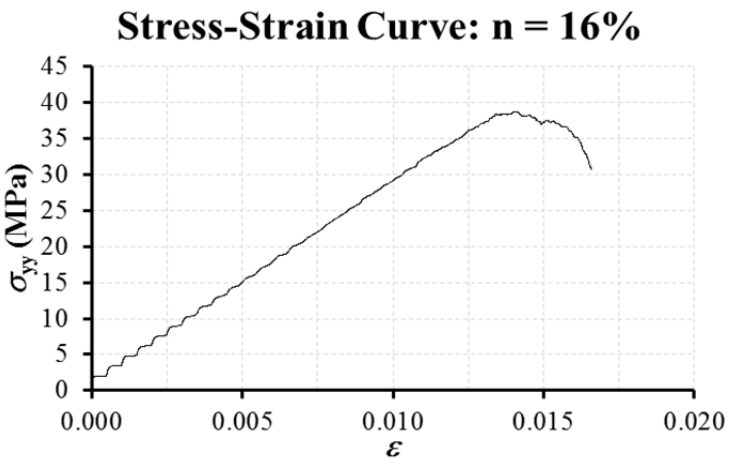


**(a)**

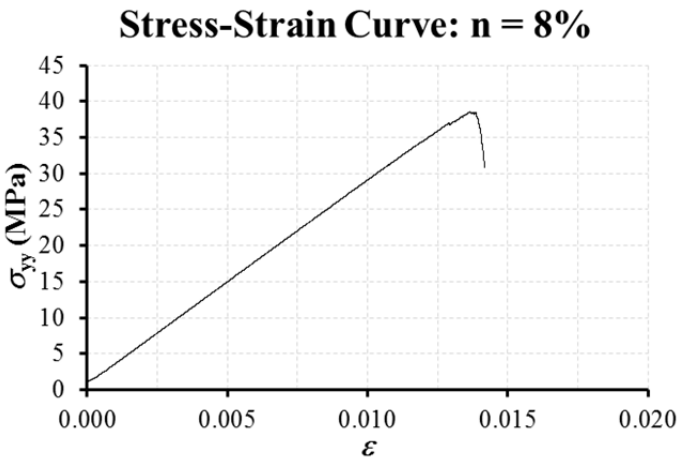


**(b)**

**Figure 4.13** Stress-Strain curves for DEM rocks with the same macroproperties but with (a) porosity n=16% and (b) porosity n=8%

RST has been shown to be useful not only for rock cutting research, but also as a quick method of obtaining the uniaxial compression of rocks. From the perspective of analysis, the numerical modeling of the test is a challenging task: a model needs to capture the fracture and fragmentation evolution during a scratching test in which a cutter continues to push against the rock. The discrete element method has a distinct advantage in that the failure process can be

automatically captured without any *a priori* setting. It has been shown previously that DEM is capable of reproducing two failure modes [50]: a plastic flow type of failure for a shallow cut and a brittle fracture type of failure for a deep cut. The current study focuses only on shallow cuts in which the specific energy of cutting has been found to be a constant for slab cutting and its value is proportional to the uniaxial strength.

Shallow cuts were simulated by setting the cutting depth to 0.4mm. Snap shots of the cutting in progress in both samples, n=8% and n=16%, are shown in Figure 4.14 along with the corresponding resulting cutting forces. The most critical aspects of the cutting process to be considered for modeling are capturing the specific energy and correct failure modes. The average forces for the two cases were about the same as reflected in the computed specific energy. For the case with n=8%, the specific energy was found to be 40.24*MPa*, and for the case with n=16% 38.71*MPa*. A visual inspection shows slight differences in the failure pattern: the denser sample shows more fractures propagating towards the middle of the sample, but the differences are deemed insignificant.

The results of the UCS test and the RST are consistent for the samples with different porosities; however, the influence of microproperty modification on other mechanical responses, such as tensile strength, has yet to be investigated. Both samples were tested and it was found that the sample with the lower porosity of 8% produced a tensile strength of $\sigma_t$=4.87*MPa* while the higher porosity value sample produced a tensile strength of $\sigma_t$=7.26*MPa.* This observed disparity suggested further investigation was required to completely simulate results from the different porosity rock samples. A study by Schöpfer et al. [36] provided insight for the possibility of balancing the influence of the microproperties based on what the investigators

termed ‘pre-existing cracks’. This concept is investigated further in the follow section, **INCLUSION OF SIMULATED MICRODEFECTS**.

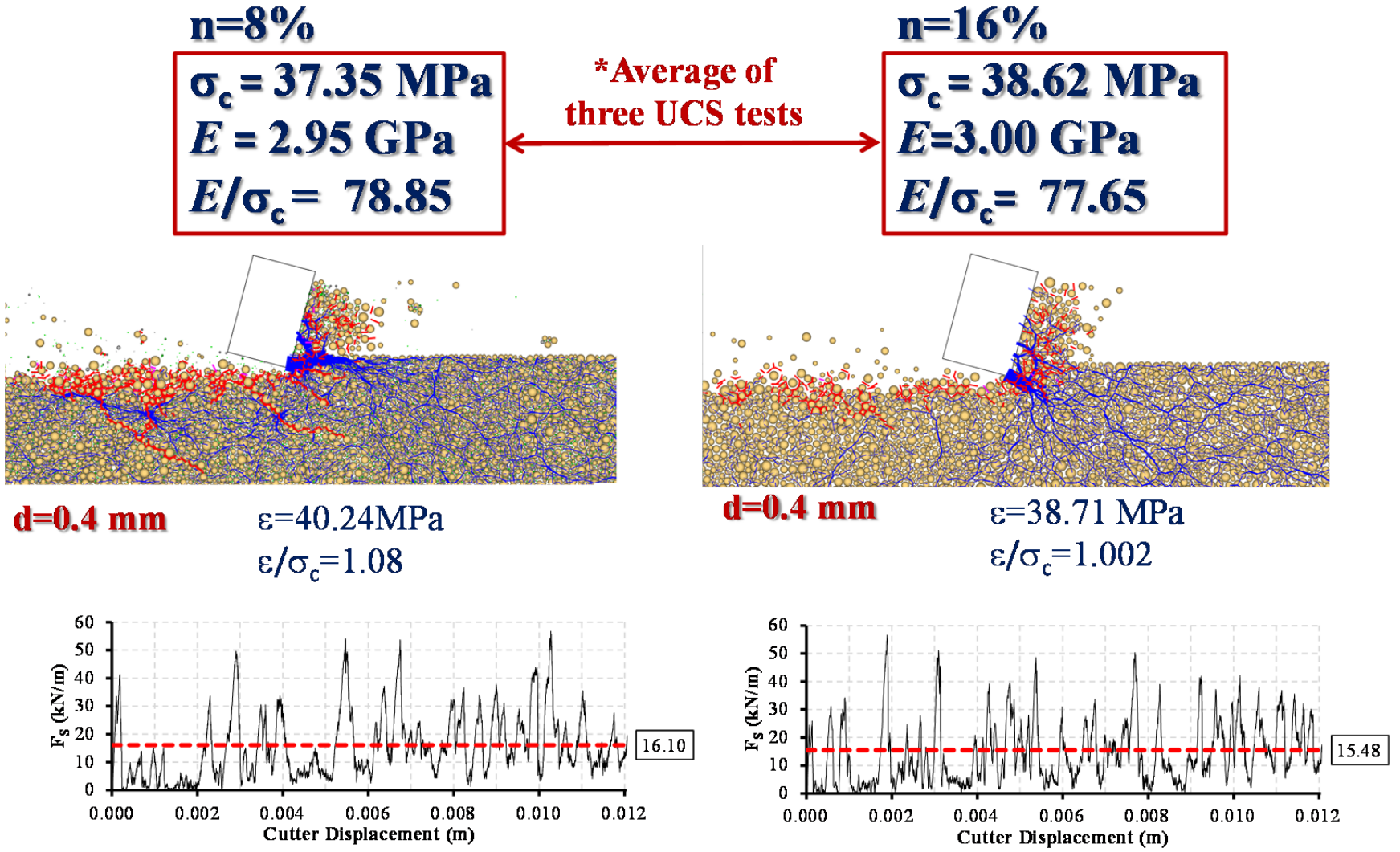


**Figure 4.14** RST result for samples with different porosities but matching macroproperties

## 4.3 INCLUSION OF SIMULATED MICRODEFECTS

When a DEM model of a rock is created in PFC2D, all existing contacts between particles are bonded together, and specifically in this case, using the parallel bond model. Therefore, the initial structure of the rock is entirely intact. In this section, the influence of unbonded contacts will be explored. In order to investigate contacts, microdefects will be randomly created through the sample proportionately to the initial number of contacts. For example, if a sample originally contains 1000 parallel bonds and it is intended to introduce 10% microdefects into this structure, the final number of parallel bonds present will be 900. The microdefects is simulated by breaking the parallel bonds by setting the bond strength equal to zero and the randomness of this operation is controlled by the use of a random number generator.

As discussed in the previous section, the impact of changing the microproperties to match the macroproperties of samples with two porosities was reflected through the tensile strength. The necessity of using microdefects to adjust for differences between the macroproperties calculated at different porosities will now be discussed.

First, the fact that the bond normal strength is higher on the n=16% sample (22*MPa*, compared to 10*MPa* of n=8%) provides an explanation for the larger tensile strength, however, the uniaxial strength, which is also related to the normal strength also increases. This phenomena can be explained by considering particle interlocking. The lower porosity sample with n=8% contains more particle interlocking than the n=16% sample, which results in a more compact structure for transferring compressive forces (Refer to the detailed areas of Figure 4.12). Thus, the hypothesis is that if a balance can be achieved from the particle interlocking of the denser

sample and the microdefects required to cancel the effects created by the excess of the bond normal strength between samples, then the resulting model calibration would be more robust.

The following method is used to investigate the effect of microdefects in the samples and its influence in porosity. Four samples were created with varying porosities (n=8%, n= 10%, n=12% and n=16%), but with identical microproperties. Then, Unconfined Compressive Strength and Direct Tension tests were performed to three different samples per porosity value and varying the amount of microdefects present. It was decided to create samples with 10%, 20%, 30%, 40% and 50% microdefects to validate results with the those obtained by Schöpfer et al. in their three-dimensional study. Moreover, pilot tests were carried out in order to verify whether it was necessary to increase the size of the sample due to the creation of these defects. The sample size was increased by the same amount that the amount of microdefects required, and it was found that the original sample had enough particles (around 8,500 particles, and around 17,500 parallel bonds) to capture the macromechanical behavior of the model.

Figure 4.15 and Figure 4.16 show the results obtained from both tests, UCS and Direct Tension (T). The results were normalized for each property and plotted accordingly to compare both raw and normalized data. The normalized parameters are identified by a superscript asterisk. From these plots the observations can be made and conclusions drawn. The UCS tends to follow the same parallel trend when microdefects are present, regardless of the porosity. This trend is also true for the Young's modulus. These two observations can be corroborated by the normalized plot of the $E$ to $\sigma_c$ ratio.

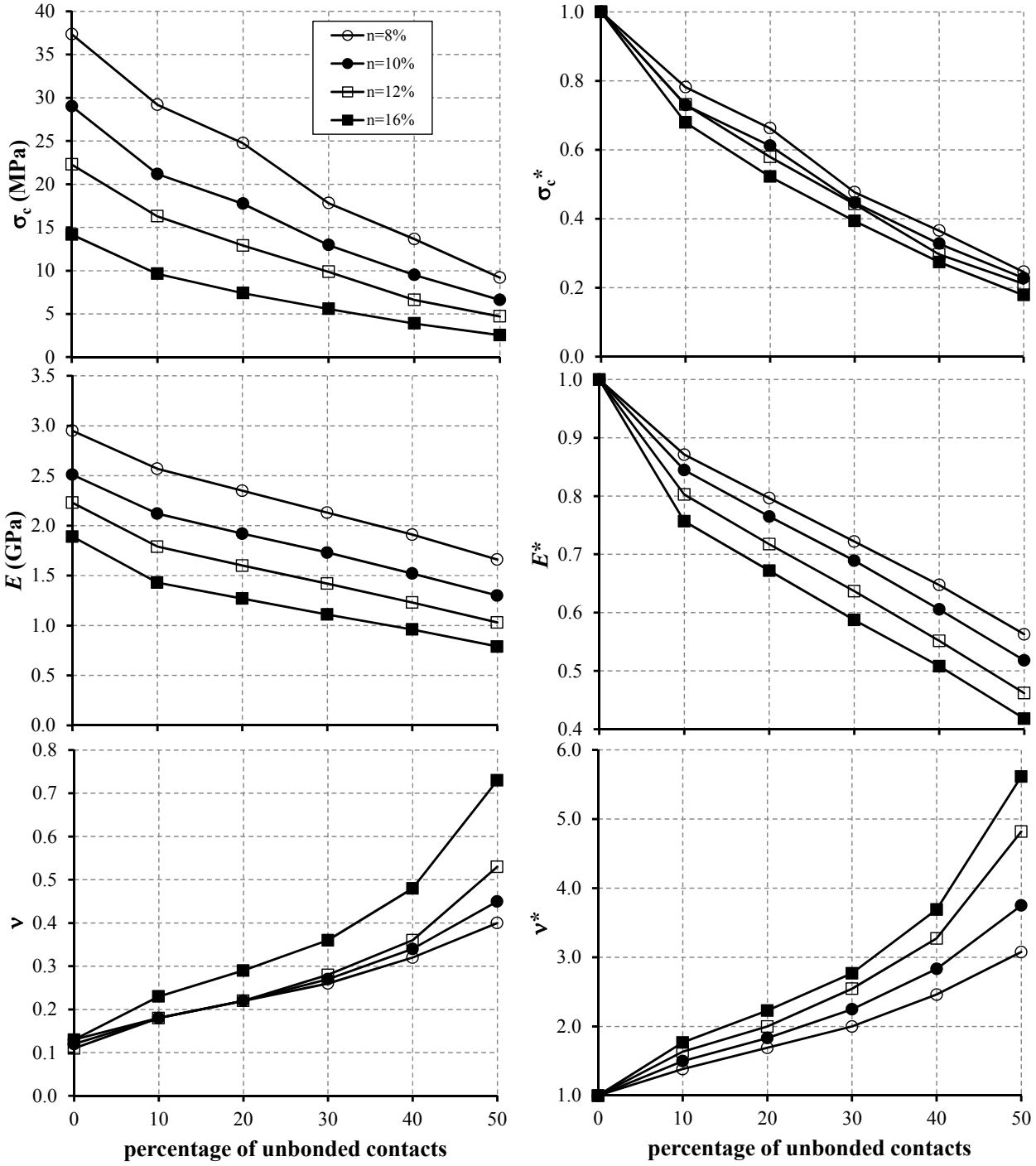


**Figure 4.15** Influence of porosity and existing microdefects on mechanical properties (UCS, Young's Modulus and Poisson's ratio)

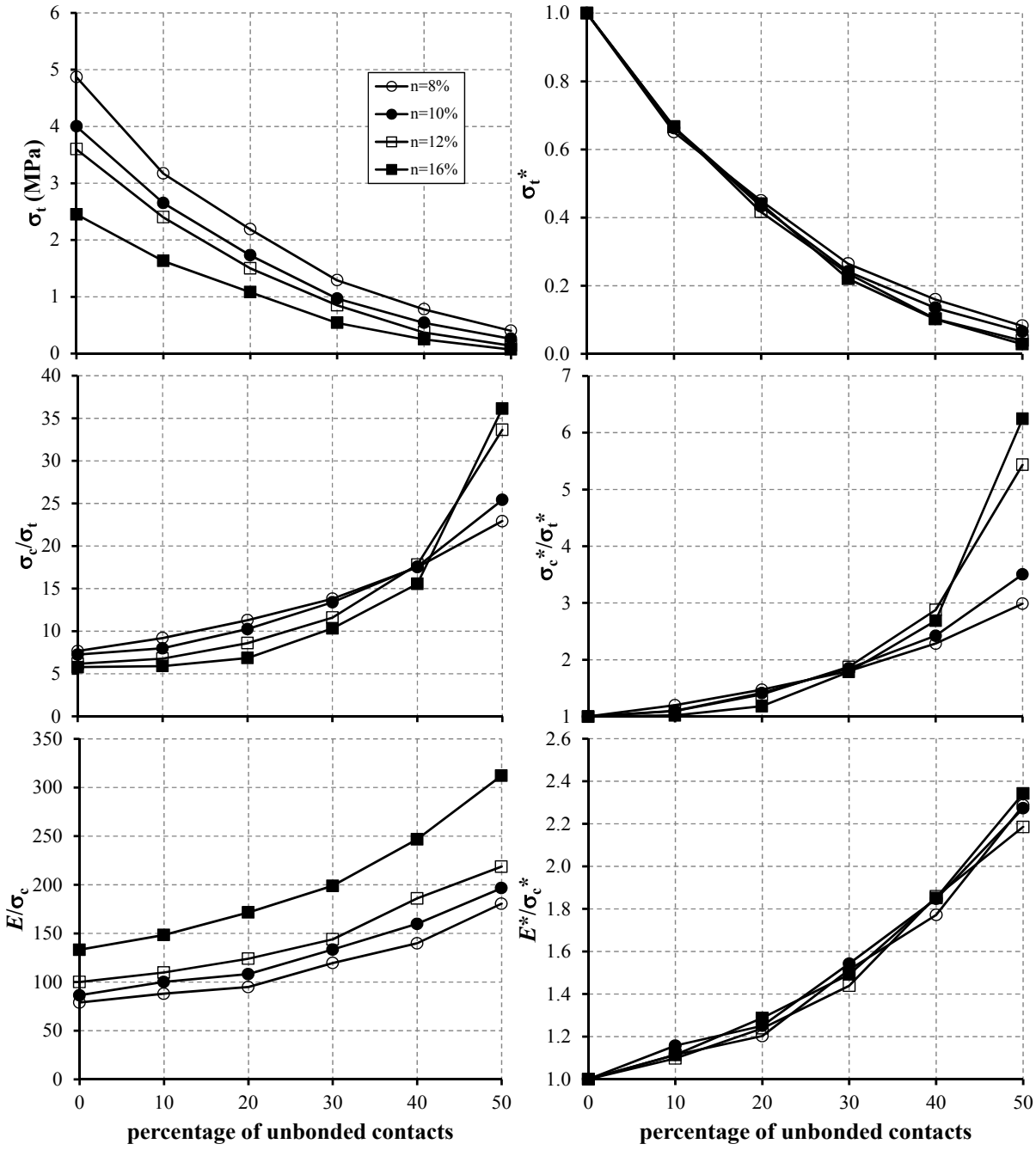


**Figure 4.16** Influence of porosity and existing microdefects on mechanical properties (Tensile Strength, UCS/T ratio and Young's modulus to UCS ratio)

The normalized tensile strength shows a mild widening when the percentage of unbonded contacts exceeds 20%. This widening is amplified in the plot of $\sigma_c/\sigma_t$ ratio, where the influence

of microdefects on the cases of higher porosities, namely n=12% and n=16%, is very significant. Finally, the implications of the $\sigma_c/\sigma_t$ ratio plot must be considered. It is well known, and widely accepted, that this ratio for rocks is close to 10. It can be seen that for the n=8% case, the $\sigma_c/\sigma_t$ ratio is close to 10. However, the n=16% case requires close to 25% microdefects in order to achieve the same ratio. Obtaining realistic values of this ration has been the focus of several previous investigations leading to the development of new contact models such as the Grain Boundary Model [12] and its derivation, the Flat Joint Bonded Particle Model [8]. The lack of reproduction of the $\sigma_c/\sigma_t$ ratio using the Parallel Bond Model has traditionally been considered a substantial drawback. However, this study brings the capabilities of this model to a different and more robust level.

### 4.3.1 Validation with 3D Results

As previously stated, the results obtained for the highest and lowest porosities from the previous analysis (***Microdefects influence on porosity***) were compared to the 3D results obtained by Schöpfer et al., which also focused on the highest and lowest porosity cases. As the rock simulated in the three-dimensional study has very high strength and stiffness, normalization of its macroproperties was necessary in order to compare them the two-dimensional results.

The macromechanical results of the 2D and 3D cases were plotted together and are shown in Figure 4.17. The most noticeable difference occurs for the tensile strength results, where a contradictory trend is observed. While the 2D results of the two different porosities flare out when the microdefects increase, the 3D results show the opposite behavior. The unconfined compressive strength, conversely, tends to keep a parallel trend regardless of whether or not the results are 2D or 3D, which shows an implicit indifference to porosity and microdefects.

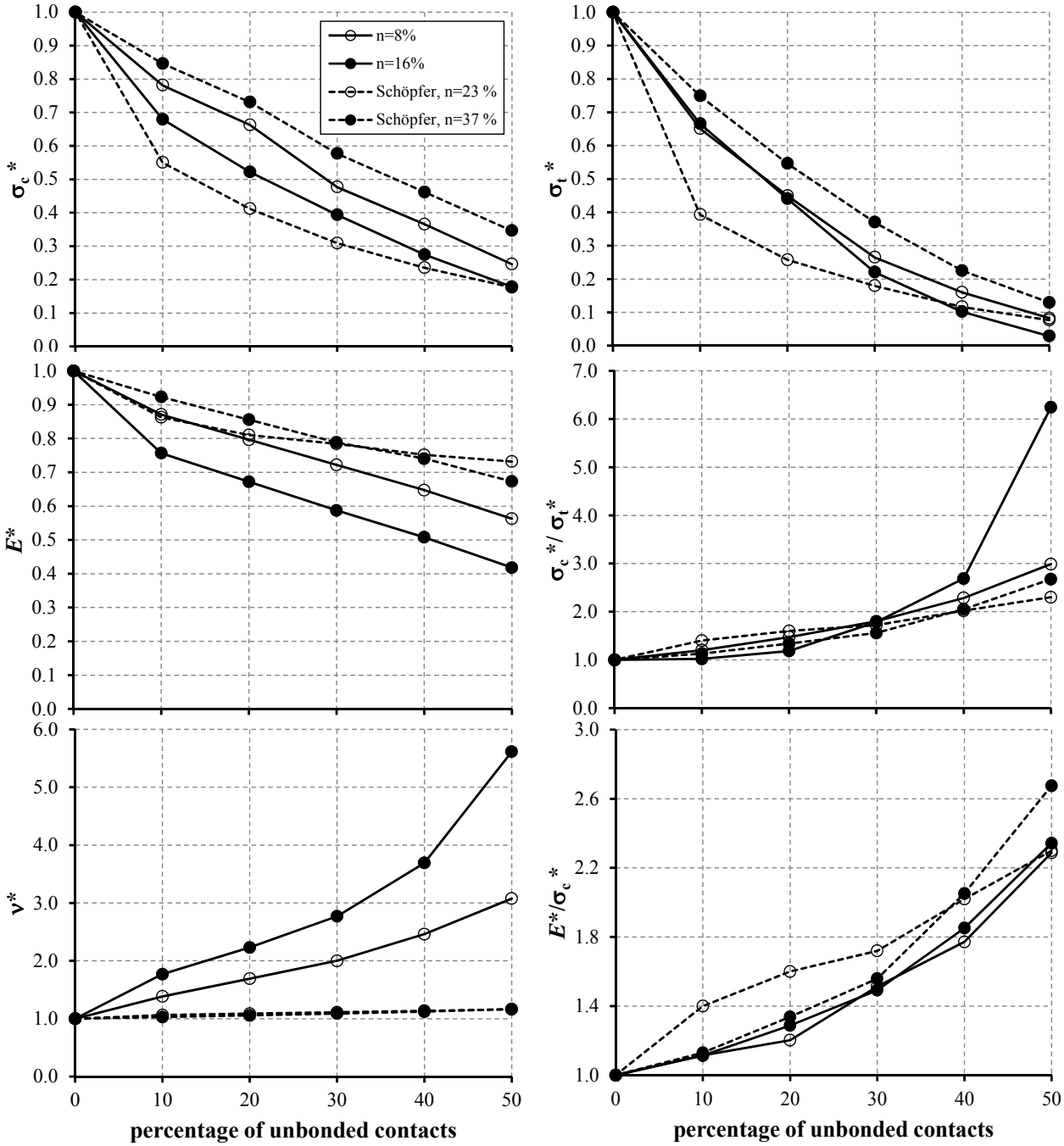


**Figure 4.17** Influence of porosity and existing microdefects on mechanical properties (Tensile strength, UCS to Tensile Strength Ratio and Modulus Ratio) for two and three-dimensional analyses

Once normalized, parallels could be drawn between the 2D and 3D analyses regarding porosity. Despite efforts to decrease porosity of the 3D model, the value is still considered to be

too high compared to the porosity results obtained in the 2D counterpart. Because of this inability to exactly match results, recreating the shape, rather than the values produced, of this trend became the focus of this study. Figure 4.18 below shows that the 2D and 3D results agree very well on every macroproperty except the Poisson's ratio. The Poisson's ratio tended to be extremely dependent on the porosity when is analyzed in the 2D environment.

From the comparison of the porosity between both 2D and 3D models, the following trends can be established. A sample with 16% porosity on the PFC2D is comparable with a sample having 37% porosity on the PFC3D. These values are the porosities that are obtained, in general, when a sample is created using ***The procedure of Potyondy and Cundall***. When the porosity is decreased by half, that is n=8% and n=23% for the 2D and 3D models, respectively, the similarities of the results are preserved.

The comparison of the results of this 2D study and Schöpfer et al.'s 3D studies performed on this section validate that the values obtained in this 2D analysis are comparable to the trends observed in the 3D analysis. The prior statement suggests that the PFC2D, which can be seen as more simplistic and less expensive modeling method, has abilities that should not be overlooked. Furthermore, this proves that the PFC2D is more than capable of capturing complicated micro and macromechanical behavior similar to the PFC3D, showing the remaining potential that this model possesses.

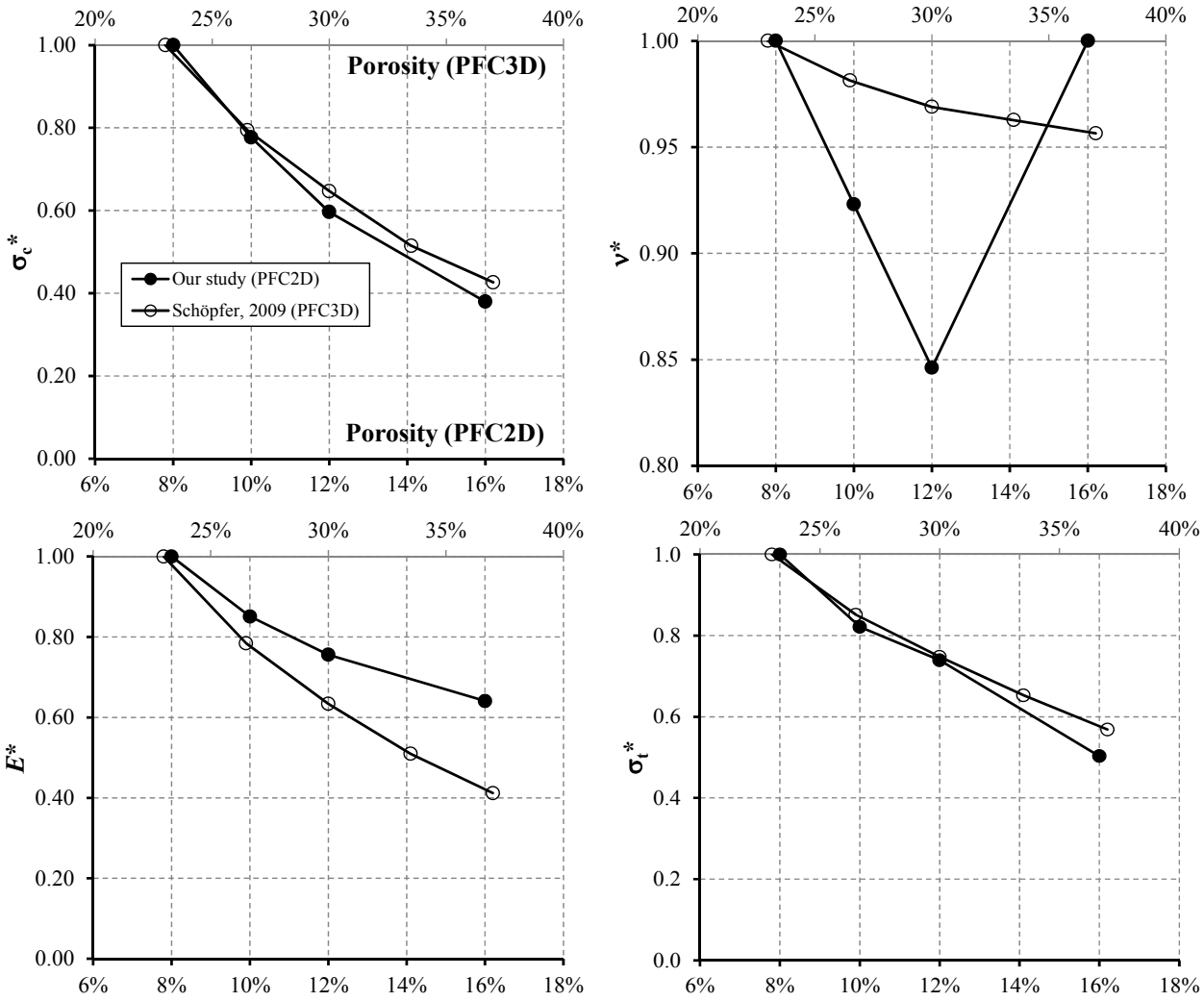


**Figure 4.18** Parallel of macroproperties for the two-dimensional and three-dimensional porosities

### 4.3.2 Optimization of Microdefects Percentage

After developing a better understanding of the influence of the microdefects on the mechanical responses of the DEM model, it was deemed necessary to evaluate whether the observed trends were repeatable for samples of different microproperties and porosities, but similar

macroproperties, i.e., the samples analyzed in the section **IMPLICIT MODEL BASED ON VARYING MICROPROPERTIES.**

The same testing procedure was given to the n=16% and n=8% samples regarding microdefects. The UCS and Direct tension tests were performed following the same protocol that has been followed during this study, that is, three samples each with different particle configuration per material. The results obtained are plotted in Figure 4.19.

From Figure 4.19, it can be seen that intact samples produce largely similar values of UCS, Young's Modulus and Poisson's ratio; however, the tensile strength values vary significantly. Also, the trends correspond to those previously observed. Furthermore, the $\sigma_c/\sigma_t$ ratio again requires attention. It can be observed that the exact same tendency is reproduced in these results regarding the n=16% sample, and its $\sigma_c/\sigma_t$ ratio. When the sample possesses microdefects between 20% and 30% the UCS to tensile strength ratio is close to 10. This provides additional verification to the previously observed relationship between the tensile strength ratio and microdefects. The results of the n=8% sample were already discussed, and it was recognized that when the sample contains 10% microdefects, the $\sigma_c/\sigma_t$ ratio is also near 10.

Based on these results, it is postulated that the granular interlocking generated as a secondary effect of decreasing the porosity can be counterbalanced by finding optimal values of microdefects for the different porosities. Because this study primarily focuses on samples of n=16% and n=8%, the following effort will be concentrated on matching the macroproperties of the samples with these porosities not only by varying the microproperties, but also by implementing microdefects.

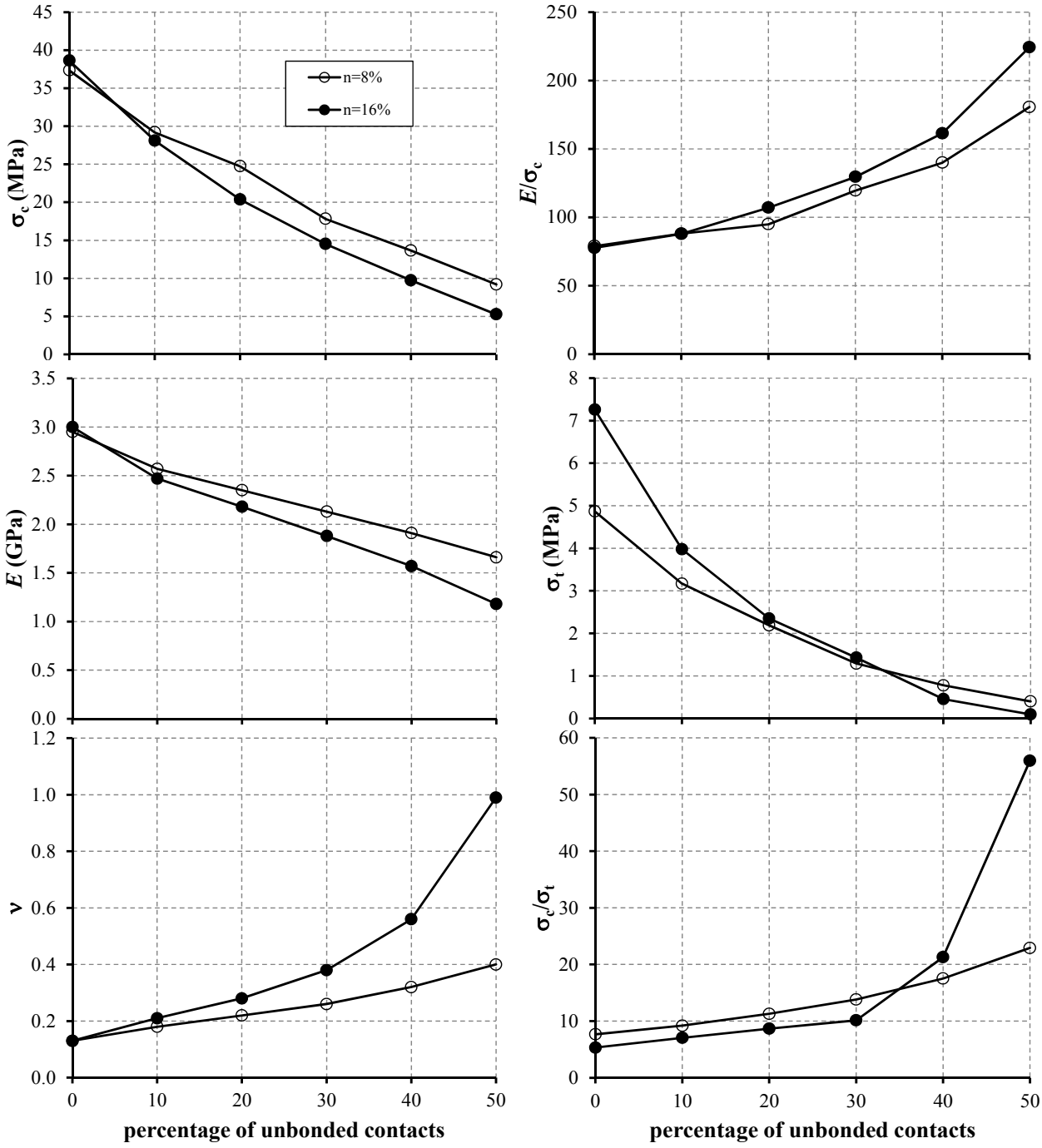


**Figure 4.19** Influence of porosity and existing microdefects on mechanical properties: Case study of samples with different porosities but matching macroproperties when intact

## 4.4 MODEL CALIBRATION INCORPORATING OPTIMAL MICRODEFECTS

For the two sample porosities of this case study, namely, n=16% and n=8%, the new calibration procedure including not only varying microproperties but also the implementation of the microdefects is described in this section. One goal of this study is to create samples with a $\sigma_c/\sigma_t$ ratio close to 10, considered typical of expected rock behavior. To support this idea, a recent investigation completed in South Africa completed uniaxial and tensile strength testing for 46 different types of rock (14 igneous, 15 metamorphic and 17 sedimentary). Figure 4.20 shows the plotted results with rock types differentiated. It can also be seen from this data that a $\sigma_c/\sigma_t$ ratio 10.619 was found to best fit the data utilizing a linear regression model.

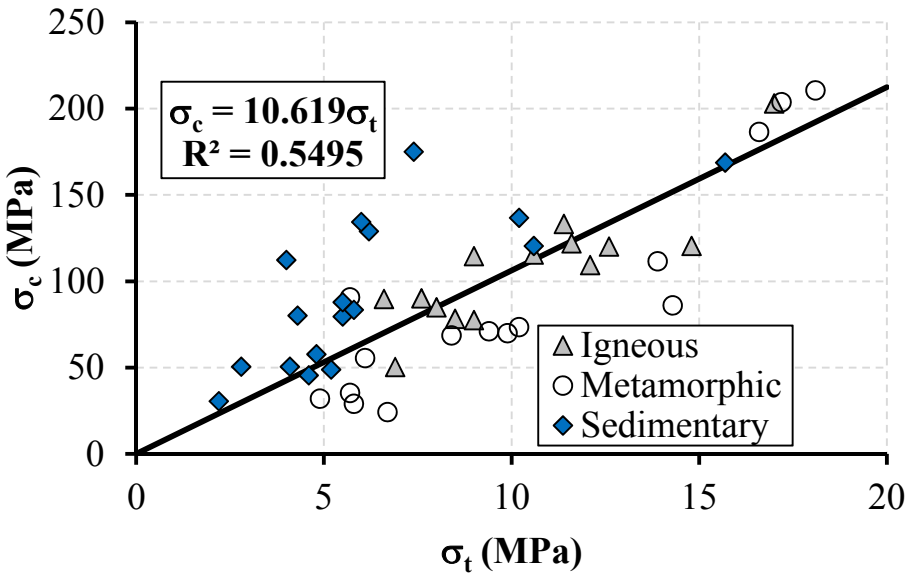


**Figure 4.20** Mechanical response of a suite of rocks [4]

In order to achieve the desired ratio for the rock samples, the optimal microdefects percentages for each level of porosity, namely 10% microdefects for n=8% and 25% microdefects for n=16% were used based on the results obtained in the previous section.

The microproperties for the n=8% case remained unmodified from the previous studies, however, the n=16% case varied from previous results. The microproperties that yielded similar results based on the UCS, Direct Tension, and RST are given in Table 4.3 below. The previous calibration, **IMPLICIT MODEL BASED ON VARYING MICROPROPERTIES**, only varied the microproperties. When the current calibration attempt is compared to the previous effort, the largest discrepancy occurs between the bond strengths, as expected, and differs by approximately 50% of its original strength.

**Table 4.3** PFC2D microproperties of the calibrated model for the samples with n=8% and n=16% porosities with 10% and 25% of microdefects, respectively

| GRAINS (PARTICLES) | CEMENT (PARALLEL BONDS) |
|---|---|
| $\boldsymbol{\rho = 2630\ kg/m^3}$<br>$\boldsymbol{E_c = \begin{cases} 1\ GPa - \ n = 8\% \\ 1.8\ GPa - \ n = 16\% \end{cases}}$<br>$\boldsymbol{R_{max}/R_{min} = 3.5}$<br>$\boldsymbol{R_{min} = 0.2 \times 10^{-3}\ m}$<br>$\boldsymbol{k_n/k_s = 1\ \therefore\ k_n = 2tE_c\ , t = 1}$<br>$\boldsymbol{\mu = 0.5}$<br><br>**Where,**<br>$\boldsymbol{\rho}$ : Density<br>$\boldsymbol{n}$ : Porosity<br>$\boldsymbol{R_{max}}$ , $\boldsymbol{R_{min}}$ : Maximum and minimum radius, respectively<br>$\boldsymbol{E_c}$ : Young sModulus<br>$\boldsymbol{k_n}$ : Normal Stiffness<br>$\boldsymbol{k_s}$ : Shear Stiffness<br>$\boldsymbol{\mu}$ : Friction | $\boldsymbol{\bar{\lambda} = 1}$<br>$\boldsymbol{\bar{R} = \bar{\lambda} \times min(R^{(A)}, R^{(B)})}$<br>$\boldsymbol{\bar{E}_c = \begin{cases} 1\ GPa - \ n = 8\% \\ 1.8\ GPa - \ n = 16\% \end{cases}}$<br>$\boldsymbol{\bar{k}^n/\bar{k}^s = 1\ \therefore\ \bar{k}^n = \bar{E}_c/(R^{(A)} + R^{(B)})}$<br>$\boldsymbol{\bar{\sigma}_c = 0.5\bar{\tau}_c = (mean \pm std.dev.)}$<br>$\boldsymbol{\therefore\ mean = \begin{cases} 10\ MPa - \ n = 8\% \\ 32\ MPa - \ n = 16\% \end{cases}\ ;\ std.dev. = 23\%}$<br><br>**Where,**<br>$\boldsymbol{\bar{\lambda}}$ : Bond Radius Multiplier<br>$\boldsymbol{\bar{R}}$ : Bond Radius<br>$\boldsymbol{R^{(A)}, R^{(B)}}$: Radius of particle in contact A and B, respectively<br>$\boldsymbol{\bar{E}_c}$ : Young's Modulus<br>$\boldsymbol{\bar{k}^n}$ : Normal Stiffnes<br>$\boldsymbol{\bar{k}^s}$ : Shear Stiffnes<br>$\boldsymbol{\bar{\sigma}_c}$ : Normal Strength<br>$\boldsymbol{\bar{\tau}_c}$ : Shear Strength |

The Uniaxial Compression Strength test yielded results very similar to those observed for the first calibration effort. The macrocracks which developed at the end of the test are depicted in

Figure 4.21. In this figure, it can be seen that the cracking density on the n=8% case is larger than on the n=16% case; however, this is a misleading observation created by the relatively larger quantity of bonds on the rock sample containing lower porosity. This effect is also apparent in the chain of forces. The coalescence of these cracks show similar failure patterns from a macroscopic point of view, as shown in the details of the figure.

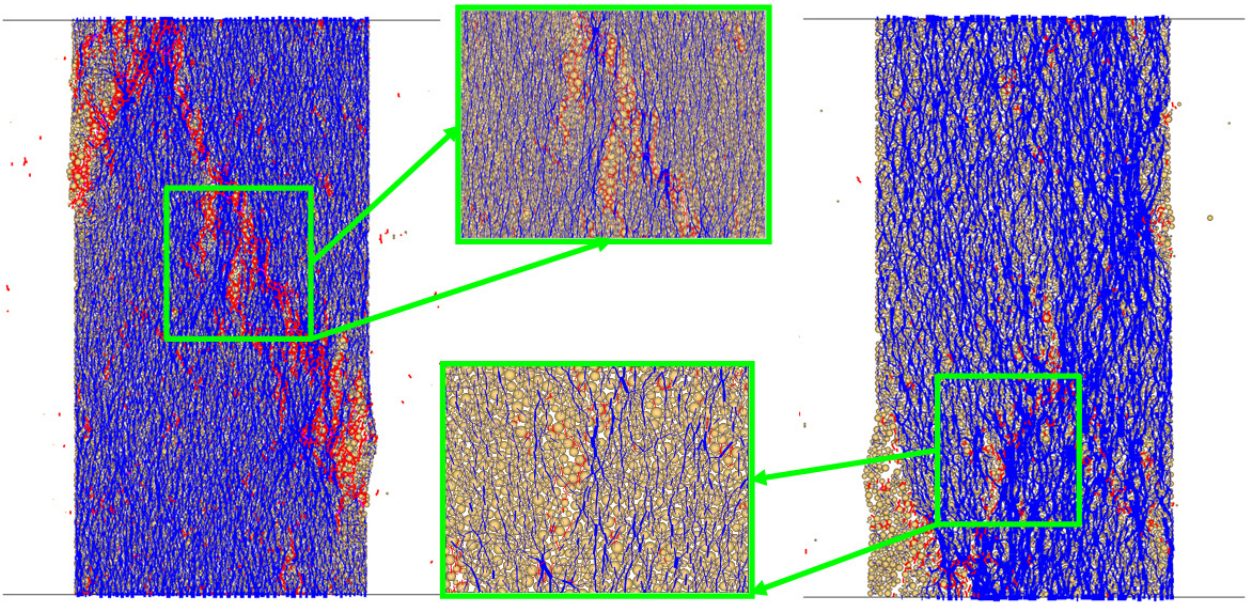

**Figure 4.21** DEM Unconfined Compressive Strength failure patterns of a porosity n=8% sample on the left and a porosity n=16% sample on the right

The Young's modulus values and peak strengths match very well in both cases. For example, Figure 4.22 shows the stress-strain curves that correspond to the failed samples above (Figure 4.21). Averaging three samples revealed an Unconfined Compressive Strength of $\sigma_c$=29.19*MPa*, and Young's Modulus of $E$=2.57*GPa* for the samples with porosity n=8% while the sample with twice this porosity, yielded values of Unconfined Compressive Strength

$\sigma_c$=27.31*MPa*, and the Young's Modulus of *E*=2.56*GPa*. These values are considered to have matched very well considering the inherent high variability of uniaxial strength.

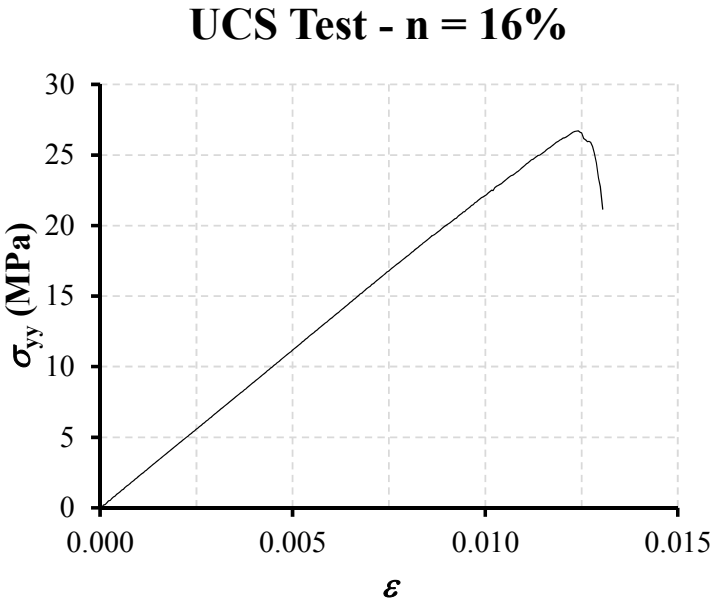


**(a)**

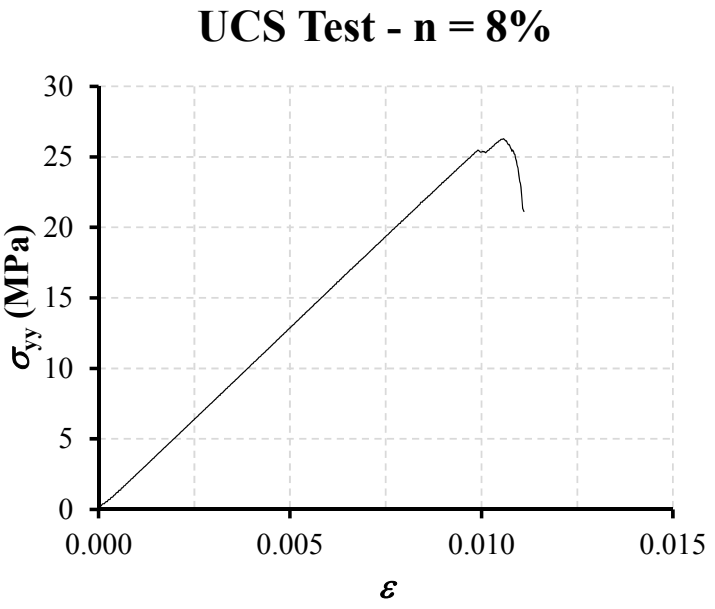


**(b)**

**Figure 4.22** Stress-Strain Curves of UCS test on samples with (a) porosity n=16% and (b) porosity n=8%

Results from the Direct Tension tests performed also matched well with expected failure patterns as illustrated by specific examples in both Figure 4.23 and Figure 4.23 below. However, the stress-strain curves showed that while the peak values matched well, the trend of the curves differed. The peak of the lower porosity sample occurred close to vertical strain $\varepsilon$=0.0028 while the peak of the higher porosity sample occurred closer to a vertical strain of $\varepsilon$=0.0045.

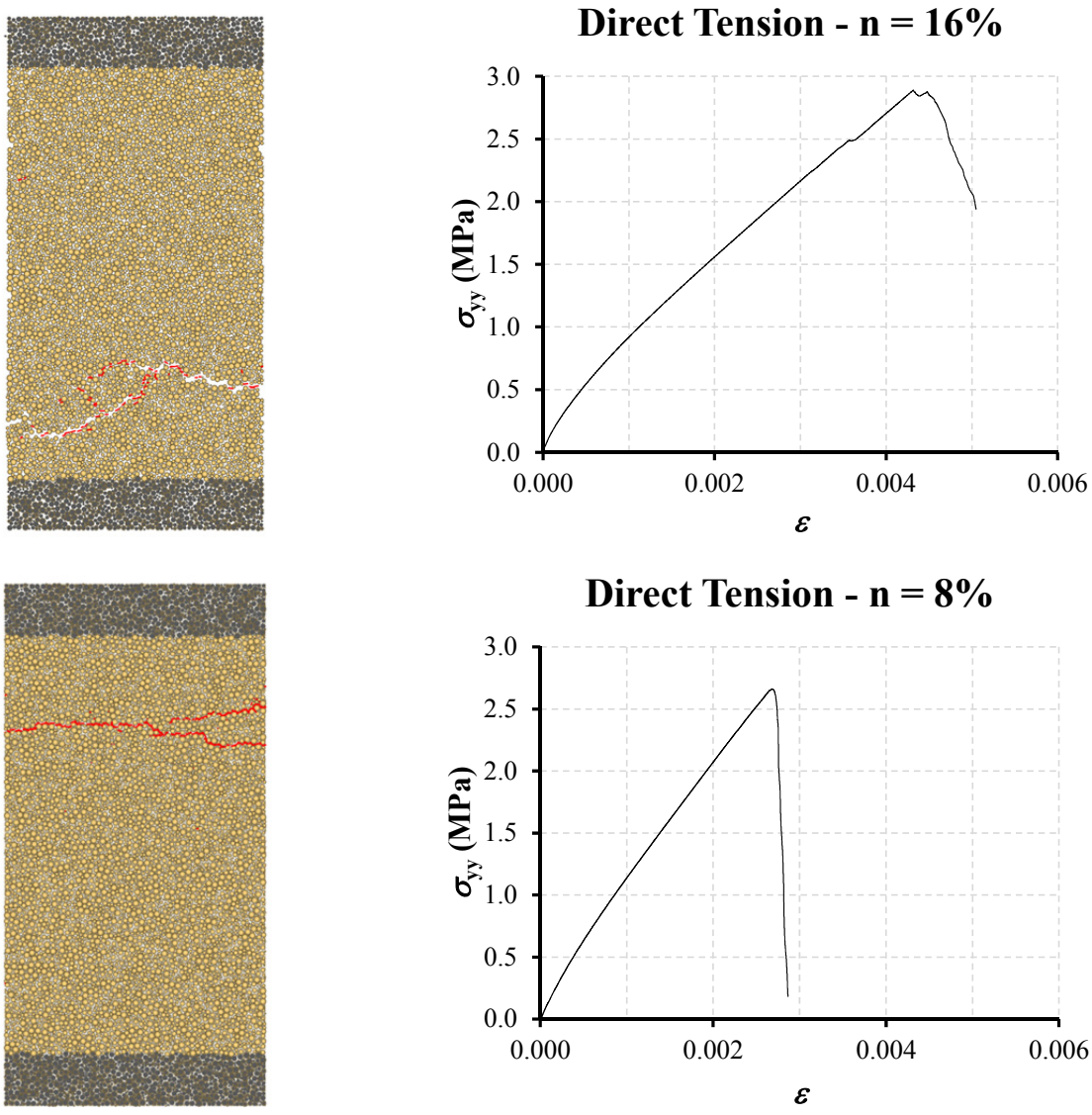


**Figure 4.23** Failure and stress-strain curve of the Direct Tension Test on a sample with porosity n=16% (top) and n=8% (bottom) where the gray particles denote grips used during sample testing

The tensile elastic moduli differ significantly. The region of elasticity of the sample is known to occur at extremely small strain values when the sample is considered to be intact. However, due to the necessary implementation of microdefects in the samples, the higher porosity rock sample may show earlier failure because its particulate matrix contains more microdefects. Therefore, the loss of stiffness is more apparent for the higher porosity sample.

To explain this tendency, first, only the elastic region is more thoroughly investigated by considering the stress-strain curve from the direct tension tests. It can be seen from Figure 4.24 below that both samples produce similar results for this region of consideration. It can also be seen that there is a difference between the strain values at failure which can be attributed to the crack length. Because the coalescence of microdefects is longer for the sample with larger porosity, extra deformation is required to yield.

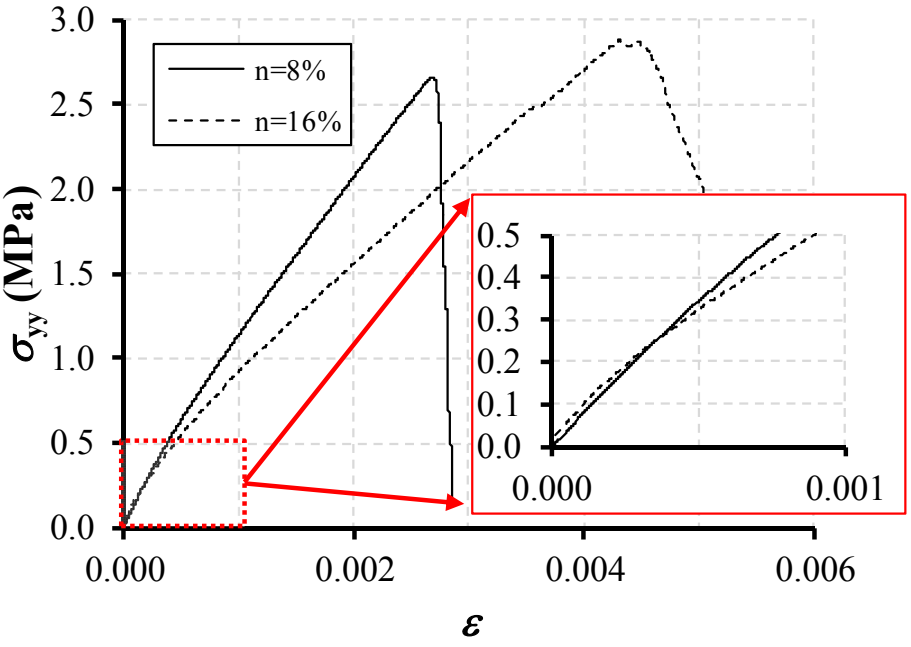


**Figure 4.24** Tensile modulus of both n=8% and n=16% for a very small strain region

This observation suggests that the samples still preserve mechanical similarities; however, the failure phenomena experience mild modification as the materials reach their strength limits. Failure considered on the micromechanical scale also showed disparities during the RST test as described in the section, **IMPLICIT MODEL BASED ON VARYING MICROPROPERTIES.** However, these differences were considered inconsequential because the critical macromechanical features were adequately captured. Three samples were averaged for the direct tension tests for each of the two porosity levels considered: n=8% and n=16% which produced $\sigma_t$=3.17*MPa* and $\sigma_t$=2.99*MPa*, respectively. Using these values, the ratio of UCS to Tensile Strength was found to be 9.21 for the n=8% sample and 9.13 for the n=16% sample.

Finally, the RST was performed to both porosity levels and the horizontal cutting forces during the cutting process were recorded and plotted. The lower porosity sample required a shallow cutting depth in order to preserve the appropriate ductile failure mode. Likewise, the higher porosity sample required a deeper cutting depth in order to ensure an adequate number of particles remained in contact in front of the cutter. The mechanical response based on the specific energy produced expected values and the failure pattern observed showed coalescence of microdefects propagating toward the sample center for both porosity cases. This tendency is displayed by Figure 4.25. To conclude, a summary of the macroproperties after calibrating the model by varying the microproperties and optimizing the microdefects is given in Table 4.4 below.

**Table 4.4** Macroproperties matched on samples with different porosities

| *Mechanical Results (Macroproperties)* | *Porosity* | |
|---|---|---|
| | ***8%*** | ***16%*** |
| **Microcraking** | *10%* | *25%* |
| **Unconfined Compressive Strentgh, $\sigma_c$ (MPa)** | 29.19 | 27.31 |
| **Young's Moudlus, *E* (GPa)** | 2.57 | 2.56 |
| **Poisson't ratio, $\nu$** | 0.13 | 0.13 |
| $E/\sigma_c$ | 88.04 | 93.74 |
| **Tensile Strength, $\sigma_t$ (MPa)** | 3.17 | 2.99 |
| $\sigma_c/\sigma_t$ | 9.21 | 9.13 |
| **Specific Energy, $\varepsilon$ (MPa)** | 30.65 | 26.17 |

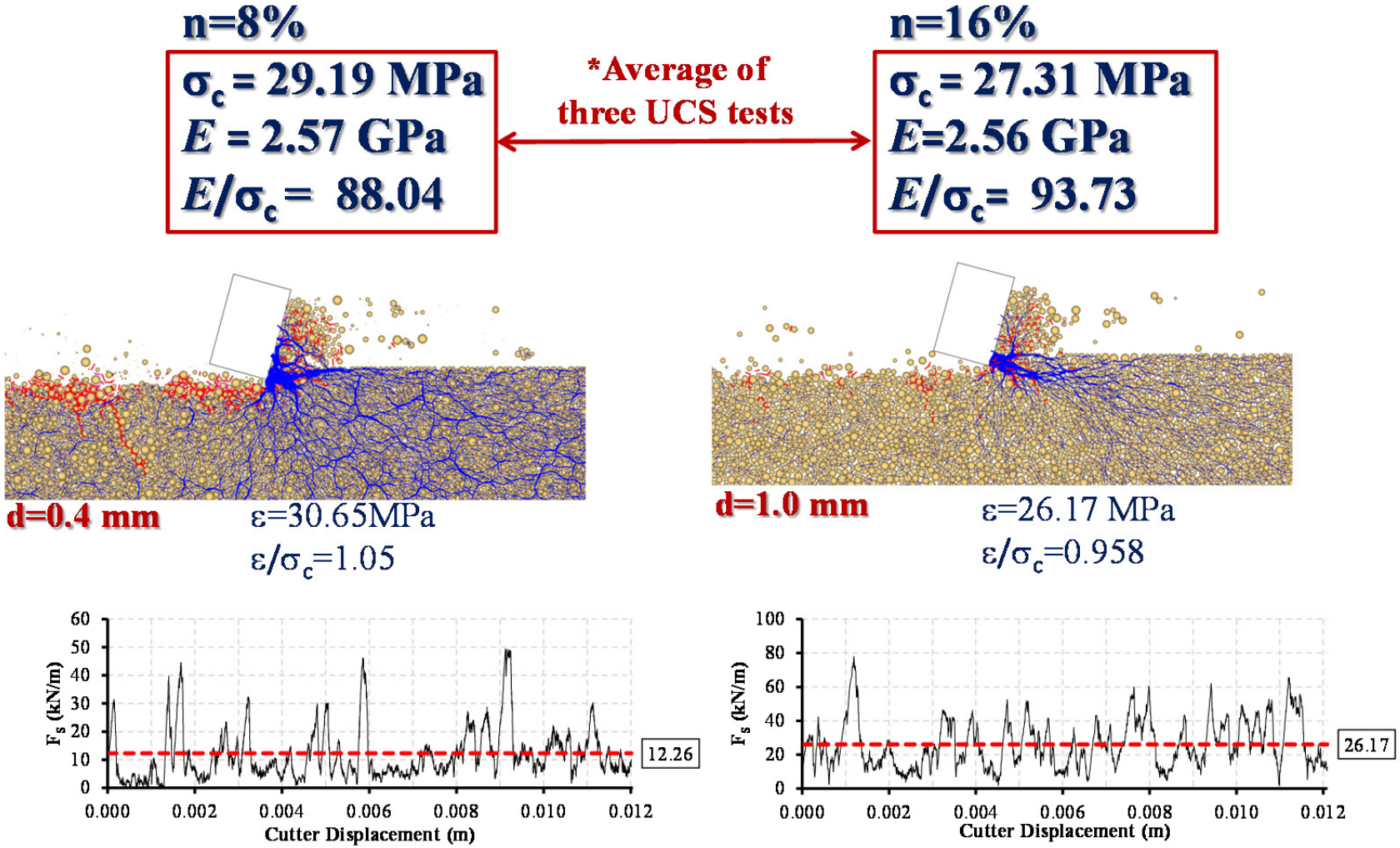


**Figure 4.25** RST result for samples with different porosities but matching macroproperties

# 5.0 SIMULATION OF THE MECHANICAL BEHAVIOR OF ROCKS UNDER HIGH PRESSURE CONFINEMENT – FOUNDATION FOR FUTURE WORK

Reproducing the rock behavior under high pressure conditions using the DEM is a challenging undertaking from the initial failure reproduction to the final mechanical response. This subject is essential to the foundation for geomechanical analyses of highly pressurized environments. Closing the gap that currently exists in accurately modeling rock behavior under high pressure conditions using DEM opens a wide range of possibilities in the numerical simulation of geophysical phenomena. This section presents some factors that have been addressed to solve this problem, and the influences shown in this simulation.

## 5.1 EFFECT OF THE INITIAL STATE OF STRESSES ON THE DEM MACROMECHANICS

During the analysis of the effects of the model on particle contact distribution produced by the in-situ sample stresses, an interesting phenomenon was observed. Despite the fact that this observation fell outside of the scope of this study, it merits consideration in future investigations utilizing pressurized environments. It was observed that the macroproperties of a material were dependent on the initial state of stresses of the sample regardless of whether or not the sample was tested with different environmental conditions.

Table 4.2 shows the created scenarios with different states of stresses where the *Isotropic* state is characterized by the equality of horizontal and vertical stresses, and the *Anisotropic* stresses present a disparity between the horizontal and vertical stresses. Naturally, two cases of the Anisotropic case can occur: *Anisotropic CASE I*, where the vertical stresses are double the horizontal stresses; and *Anisotropic CASE II*, where the vertical stresses are half the horizontal stresses. These states of stresses are achieved during sample creation.

Four different materials each with four different porosities underwent UCS tests and three samples per material were tested. The results obtained for the *Isotropic*, *Anisotropic CASE I* and *Anisotropic CASE II* are summarized in Table 5.1, Table 5.2 and Table 5.3, respectively.

**Table 5.1** Macroproperties on samples with different porosities – Isotropic Case

| | | *Material* | [1] $\sigma_c$ (MPa) | [2] $E$ (GPa) | Ratio: $E$ / $\sigma_c$ | [3] Normal Bond Strength (MPa) | [4] Particle Young's Modulus (GPa) | [1]/[3] Normalized Strength | [2]/[4] Normalized Stiffness |
|---|---|---|---|---|---|---|---|---|---|
| **ISOTROPIC** | n = 8 % | *SS_1_VIII* | 37 | 2.95 | 78.85 | 10.00 | 1.00 | 3.74 | 2.95 |
| | | *SS_2_VIII* | 42 | 4.35 | 102.74 | 12.00 | 1.50 | 3.53 | 2.90 |
| | | *SS_3_VIII* | 50 | 5.81 | 116.43 | 14.00 | 2.00 | 3.56 | 2.90 |
| | | *SS_4_VIII* | 57 | 7.19 | 125.89 | 16.00 | 2.50 | 3.57 | 2.88 |
| | n = 10 % | *SS_1_VIII* | 29 | 2.51 | 86.42 | 10.00 | 1.00 | 2.90 | 2.51 |
| | | *SS_2_VIII* | 34 | 3.69 | 110.04 | 12.00 | 1.50 | 2.79 | 2.46 |
| | | *SS_3_VIII* | 39 | 4.91 | 125.80 | 14.00 | 2.00 | 2.79 | 2.45 |
| | | *SS_4_VIII* | 47 | 6.03 | 128.91 | 16.00 | 2.50 | 2.92 | 2.41 |
| | n = 12 % | *SS_1_VIII* | 22 | 2.23 | 99.91 | 10.00 | 1.00 | 2.23 | 2.23 |
| | | *SS_2_VIII* | 27 | 3.24 | 121.56 | 12.00 | 1.50 | 2.22 | 2.16 |
| | | *SS_3_VIII* | 31 | 4.32 | 139.19 | 14.00 | 2.00 | 2.22 | 2.16 |
| | | *SS_4_VIII* | 35 | 5.23 | 150.07 | 16.00 | 2.50 | 2.18 | 2.09 |
| | n = 16 % | *SS_1_VIII* | 14 | 1.89 | 133.55 | 10.00 | 1.00 | 1.42 | 1.89 |
| | | *SS_2_VIII* | 17 | 2.70 | 156.53 | 12.00 | 1.50 | 1.44 | 1.80 |
| | | *SS_3_VIII* | 20 | 3.58 | 178.34 | 14.00 | 2.00 | 1.43 | 1.79 |
| | | *SS_4_VIII* | 23 | 4.38 | 192.72 | 16.00 | 2.50 | 1.42 | 1.75 |

**Table 5.2** Macroproperties on samples with different porosities – Anisotropic Case I

| | | *Material* | $\sigma_c$ (MPa) | $E$ (GPa) | Ratio: $E$ / $\sigma_c$ | [3] Normal Bond Strength (MPa) | [4] Particle Young's Modulus (GPa) | [1]/[3] Normalized Strength | [2]/[4] Normalized Stiffness |
|---|---|---|---|---|---|---|---|---|---|
| ANISOTROPIC: CASE I | n = 8 % | *SS_1_VIII* | 20 | 1.44 | 71.03 | 10.00 | 1.00 | 2.03 | 1.44 |
| | | *SS_2_VIII* | 22 | 2.03 | 93.65 | 12.00 | 1.50 | 1.80 | 1.35 |
| | | *SS_3_VIII* | 27 | 2.68 | 99.92 | 14.00 | 2.00 | 1.91 | 1.34 |
| | | *SS_4_VIII* | 26 | 3.29 | 125.33 | 16.00 | 2.50 | 1.64 | 1.32 |
| | n = 10 % | *SS_1_VIII* | 16 | 1.32 | 81.92 | 10.00 | 1.00 | 1.61 | 1.32 |
| | | *SS_2_VIII* | 18 | 1.85 | 104.36 | 12.00 | 1.50 | 1.48 | 1.24 |
| | | *SS_3_VIII* | 21 | 2.40 | 112.43 | 14.00 | 2.00 | 1.52 | 1.20 |
| | | *SS_4_VIII* | 24 | 2.87 | 117.36 | 16.00 | 2.50 | 1.53 | 1.15 |
| | n = 12 % | *SS_1_VIII* | 14 | 1.24 | 90.64 | 10.00 | 1.00 | 1.36 | 1.24 |
| | | *SS_2_VIII* | 16 | 1.70 | 108.52 | 12.00 | 1.50 | 1.30 | 1.13 |
| | | *SS_3_VIII* | 18 | 2.22 | 122.98 | 14.00 | 2.00 | 1.29 | 1.11 |
| | | *SS_4_VIII* | 19 | 2.64 | 139.52 | 16.00 | 2.50 | 1.18 | 1.05 |
| | n = 16 % | *SS_1_VIII* | 9 | 1.27 | 143.27 | 10.00 | 1.00 | 0.89 | 1.27 |
| | | *SS_2_VIII* | 10 | 1.71 | 176.95 | 12.00 | 1.50 | 0.81 | 1.14 |
| | | *SS_3_VIII* | 11 | 2.07 | 180.74 | 14.00 | 2.00 | 0.82 | 1.03 |
| | | *SS_4_VIII* | 13 | 2.38 | 182.25 | 16.00 | 2.50 | 0.82 | 0.95 |

**Table 5.3** Macroproperties on samples with different porosities – Anisotropic Case II

| | | *Material* | $\sigma_c$ (MPa) | $E$ (GPa) | Ratio: $E$ / $\sigma_c$ | [3] Normal Bond Strength (MPa) | [4] Particle Young's Modulus (GPa) | [1]/[3] Normalized Strength | [2]/[4] Normalized Stiffness |
|---|---|---|---|---|---|---|---|---|---|
| ANISOTROPIC: CASE II | n = 8 % | *SS_1_VIII* | 20 | 1.18 | 57.58 | 10.00 | 1.00 | 2.04 | 1.18 |
| | | *SS_2_VIII* | 20 | 1.68 | 82.47 | 12.00 | 1.50 | 1.69 | 1.12 |
| | | *SS_3_VIII* | 25 | 2.28 | 90.51 | 14.00 | 2.00 | 1.80 | 1.14 |
| | | *SS_4_VIII* | 30 | 2.81 | 93.35 | 16.00 | 2.50 | 1.88 | 1.12 |
| | n = 10 % | *SS_1_VIII* | 17 | 1.03 | 60.11 | 10.00 | 1.00 | 1.72 | 1.03 |
| | | *SS_2_VIII* | 17 | 1.48 | 85.55 | 12.00 | 1.50 | 1.44 | 0.99 |
| | | *SS_3_VIII* | 21 | 1.99 | 96.49 | 14.00 | 2.00 | 1.48 | 1.00 |
| | | *SS_4_VIII* | 26 | 2.43 | 95.36 | 16.00 | 2.50 | 1.59 | 0.97 |
| | n = 12 % | *SS_1_VIII* | 14 | 0.94 | 68.77 | 10.00 | 1.00 | 1.37 | 0.94 |
| | | *SS_2_VIII* | 14 | 1.34 | 95.05 | 12.00 | 1.50 | 1.17 | 0.89 |
| | | *SS_3_VIII* | 18 | 1.79 | 100.55 | 14.00 | 2.00 | 1.27 | 0.90 |
| | | *SS_4_VIII* | 20 | 2.16 | 109.07 | 16.00 | 2.50 | 1.24 | 0.86 |
| | n = 16 % | *SS_1_VIII* | 8 | 0.80 | 104.73 | 10.00 | 1.00 | 0.76 | 0.80 |
| | | *SS_2_VIII* | 9 | 1.07 | 123.17 | 12.00 | 1.50 | 0.73 | 0.72 |
| | | *SS_3_VIII* | 12 | 1.42 | 118.24 | 14.00 | 2.00 | 0.86 | 0.71 |
| | | *SS_4_VIII* | 13 | 1.73 | 135.57 | 16.00 | 2.50 | 0.80 | 0.69 |

The macroproperties obtained for each material, namely, $\sigma_c$ and $E$, were normalized with their respective microproperties, that is, $\sigma_c$ was normalized to the normal bond strength and $E$ was normalized to the particle's Young's modulus. These values are given in the tables above as as **Normalized Strength** and **Normalized Stiffness**. The average of these normalized values was taken for each porosity case (n=8%, n=10%, n=12% and n=16%) and these averages were plotted and are shown in Figure 5.1. It can be seen from this figure that the material uniaxial strength and stiffness decrease independently of the porosity value for anisotropic stress states. Further investigation revealed that the uniaxial strength was independent among all cases of anisotropy; however, the Young's modulus was more sensitive to the second case of anisotropy than the first.

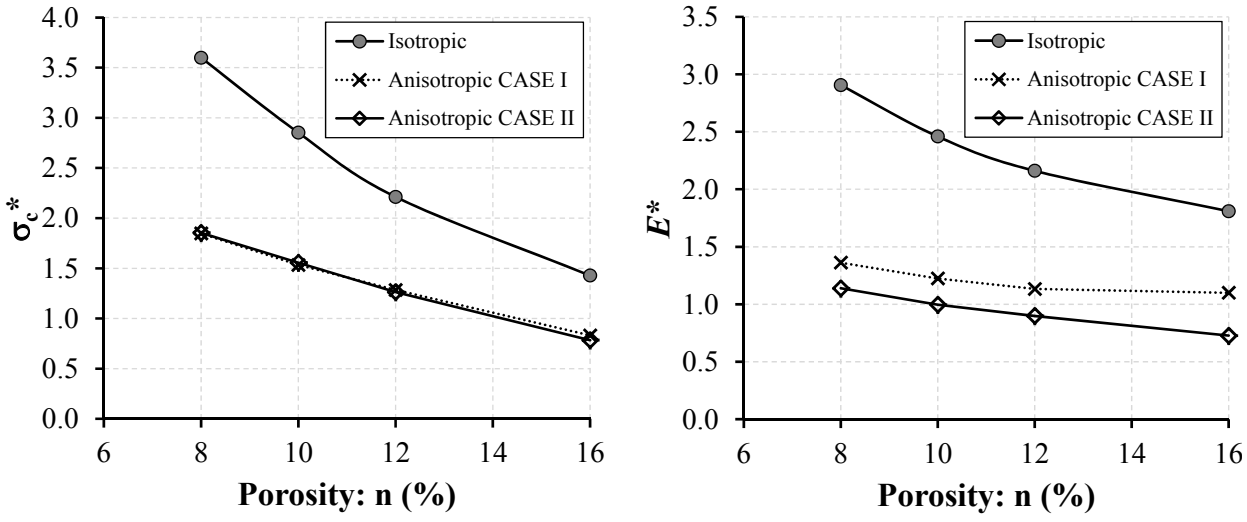


**Figure 5.1** Influence of state of stresses on selected macroproperties

A hypothesis was proposed to explain this mechanical behavior. A sample loaded isotropically develops nearly negligible stresses in the parallel bonds of the sample due to its isotropic nature as depicted on the left side of Figure 5.2. Thus, the *locked-in* stresses in the

majority of the parallel bonds will be near zero. On the other hand (refer to right side of Figure 5.2), when the sample undergoes an anisotropic state of stresses, the parallel bonds develop *locked-in* stresses that cannot be considered negligible.

This difference in magnitude between the *locked-in* stresses of the *Isotropic* bonds and the *Anisotropic* bonds indicates that the *Isotropic* bonds will require a larger deviatoric stress in order to achieve failure. Therefore, samples possessing parallel bonds under Isotropic stress states will appear to have larger uniaxial strength values. Conversely, the Anisotropic cases require smaller deviatoric stresses compared to the Isotropic cases; therefore, these samples will have a much lower uniaxial strength. It should be noted that while the *locked-in* stresses were allowed to settle, there was no discernible influence on the macromechanical properties.

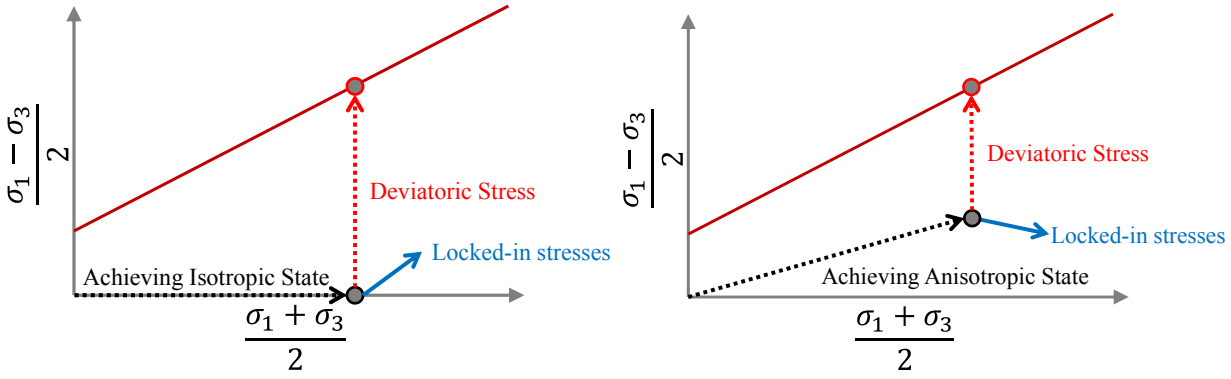


**Figure 5.2** RST result for samples with different porosities but matching macroproperties

## 5.2 CONFINEMENT PRESSURE BOUNDARY IMPACT

The boundary conditions on the side of the sample have shown to have a significant impact on the failure mode, as seen in Figure 5.3 below; however, the mechanical response still fails to achieve the desired results compared to the laboratory results that form the basis of the calibration process (Refer to Figure 5.3). The failure envelopes obtained in the numerical simulation show a linear tendency while the laboratory depicts a nonlinear form.

It is known that the use of this kind of boundary conditions make the biaxial results result in more realistic damage. For instance, the sample under $10MPa$ of confinement in Figure 5.4 shows a clear failure shear plane, and with the increment of confining pressure, the coalescence of shear failures start to emerge. Comparing the top and bottom results, i.e., confinement membrane boundary and rigid wall boundary, respectively, it is perceived that the wall boundary inhibits the development of failure characteristics named in section ***Mechanical behavior of rocks under high pressure confinements***.

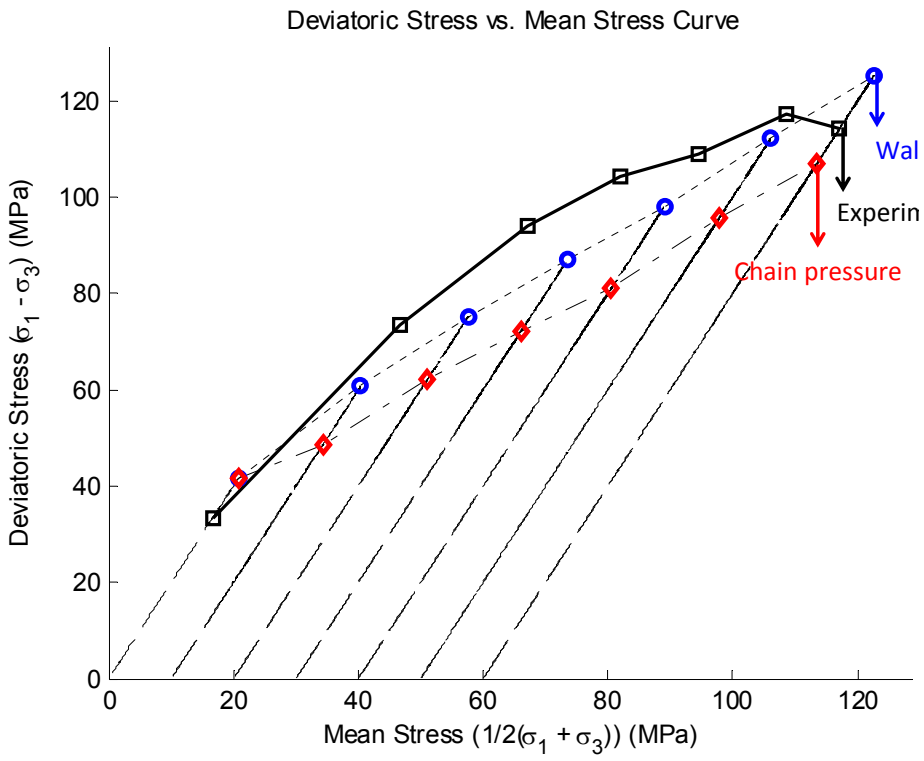


**Figure 5.3** Comparison of laboratory and numerical failure envelopes

## 5.3 STATISTICAL APPROACH FOR THE MICROPROPERTIES

The microproperties assigned to the DEM produce the macro-mechanical characteristics of the sample. Microproperties are assigned to the different entities of the DEM simulation, i.e., balls, walls, and to the contact models. In the PFC environment for preparing a sample, the macroproperties are assigned to the different entities and statistical randomness is assigned only to the contact model. The benefits of assigning a more realistic set of microproperties to both the contact model and the different microproperties of the particles were investigated. The Gaussian and Weibull distributions were chosen for fulfilling this statistical task.

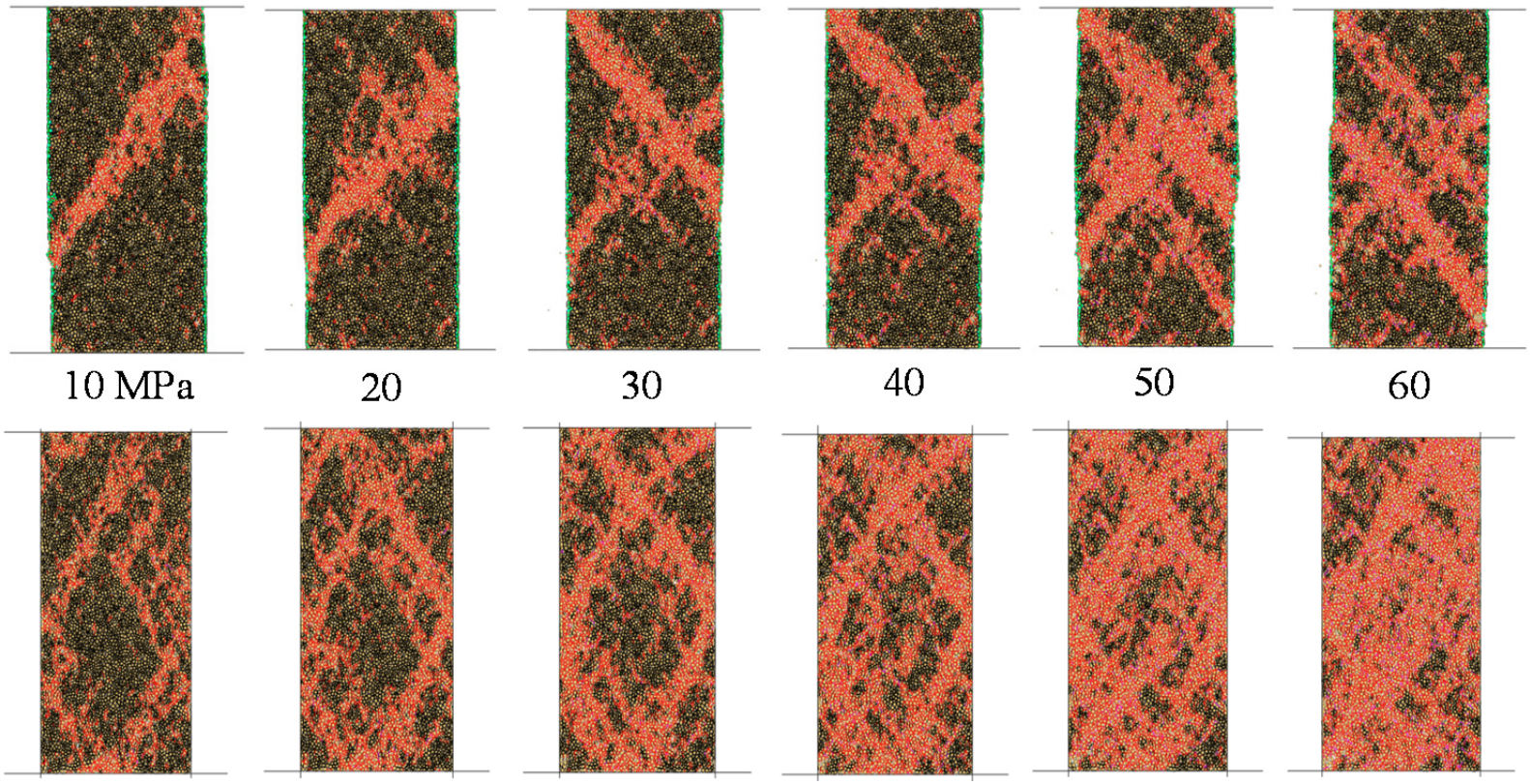


**Figure 5.4** Failure under different confinements of biaxial tests using chain pressure boundary on the top and rigid walls on the bottom

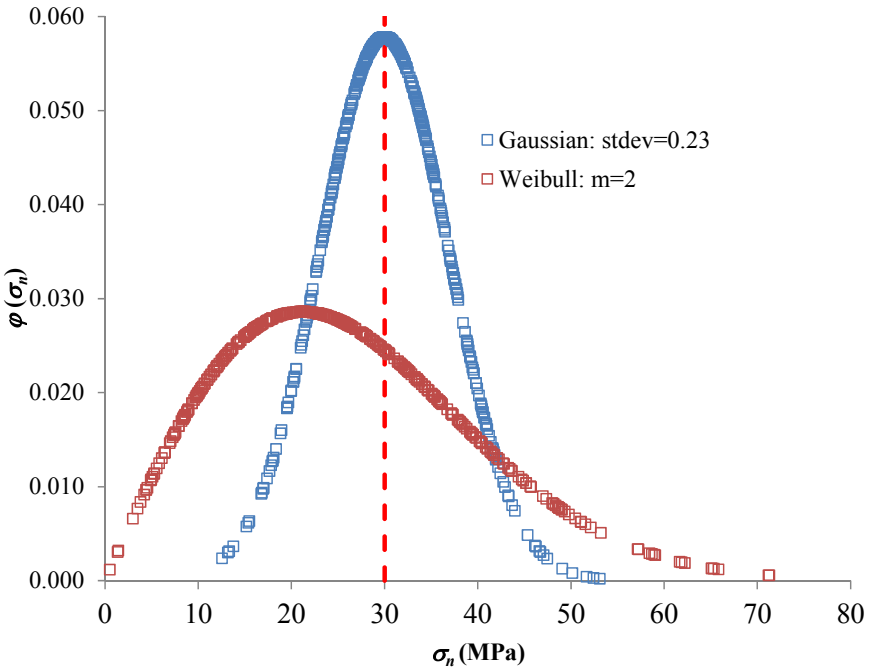


**(a)**

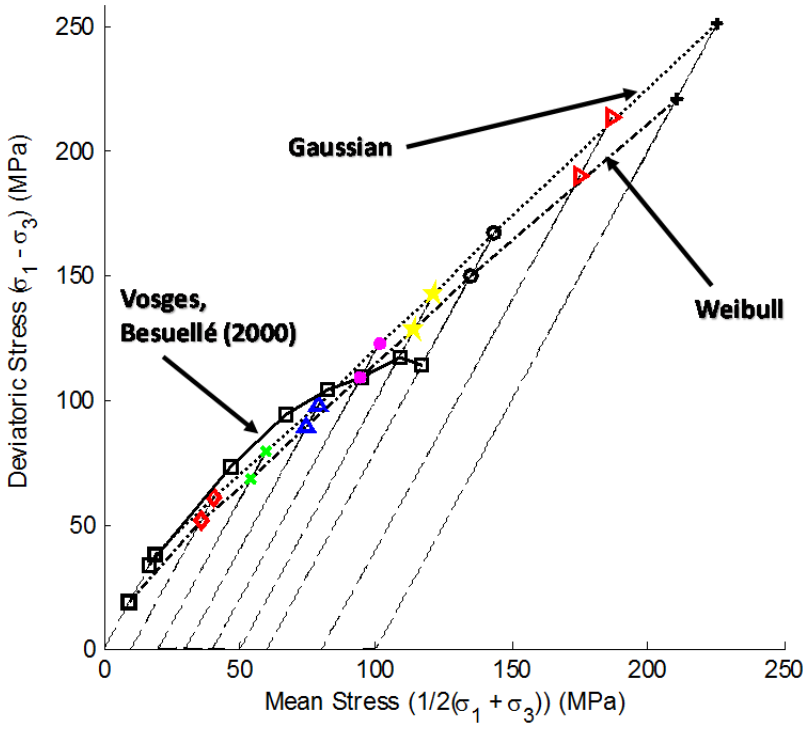


**(b)**

**Figure 5.5** (a) Gaussian and Weibull distribution assigned to tensile strength of the parallel bond and (b) mechanical response obtained.

Samples were created with microproperties following randomness from Gaussian and Weibull distributions. The distributions given to the normal tensile strength of the parallel bond are shown in Figure 5.5 (a). Also the failure envelopes obtained with pressures up to 240*MPa* are compared and do not suggest an advantage from choosing either statistical representation.

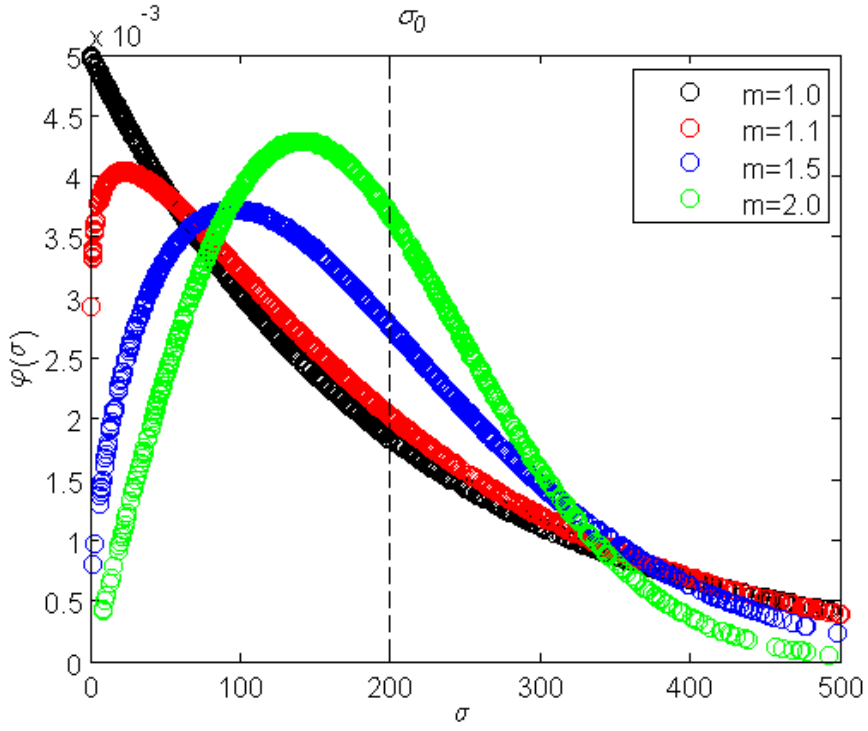


**Figure 5.6** Weibull distributions with different shape parameters "m"

Due to its shape parameter, the Weibull distribution has the inherent capability of creating different distribution shapes and can span from exponential to Gaussian. Analyses using the Weibull distribution with different shape parameters, m, were carried out and the curves of the different distributions used are shown in Figure 5.6. The results from this numerical analysis indicated the possibility of reproducing the failure envelope of specific rocks. Figure 5.7 shows the failure envelope obtained using the shape parameter m=1 and presents the same form as

laboratory results of Vosges sandstone. Moreover, a spectrum of failure envelopes arise from the use of the different Weibull distributions giving a quality of flexibility that does not exist in current models.

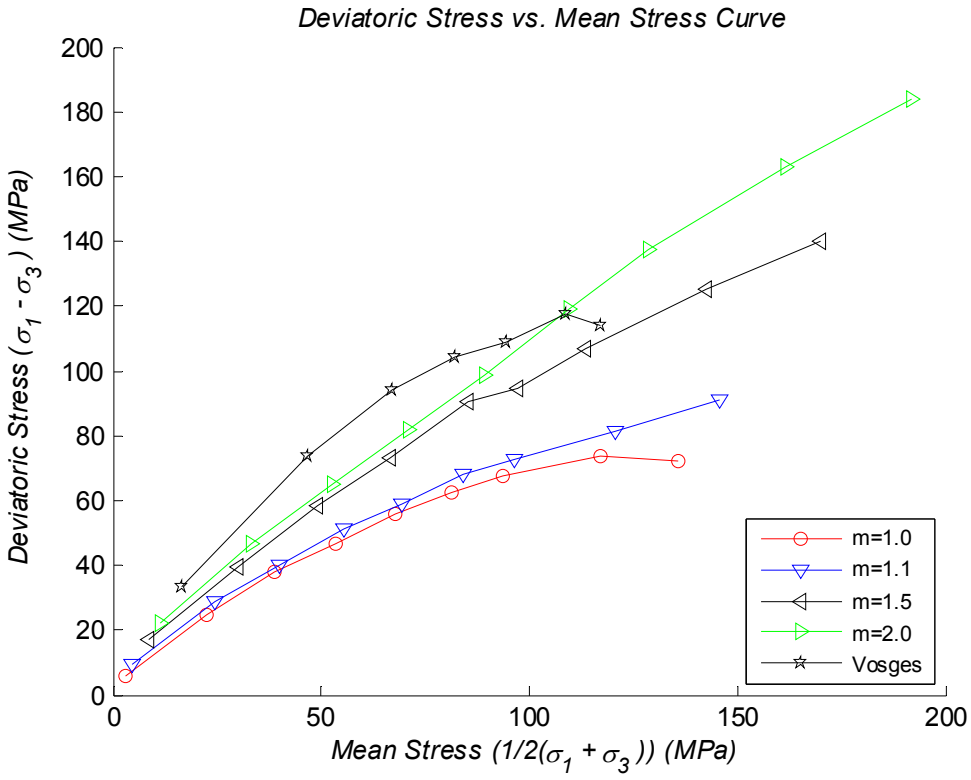


**Figure 5.7** Failure envelopes obtained using Weibull distributions with different shape parameters

## 5.4 ROCK CUTTING PROCESS UNDER PRESSURE

During the development of the DEM system under high pressure confinement, it became clear that using the confinement membrane boundary instead of the chain functions available in the PFC environment was advantageous. In Figure 5.8, three snapshots of the rock cutting process under high pressure are shown.

The snapshots (a) and (b) show some instability of the chain functions. In snapshot (a), the chain created a crack towards the bottom of the sample and missed particles that were both crushed and flying freely despite the fact they should be pressed toward the sample. In snapshot (b), odd patterns on the top of the sample are left behind the cutter, changing the topology of the cut surface. Encouragingly, these problems were not seen in snapshot (c), where the proposed confinement boundary pressure developed was used. The simulation results shown in snapshots (a) and (b) were performed with 140*MPa* of top pressure while the simulation in snapshot (c) had a top pressure of 240*MPa*. Additionally, the simulation performed using this developed confinement pressure boundary, the flow of particles below the cutter was observed. This phenomena was also investigated by Kaitkay and Lei [20] in experimental tests. These results, although referred to as simply failure by Kaitkay and Lei, prove the ability of the DEM to model rock cutting under high pressures with the implementation of the confinement boundary pressure while aligning with experimental results.

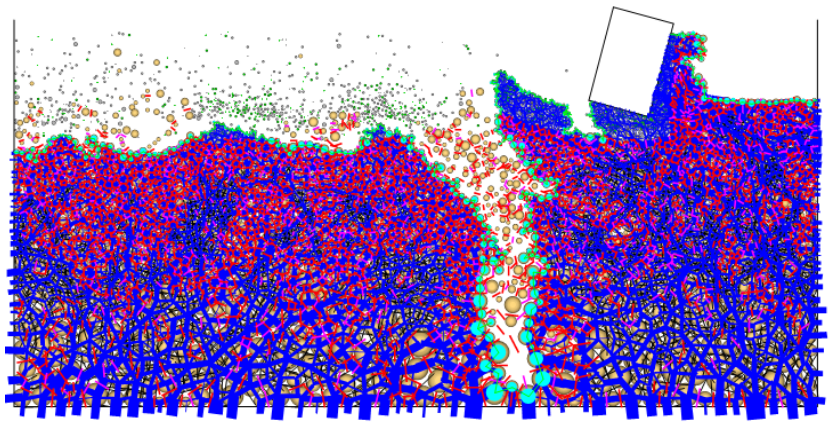

**(a)**

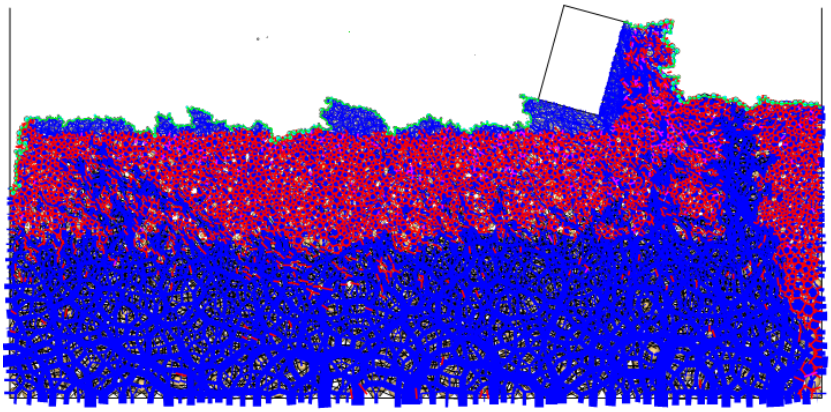

**(b)**

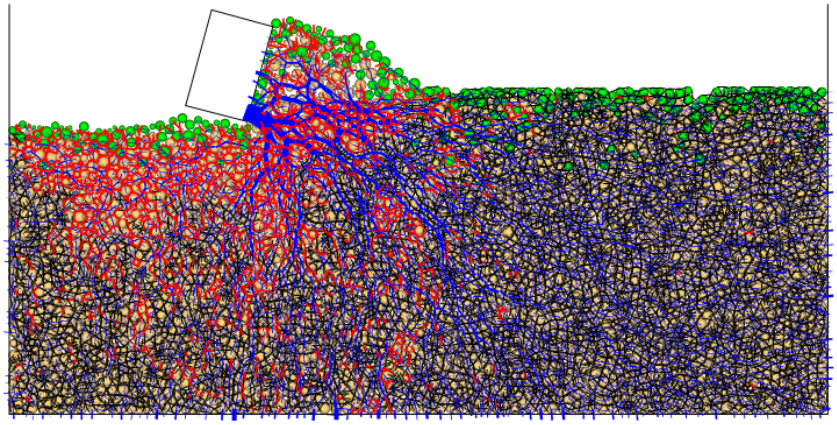

**(c)**

**Figure 5.8** Rock Cutting Under Pressure: (a) and (b) using chain functions under 140*MPa* of top pressure; and (c) using the Confinement Boundary Pressure under 240*MPa* of top pressure

# 6.0 CONCLUSIONS AND CONTRIBUTIONS

Finally, this study does not attempt to create a unique approach to the problems encountered but rather represents efforts to solve an initial set of problems. Some sections have been simplified and assumptions have been made in order to proceed with this modeling.

This study demonstrated that discrete element modeling was capable of providing reasonable estimates of cutting forces in the modeling of shallow rock scratch tests for rocks over a wide range of strength and stiffness values. It was also found that the force history of a three-dimensional model, which closely resembles that from an actual test, can be viewed as a collection of the cutting forces of the two-dimensional results averaged. Moreover, if the length of cut was much longer than that of the depth of cut, a two-dimensional result can be viewed as ergodic and thus justified its use.

In the rock cutting model, a DEM rock model only needed to be calibrated for its strength and stiffness and thus implicitly incorporated the porosity effect. This brought up an important question about the validity of the current practice of implicit modeling of rock porosity. This study found that the implicit modeling worked because the initial fabrics of sample of various porosities, as revealed by the contact force Rose Diagrams, were not greatly affected by the porosity and thus the samples were not mechanically significantly different. It was also found in this study that in a general two-dimensional DEM model, a model with approximately 16% porosity and a material that contains about 25% of its bonded contacts cracked would yield an

unconfined compressive strength to tensile strength ratio compatible to real rocks. Moreover, this study showed that there was a good link between two-dimensional and three-dimensional DEM rock models. For instance the 16% and 8% porosities of two-dimensional rock samples corresponded to 37% and 23% three-dimensional samples, respectively. This has an important bearing in general DEM rock modeling.

It is clear that the implications of this implicit porosity modeling on increasing computational efficiency are tremendous. A low porosity rock sample, traditionally considered computationally heavy due to its relatively high number of particles, can now be easily manipulated with microdefects in order to quickly and efficiently model its macroproperties.

To follow up on the present work, future research in the two following areas would be worth pursuing as they would have significant immediate impacts: First, investigate introducing the pressure-dependency of rocks through DEM. Second, investigate scaling the DEM model from the current study that involved mm size particles to include the larger scale found in practical engineering problems.

This study has completed some preliminary studies on pressure effects. The adoption of Hertz contact springs did not make much difference. The introduction of Weibull distribution for stiffness and for strength did accurately represent rock behavior, but the brittle to ductile transition for rocks under *kPa* pressure to *MPa* pressure failed to exist. The questions of interests for future study include: Would the introduction of new particle level micro parameters, or a modification of the existing parameters, to physically sound pressure-dependent parameters, be sufficient to appropriately model the observed rock behavior? Or would some new type of contact that would effectively fuse particles together under high pressure be needed?

Regarding the problem of scale, could one simply select the near field DEM particle size to a certain proportion of the problem dimension? In this respect, would it possible to make the fracture energy independent of the DEM particle size and thus ascertain the results are objective, in other words, could the results be made to be independent of DEM particle size?

Finally, this study does not attempt to create a unique approach to the problems encountered but rather represents efforts to solve an initial set of problems. Some sections have been simplified and assumptions have been made in order to proceed with this modeling.

## BIBLIOGRAPHY


[1] Richard T. Determination of Rock Strength from Cutting Tests: University of Minnesota, 1999.

[2] Dagrain F, Poyol E and Richard T. Strength Logging of Geomaterials from Scratch Tests. In: EUROROCK 2004 & 53rd Geomechanics Colloquium, Salzburg, Austria, 2004.

[3] Potyondy DO and Cundall P. A bonded-particle model for rock. International Journal of Rock Mechanics and Mining Sciences, 2004; 49: 1329-64.

[4] Kahraman S, Fener M and Kozman E. Predicting the compressive and tensile strength of rocks from indentation hardness index. The Journal of The Southern African Institute of Mining and Metallurgy, 2012; 112: 9.

[5] Cundall PA. A computer model for simulating progressive large scale movements in blocky rock systems. In: Proceedings of the Symposium of the International Society of Rock Mechanics, Nancy, France, 1971.

[6] Cundall PA and Strack ODL. A discrete numerical model for granular assemblies. Géotechnique, 1979; 29: 47-65.

[7] Itasca Consulting Group Inc. PFC2D/3D (Particle Flow Code in 2/3 Dimensions), Version 4.0. Minneapolis, MN: ICG; 2008.

[8] Potyondy DO. A Flat-Jointed Bonded-Particle Material for Hard Rock. In: The 46th US Rock Mechanics / Geomechanics Symposium - ARMA, Chicago, IL, 2012. 10.

[9] Itasca. Itasca Consulting Group Inc. PFC2D/3D (Particle Flow Code in 2/3 Dimensions), Version 4.0. Minneapolis, MN: ICG; 2008, 2008.

[10] Cho N, Martin CD and Sego DC. A clumped particle model for rock. International Journal of Rock Mechanics and Mining Sciences, 2007; 44: 14.

[11] Diedrichs MS, Instability of hard rock masses: the role of tensile damage and relaxation, in Civil Engineering. 2000, University of Waterloo.

[12] Utili S and Nova R. DEM analysis of bonded granular geomaterials. International Journal for Numerical and Analytical Methods in Geomechanics, 2008; 32: 35.

[13] Wang Y and Tonon F. Modeling Lac du Bonnet granite using a discrete element model. International Journal of Rock Mechanics and Mining Sciences, 2009; 46: 12.

[14] Wang Y and Tonon F. Calibration of a discrete element model for intact rock up to its peak strength. International Journal for Numerical and Analytical Methods in Geomechanics, 200923.

[15] Ledgerwood III LW. PFC modeling of rock cutting under high pressure conditions. In: Rock Mechanics: Meeting Society's Challenges and Demands (1st Canada-U.S. Rock Mechanics Symposium, Vancouver, May 2007), Vancouver: Taylor & Francis Group., 2007. 511-18.

[16] Detournay E and Defourny P. A Phenomenological Model for the Drilling Action of Drag Bits. International Journal of Rock Mechanics and Mining Sciences, 1992; 29: 13-23.

[17] Richard T, Determination of strength from cutting tests. 1999, University of Minnesota: Minneapolis, MN. p. 99.

[18] Richard T, Detournay E, Drescher A, Nicodeme O and Fourmaintraux D. The scratch test as a means to measure strength of sedimentary rocks. In: SPE/ISRM Rock Mechanics in Petroleum Eng. Conference, Trondheim, Norway, 1998. 15-22.

[19] Schei G, Fjaer E, Detournay E, Kenter CJ, Fuh GF and Zausa F. The scratch test: An Attractive technique for determining strength and elastic properties of sedimentary rocks. In: SPE Annual Technical Conference and Exhibition, Dallas, Texas, 2000.

[20] Kaitkay P and Lei S. Experimental study of rock cutting under external hydrostatic pressure. Journal of Materials Processing Technology, 2005; 159: 206-13.

[21] Huang H, Detournay E and Bellier B. Discrete element modelling of rock cutting. In: The 37th U.S. Rock Mechanics Symposium. Rock Mechanics for Industry, Vail, USA, 1999. 123-30.

[22] Huang H, Discrete Element Modeling of Tool-Rock Interaction, in Civil Engineering. 1999, University of Minnesota: Minnesota.

[23] Rojek J. Discrete element modeling of rock cutting. Computer Methods in Materials Science, 2007; 7: 224-30.

[24] Nishimatsu Y. The mechanics of rock cutting. International Journal of Rock Mechanics and Mining Sciences & Geomechanics Abstracts, 1972; 9: 261-70.

[25] Evans I. The force requiered for pointed attacks picks. International Journal of Mining Engineering, 1965; 2: 63-71.

[26] Huang H and Detournay E. Intrinsic Length Scales in Tool-Rock Interaction. International Journal of Geomechanics, 2008; 8: 39-44.

[27] Rojek J, Oñate E, Labra C and Kargl H. Discrete element simulation of rock cutting. International Journal of Rock Mechanics and Mining Sciences, 2011; 48: 996-1010.

[28] Su O and Ali Akcin N. Numerical simulation of rock cutting using the discrete element method. International Journal of Rock Mechanics and Mining Sciences, 2011; 48: 434-42.

[29] Lei ST and Kaitkay P. Distinct Element Modeling of Rock Cutting under Hydrostatic Pressure. Key Engineering Materials, 2003; 250: 110-17.

[30] Lei ST, Kaitkay P and Shen X. Simulation of rock cutting using distinct element method - PFC$^{2D}$. In: Numerical Modeling in Micromechanics Via Particle Methods, Leiden: A.A. Balkema Publishers, 2004. 63-71.

[31] Block G and Jin H. Role of failure mode on rock cutting dynamics. In: SPE Annual Technical and Exhibition, New Orleans, Louisiana, 2009.

[32] Vernik L, Bruno M and Bovberg C. Empirical relations between compressive strength and porosity of siliciclastic rocks. In: International Journal of Rock Mechanics and Mining Sciences & Geomechanics Abstracts: Pergamon, 1993. 677-80.

[33] Lubachevsky BD and Stillinger FH. Geometric properties of random disk packings. Journal of Statistical Physics, 1990; 60: 561-83.

[34] Kansal AR, Torquato S and Stillinger FH. Computer generation of dense polydisperse sphere packings. The Journal of chemical physics, 2002; 117: 8212.

[35] Bagi K. An algorithm to generate random dense arrangements for discrete element simulations of granular assemblies. Granular Matter, 2005; 7: 31-43.

[36] Schöpfer MPJ, Abe S, Childs C and Walsh JJ. The impact of porosity and crack density on the elasticity, strength and friction of cohesive granular materials: Insights from DEM modelling. International Journal of Rock Mechanics and Mining Sciences, 2009; 46: 250-61.

[37] Deere DU and Miller RP, Engineering classification and index properties for intact rock. 1966, Air Force Weapons Lab: Kirtland Air Base, New Mexico.

[38] Bell FG. Engineering Properties of Soils and Rocks. London: Blackwell Science Ltd., 2000.

[39] Paterson MS and Wong T-f. Experimental Rock Deformation-the Brittle Field, 2005.

[40] Wong T-f, David C and Zhu W. The transition from brittle faulting to cataclastic flow in porous sandstones: Mechanical deformation. J Geophys Res, 1997; 102: 3009-25.

[41] Dagrain F and Richard T, On the influence of PDC wear and rock type on friction coeffictient and cutting efficiency, in EUROROCK 2006: Multiphysics coupling and

long term behaviour in rock mechanics, A Van Cotthen, et al., Editors. 2006, Taylor and Francis Group: Liège, Belgium.

[42] Tsuongui O, Vallet D and Charmet J-C. Numerical model of crushing of grains inside two-dimensional granular materials. Powder Technology, 1999; 105: 190-98.

[43] Nakata Y, Hyde AFL, Hyodo M and Murata H. A probabilistic approach to sand particle crushing in the triaxial test. Géotechnique, 1999; 49: 567-83.

[44] McDowell GR and Amon A. The application of Weibull statistics to the fracture of soil particles. Soils and Foundations, 2000; 40: 133-41.

[45] Nakata Y, Kato Y, Hyodo M, Hyde AFL and Murata H. One-dimensional compression behaviour of uniformly graded sand related to single particle crushing strength. Soils and Foundations, 2001; 41: 39-51.

[46] Wong R, H. C., Chau K, T. and Wang P. Microcracking and Grain Size Effect in Yuen Long Marbles. International Journal of Rock Mechanics and Mining Sciences & Geomechanics Abstracts, 1996; 33: 7.

[47] Mendoza JA, Gamwo IK, Zhang W and Lin J-S, Discrete Element Modeling of Rock Cutting Using Crushable Particles, 44th U.S. Rock Mechanics Symposium and 5th U.S.-Canada Symposium. 2010, ARMA 10-232. Salt Lake City, Utah, USA.

[48] Hale PA and Shakoor A. A laboratory investigation of the effects of cyclic heating and cooling, wetting and drying, and freezing and thawing on the compressive strength of selected sandstones. Environmental & Engineering Geoscience, 2003; 9: 117-30.

[49] Bésuelle P, Desrues J and Raynaud S. Experimental characterisation of the localisation phenomenon inside a Vosges sandstone in a triaxial cell. International Journal of Rock Mechanics and Mining Sciences, 2000; 37: 1223-37.

[50] Mendoza JA, Gamwo IK, Zhang W and Lin J-S, Considerations for Discrete Modeling of Rock Cutting, 45th US Rock Mechanics / Geomechanics Symposium. 2011, ARMA 11-209. San Fracisco, California, USA.